Title
Multiscale imaging and machine-learning approaches to investigate cardiovascular and metabolic diseases

Permalink
https://escholarship.org/uc/item/9761039m

Author
Chang, Chih-Chiang

Publication Date
2021

Peer reviewed|Thesis/dissertation

UNIVERSITY OF CALIFORNIA

Los Angeles

Multiscale imaging and machine-learning approaches to investigate cardiovascular and metabolic diseases

A dissertation submitted in partial satisfaction of the
requirements for the degree Doctor of Philosophy in Bioengineering

by

Chih-Chiang Chang

2021

ABSTRACT OF THE DISSERTATION

Multiscale imaging and machine-learning approaches to investigate cardiovascular and metabolic diseases

by

Chih-Chiang Chang

Doctor of Philosophy in Bioengineering

University of California, Los Angeles, 2021

Professor Tzung Hsiai, Chair

Abstract

Cardiovascular and correlated metabolomic diseases remain the leading cause of death in the United States and around the world. Three-dimensional (3-D) and real-time imaging techniques for investigating cardiovascular physiology and pathology mechanisms remain a significant challenge. In this thesis, I first introduce advanced light-sheet microscopy that enables multi-dimensional and multi-scale imaging via illuminating specimens with a thin sheet of the laser. This imaging strategy allows rapid data acquisition with a high spatiotemporal resolution, minimal photo-bleaching, and photo-toxicity. Its multiscale capability also empowers us to image and investigate the cardiovascular physiology and pathology at the scales from zebrafish embryos to adult mouse hearts and even human organs. Secondly, the custom-build light-sheet system was established and optimized to investigate the retinas in the embryonic mouse model.

By combining light-sheet with tissue-clearing and computational quantification, we revealed the 3-D retinal microvascular network including primary (inner) and secondary (outer) plexuses as well as the vertical sprouts bridging the two plexuses. Whereas, in an oxygen-induced retinopathy (OIR) mouse model, we demonstrated preferential obliteration of the secondary plexus and bridging vessels with a relatively unscathed primary plexus. Using clustering coefficients and Euler numbers, we computed the local versus global vascular connectivity. While local connectivity was preserved, the global vascular connectivity in OIR retinas was significantly reduced. Overall, the application of 3-D LSFM images coupled with computational quantification provides vascular insights into OIR, with translational significance for developing therapeutic interventions to prevent visual impairment. Thirdly, we developed electrical impedance tomography (EIT) as a non-invasive and portable detection method for fatty infiltrate in the liver. Since non-alcoholic fatty liver disease (NAFLD) is still endemic in developed countries and is one of the most common causes of cardiometabolic diseases, there is an unmet clinical need for non-invasive and cost-effective monitoring of fatty liver disease. The current gold diagnosis standard is liver biopsy which is prone to bleeding and has the risk of complications and sampling errors. Using acquired voltage data and the reconstruction algorithm for the EIT imaging, we computed the absolute conductivity distribution of the abdomen in 2-D. We performed correlation analyses to compare the individual EIT conductivity vs. MRI PDFF. Our results demonstrated that EIT conductivity (S·m^{-1}) is inversely correlated with the MRI proton-density fat fraction percentage (PDFF%) in the liver. This inverse correlation holds promises for developing non-invasive and portable liver EIT for early detection of fatty liver content in overweight individuals.

The dissertation of Chih-Chiang Chang is approved.

Linda L. Demer

Song Li

Atsushi Nakano

René Rupen Sevag Packard

Alison Chu

Tzung Hsiai, Committee Chair

University of California, Los Angeles

2021

DEDICATION

This dissertation is dedicated to my father, Chin-Chou Chang, my mother Hsiao-Man Yang, my sister Jung-Jung Chang.

ACKNOWLEDGEMENT

First, I would like to express my highest gratitude to my research adviser Dr. Tzung K. Hsiai. He always encourages his trainees to think creatively and challenge themselves which is very helpful to my Ph.D. career. Furthermore, he has been always supportive of my research and gave me numerous advice to be successful not only during Ph.D. training but also in my future career.

I would like to also show appreciation to those whom I collaborated with in my Ph.D. career. Alison Chu at UCLA pediatrics is always nice and encouraging. We have completed a great publication together. Dr. Yuchong Tai at the California Institute of Technology, a pioneer and leader in MEMS fabrication. His optimism and energy in communication and academic performance inspired me a lot. Dr. Linda Demer and Dr. Yin Tintut have been always supportive and offered helpful advice during my Ph.D.

In addition, I would like to give special thanks to those who serve on my committee for their efforts and energy: Drs. Linda L. Demer, Song Li, Atsushi (Austin) Nakano, René Rupen Sevag Packard, and Alison Chu. Their scientific advice during my oral qualification exam and defense was truly inspirational and helpful for my research focus and success. Their leadership, career achievement, and always positive are exemplars for my future career.

Additionally, I really appreciate all my colleagues who are always collaborative and supportive as my friends and mentors. Without their advice and assistant, it would not be possible to complete my PhD work. Dr. Rongsong Li is an expert in molecular biology always offers me helpful advice when I have questions or problems in biology. Dr. Rene Packard is a talented researcher and cardiologist who always give me great support and helpful suggestions. Dr. Nelson Jen is an energetic and great researcher who has provided many critical comments to my research and career. Dr. Jeffrey J. Hsu is an intelligent physician-scientist who can always identify the critical clinical questions combine with his research. His mentorship to medical students and junior STAR fellows has been instrumental in leadership. He has been always collaborative and supportive to me and other lab colleagues. I am grateful for his friendship and contribution to make our lab always energetic and full of fun. Dr. Yichen Ding is one of the most hardworking persons I've ever met. He introduced me to the exciting optical microscopy field which is the foundation of my Ph.D. research. He is always supportive and encouraging to the lab colleagues. Dr. Kyung-In Baek is another most hard-working person I met in the lab. His enthusiasm for research inspired me. He is also always supportive and collaborative. I have got a lot of scientific support and advice from both Yichen and Kyung and I feel very lucky to have them as my lab colleagues and friends. In addition, my colleagues Ana, Susana, Ryan, Sandro, Qingyu, and fellow Ph.D. candidates including Junjie, Zhaoqiang, Mehrdad, and Jing have been excellent researchers that I usually learn a lot from them. Their dedications in molecular biology, optical imaging, computational biology, and fluid dynamics were highly relevant to the lab. My former lab members, Drs. Nelson Jen, Tyler J. Beebe, Juhyun Lee have been good mentors and friends.

Finally, I wish to express my love and gratitude to my family. My father, Chin-Chou Chang, who is always optimistic and supportive, greatly affects my outlook on world value and life. He is one of the major sources bring me to where I am today. My mother, Hsiao-Man Yang, has been always supported my decisions. I could not achieve where I am now without her support and encouragement. My brilliant sister, Jung-Jung Chang, has always brought vitality and happiness to my family. My grandma, I-Tsai, always offers me unconditional support and never forgets me if she gets the good stuff. I feel that I am more than lucky to have them. Last but not least, I want to express my deepest gratitude again to my family that I could not achieve where I am today without their support and encouragement.

TABLE OF CONTENTS

CHAPTER IV. LIVER ELECTRICAL IMPEDANCE TOMOGRAPHY FOR EARLY IDENTIFICATION OF FATTY INFILTRATE IN OBESITY

LIST OF FIGURES

CHAPTER I

CHAPTER II

CHAPTER III

CHAPTER IV

LIST OF TABLES

CHAPTER II

CHAPTER III

CHAPTER IV

CURRICULUM VITAE

EDUCATION

University of Pennsylvania, Philadelphia, Pennsylvania
M.S.E in Bioengineering, School of Engineering and Applied Science

National Taiwan University, Taipe, Taiwan
M.S. in Biomedical Electronics and Bioinformatics

National Taiwan University, Taipe, Taiwan
B.S.E. in Electrical Engineering

PROFESSIONAL SOCIETIES

2019-Present	American Association of Anatomist (AAA)
2016-Present	American Heart Association (AHA)
2016-Present	Biomedical Engineering Society (BMES)
2019-Present	The Association for Research in Vision and Ophthalmology (ARVO)

RELATED PUBLICATIONS

1. **Chang CC**, Chu A, Meyer S, Ding Y, Sun MM, Abiri P, Baek KI, Gudapati V, Ding X, Guihard P, Bostrom KI. Three-dimensional Imaging Coupled with Topological Quantification Uncovers Retinal Vascular Plexuses Undergoing Obliteration. *Theranostics*. 2021;11(3):1162.
2. **Chang CC**, Huang ZY, Shih SF, Luo Y, Ko A, Cui Q, Sumner J, Cavallero S, Das S, Gao W, Sinsheimer J. Electrical impedance tomography for non-invasive identification of fatty liver infiltrate in overweight individuals. *Scientific Reports*. 2021 Oct 6;11(1):1-2.
3. Baek KI, Qian Y, **Chang CC**, O'Donnell R, Soleimanian E, Sioutas C, Li R, Hsiai TK. An Embryonic Zebrafish Model to Screen Disruption of Gut-Vascular Barrier upon Exposure to Ambient Ultrafine Particles. *Toxics*. 2020 Dec;8(4):107.
4. Li R, Adami A, **Chang CC**, Tseng CH, Hsiai TK, Rossiter HB. Serum Acylglycerols Inversely Associate with Muscle Oxidative Capacity in Severe COPD. *Medicine and Science in Sports and Exercise*. 2021 Jan;53(1):10.
5. Baek KI, Chang SS, **Chang CC**, Roustei M, Ding Y, Wang Y, Chen J, O'donnelle R, Chen H, Ashby JW, Mack JJ. Vascular Injury Changes Topology of Vessel Network to Adapt to Partition of Blood Flow for New Arteriovenous Specification. *BioRxiv*. 2020 Jan 1.
6. Abiri P, Abiri A, Gudapati V, **Chang CC**, Roustaei M, Bourenane H, Anwar U, Markovic D, Hsiai TK. Wireless pacing using an asynchronous three-tiered inductive power transfer system. *Annals of Biomedical Engineering*. 2020 Apr;48(4):1368-81.
7. Hsu JJ, Fong F, Patel R, Qiao R, Lo K, Soundia A, **Chang CC**, Le V, Tseng CH, Demer LL, Tintut Y. Changes in microarchitecture of atherosclerotic calcification assessed by 18 F-NaF PET and CT after a progressive exercise regimen in hyperlipidemic mice. *Journal of Nuclear Cardiology*. 2020 Jan 2:1-8.
8. Ding Y, Gudapati V, Lin R, Fei Y, Packard RR, Song S, **Chang CC**, Baek KI, Wang Z, Roustaei M, Kuang D. Saak transform-based machine learning for light-sheet imaging of cardiac trabeculation. *IEEE Transactions on Biomedical Engineering*. 2020 May 1;68(1):225-35.
9. Zhao H, **Chang CC**, Liu Y, Yang Y, Tseng WJ, de Bakker CM, Chung R, Ghosh P, Deng L, Liu XS. Reproducibility and Radiation Effect of High-Resolution In Vivo Micro Computed Tomography Imaging of the Mouse Lumbar Vertebra and Long Bone. *Annals of Biomedical Engineering*. 2020 Jan;48(1):157-68.

10. Chen J, Ding Y, Chen M, Gau J, Jen N, Nahal C, Tu S, Chen C, Zhou S, **Chang CC**, Lyu J. Displacement analysis of myocardial mechanical deformation (DIAMOND) reveals segmental susceptibility to doxorubicin-induced injury and regeneration. *JCI Insight*. 2019 Apr 18;4(8).
11. Hsu JJ, Vedula V, Baek KI, Chen C, Chen J, Chou MI, Lam J, Subhedar S, Wang J, Ding Y, **Chang CC**. Contractile and hemodynamic forces coordinate Notch1b-mediated outflow tract valve formation. JCI insight. 2019 May 16;4(10).
12. Lee J, Vedula V, Baek KI, Chen J, Hsu JJ, Ding Y, **Chang CC**, Kang H, Small A, Fei P, Chuong CM. Spatial and temporal variations in hemodynamic forces initiate cardiac trabeculation. *JCI Insight*. 2018 Jul 12;3(13).
13. Hsu JJ, Lu J, Umar S, Lee JT, Kulkarni RP, Ding Y, **Chang CC**, Hsiai TK, Hokugo A, Gkouveris I, Tetradis S. Effects of teriparatide on morphology of aortic calcification in aged hyperlipidemic mice. *American Journal of Physiology-Heart and Circulatory Physiology*. 2018 Jun 1.
14. Luo Y, Abiri P, Zhang S, **Chang CC**, Kaboodrangi AH, Li R, Sahib AK, Bui A, Kumar R, Woo M, Li Z. Non-invasive electrical impedance tomography for multi-scale detection of liver fat content. *Theranostics*. 2018;8(6):1636.
15. Ding Y, Abiri A, Abiri P, Li S, **Chang CC**, Baek KI, Hsu JJ, Sideris E, Li Y, Lee J, Segura T. Integrating light-sheet imaging with virtual reality to recapitulate developmental cardiac mechanics. *JCI Insight*. 2017 Nov 16;2(22).

Review Articles

16. Baek KI*, Ding Y*, **Chang CC***, Chang M, Packard RR, Hsu JJ, Fei P, Hsiai TK. Advanced microscopy to elucidate cardiovascular injury and regeneration: 4D light-sheet imaging. *Progress in Biophysics and Molecular Biology*. 2018 Oct 1;138:105-15. **(* equally contributed to this work)**
17. Li R, Baek KI, **Chang CC**, Zhou B, Hsiai TK. Mechanosensitive pathways involved in cardiovascular development and homeostasis in zebrafish. *Journal of Vascular Research*. 2019;56(6):273-83.
18. Ding Y, Ma J, Langenbacher AD, Baek KI, Lee J, **Chang CC**, Hsu JJ, Kulkarni RP, Belperio J, Shi W, Ranjbarvaziri S. Multiscale light-sheet for rapid imaging of cardiopulmonary system. *JCI Insight*. 2018 Aug 23;3(16).
19. Ding Y, Lee J, Hsu JJ, **Chang CC**, Baek KI, Ranjbarvaziri S, Ardehali R, Packard RR, Hsiai TK. Light-sheet imaging to elucidate cardiovascular injury and repair. *Current Cardiology Reports*. 2018 May;20(5):1-8.

Book Chapters

1. Li R, Baek KI, **Chang CC**, Zhou B, Hsiai T. Mechanotransduction in Cardiovascular Development and Regeneration: A Genetic Zebrafish Model. InModern Mechanobiology 2021 Feb 25 (pp. 155-182). *Jenny Stanford Publishing*.
2. Luo Y, Abiri P, **Chang CC**, Tai YC, Hsiai TK. Epidermal EIT Electrode Arrays for Cardiopulmonary Application and Fatty Liver Infiltration. InInterfacing Bioelectronics and Biomedical Sensing 2020 (pp. 163-184). *Springer, Cham*.

Selected Abstracts

1. **Chang** CC, Ding Y, Abiri P, Sun MM, Meyer ST, Baek KI, Zheng JJ, Gordon LK, Chu A, Hsiai TK. Light-Sheet Imaging of Intact Retinal Vasculature and Quantitative Analysis in Murine Model. *Investigative Ophthalmology & Visual Science*. 2020 Jun 10;61(7):200-. (**ARVO 2020 Travel Award**)
2. **Chang CC**, Abiri P, Sun M, Baek KI, Chu A, Zheng J, Bostrom KI, Gordon L, Ding Y, Hsiai TK. Light-sheet Imaging of Intact Ocular System and Quantitative Analysis of Retinal Vasculature. *Circulation*. 2019 Nov 19;140(Suppl_1):A12355-. (**Rapid Fire Oral**)
3. **Chang CC,** Zhao H, Yang Y, de Bakker CM, Tseng WJ, Liu XS. Reproducibility of mouse trabecular bone microstructure at multiple skeletal sites by in vivo micro computed tomography imaging. *Summer Biomechanics, Bioengineering and Biotransport Conference*, National Harbor, MD, June 29-July 2, 2016.

Chapter I

Introduction

Light-Sheet imaging and application in cardiovascular research

The advent of three-dimensional imaging of biological organisms and tissues provides a fundamental basis for cardiovascular research. To unravel the cardiovascular morphogenesis, differentiation, proliferation, and regeneration, require high spatiotemporal resolution with deep tissue penetration to visualize the dynamic events. Conventional optical microscopes are limited by low tissue penetration and small working distance, prohibiting the capability of long-term live imaging that requires rapid data acquisition to minimize photobleaching and phototoxicity to the specimens [1-3]. Unlike confocal and wide-field microscopy (**Fig 1**), LSFM has the capacity to localize 4-D (3-D spatial + 1-D time or spectra) cellular phenomena with multiple fluorescence channels [3-6]. The unique operation of LSFM resides in the orthogonal optical pathway. It applies two separate sets of lenses for illumination and detection through its selective plane excitation (usually through the cylindrical lens) and offers several distinct advantages including: 1) rapid data acquisition, 2) deep axial resolution, 3) large dynamic range, 4) reduced photobleaching, and 5) large 3D structure reconstruction. In our light-sheet microscopy setup, we applied objective lenses with a low numerical aperture integrated with cylindrical lenses to generate a sheet of light for scanning across the sample. While a stack of images is acquired by moving the sample in a stepwise fashion along the detection axis, the axial resolution of the sample is dominated by the thickness of the light-sheet but not limited by the objective of the detection lens as conventional microscope like confocal or wide-field microscope. Thus, our light-sheet fluorescent microscopy system introduces deep-tissue penetration, high-spatiotemporal resolution, and minimal photobleaching. Our group has demonstrated the capacity of light-sheet imaging to uncover both mechanical and structural phenotypes in the cardiovascular systems in both zebrafish and mice [3, 5-8]. In this thesis, we developed and optimized the light-sheet microscope for imaging embryonic mouse retinas. We demonstrated the unscathed 3-D retinal microvascular network undergoing hyperoxia-induced obliteration from the secondary (outer) plexus to the vertical sprouts provided new network insights into OIR-associated vascular obliteration, with translational significance for investigating therapeutic interventions to prevent visual impairment.

Electrical Impedance Tomography for Liver Fat Content Quantification

Biological tissues store charge and have a frequency-dependent electrical impedance (Z) in response to applied alternating current (AC). At low frequencies, the lipid-bilayers impede the current flow, resulting in high conductivity, whereas, at high frequency, the bilayers serve as imperfect capacitors, resulting in tissue- and fluid-dependent impedance. This impedimetric property provides the basis for applying the Electrical Impedance Tomography (EIT) to measure tissue-specific conductivity, morphology, and volume [9-11]. Electrical impedance tomography (EIT) is a non-invasive medical imaging technique to reconstruct the conductivity image based on the tissue electrical properties derived from surface electrode measurements. Over the past few decades, EIT has seen ever-increasing medical imaging applications including cardiopulmonary, breast tissue, brain function as well as pulmonary disease and respiratory monitoring in clinical settings [11-13]. Although EIT is commonly used in medical applications, there is a paucity of work applying the EIT to target the screening of Nonalcoholic fatty liver disease (NAFLD). Our group previously has shown the feasibility of EIT to quantify the fat contents in animal models including pigs and rabbits [14]. In this thesis, we recruited overweight subjects (BMI>25) to undergo liver 3T MRI scans, followed by the portable EIT belts measurement.

MRIs were acquired to provide the a priori knowledge of the liver boundary condition to solve the inverse problem for EIT reconstruction. We further compared and validated the subject-specific EIT conductivity with the liver MRI proton-density fat fraction (PDFF) as a reference standard for fatty liver infiltrate. We reveal that the correlation between liver EIT conductivity or MRI PDFF with demographics is statistically insignificant, whereas liver EIT conductivity is inversely correlated with MRI PDFF. In short, EIT conductivity provides a portable method for operator-independent and cost-effective detection of hepatic steatosis.

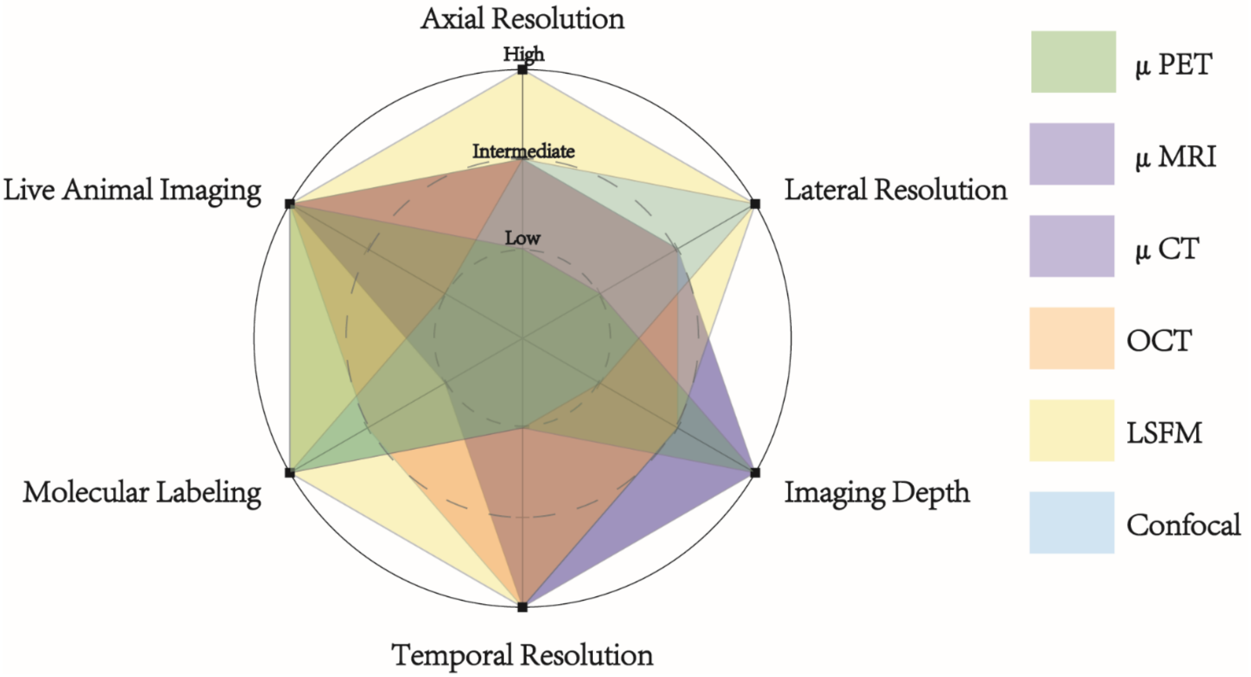

Figure 1. Comparison between different imaging modalities**.**

Reference

1. Ntziachristos V, Ripoll J, Wang LV, Weissleder R. Looking and listening to light: the evolution of whole-body photonic imaging. Nature biotechnology. 2005; 23: 313-20.
2. Scherf N, Huisken J. The smart and gentle microscope. Nature biotechnology. 2015; 33: 815-8.
3. Baek KI, Ding Y, Chang C-C, Chang M, Packard RRS, Hsu JJ, et al. Advanced microscopy to elucidate cardiovascular injury and regeneration: 4D light-sheet imaging. Progress in biophysics and molecular biology. 2018; 138: 105-15.
4. Chhetri RK, Amat F, Wan Y, Höckendorf B, Lemon WC, Keller PJ. Whole-animal functional and developmental imaging with isotropic spatial resolution. Nature methods. 2015; 12: 1171-8.
5. Dodt H-U, Saghafi S, Becker K, Jährling N, Niendorf A, Hahn C, et al. Ultramicroscopy: development and outlook. Neurophotonics. 2015; 2: 041407.
6. Fei P, Lee J, Packard RRS, Sereti K-I, Xu H, Ma J, et al. Cardiac light-sheet fluorescent microscopy for multi-scale and rapid imaging of architecture and function. Scientific reports. 2016; 6: 1-12.
7. Huisken J, Stainier DY. Even fluorescence excitation by multidirectional selective plane illumination microscopy (mSPIM). Optics letters. 2007; 32: 2608-10.
8. Huisken J, Stainier DY. Selective plane illumination microscopy techniques in developmental biology. 2009.
9. Brown BH. Electrical impedance tomography (EIT): a review. Journal of medical engineering & technology. 2003; 27: 97-108.
10. Holder DS. Electrical impedance tomography: methods, history and applications: CRC Press; 2004.
11. Bayford RH. Bioimpedance tomography (electrical impedance tomography). Annu Rev Biomed Eng. 2006; 8: 63-91.
12. Zhao Z, Müller-Lisse U, Frerichs I, Fischer R, Möller K. Regional airway obstruction in cystic fibrosis determined by electrical impedance tomography in comparison with high resolution CT. Physiological measurement. 2013; 34: N107.
13. Zhao Z, Zhang J-S, Chen Y-T, Chang H-T, Hsu Y-L, Frerichs I, et al. The use of electrical impedance tomography for individualized ventilation strategy in COVID-19: a case report. BMC pulmonary medicine. 2021; 21: 1-5.
14. Luo Y, Abiri P, Zhang S, Chang C-C, Kaboodrangi AH, Li R, et al. Non-invasive electrical impedance tomography for multi-scale detection of liver fat content. Theranostics. 2018; 8: 1636.

CHAPTER II

Advanced microscopy to elucidate cardiovascular injury and regeneration: 4D light-sheet imaging

Baek, K.I*., Ding, Y*., Chang, C.C*., Chang, M., Packard, R.R.S., Hsu, J.J., Fei, P. and Hsiai, T.K

* Equal contribution.

This chapter is reproduced from the review article published in ***Progress in Biophysics and Molecular Biology***, 2018, 138; 105-115 and approved by the co-authors.

Introduction

Zebrafish (*Danio rerio*) share conserved cardiovascular developmental signaling pathways with mammals, providing a genetically tractable model in developmental research, drug screening, and heart failure studies [1-5]. Zebrafish embryos are optically transparent, allowing for real-time visualization of structural and functional phenotypes [2, 6]. Their small size and short developmental stages facilitate high-throughput genetic, epigenetic, and pharmaceutical analyses [7, 8]. Although mammalian models including mice exhibit the capacity of tissue regeneration during the early stage of development, zebrafish demonstrate structural recovery in response to anatomical amputation, chemotherapy, or redox active ultrafine particles (UFP, diameter < 0.2 μm) in air pollutants [2]. In this review, we introduce our novel imaging technique using our custom-built light-sheet fluorescence microscopy (LSFM) to elucidate zebrafish models of cardiovascular injury and regeneration. We highlight the pathological effects of ambient UFP exposure underlying impaired Notch transcriptional activation complex to promote vascular regeneration [9]. Furthermore, we introduce a novel flow-responsive mechano-metabolic pathway implicated in vascular regeneration [10].

1. Light-sheet imaging to study cardiovascular regeneration

Live imaging has transformed biomedical sciences by permitting visualization and analysis of dynamic cellular processes as they occur in their native contexts [11-13]. Conventional methods continue to be useful, but the pursuit of new biological insights often requires higher spatiotemporal resolution in ever-larger, intact samples and, crucially, a gentle touch, such that biological processes continue unhindered. Although confocal microscopy improves spatial resolution and image contrast, using the same path for both illumination and fluorescence detection leads to intensive photo-bleaching and photo-toxicity with limited penetration depth (100-150 μm) [14, 15]. Multi-photon microscopy utilizes an infrared mode-locked laser as the illumination source and reaches up to 1 mm penetration depth [16, 17], but requires a high numerical aperture (NA > 0.7) and a short laser pulse with a long wavelength. On account of these limitations, LSFM splits the paths so that the illumination plane is perpendicular to the detection angle. Therefore, fluorescence is emitted from the selective focal plane, and only a few fluorescent molecules are excited in the micrometer thickness of the light-sheet.

In comparison to conventional microscopy, LSFM integrates several distinct advantages [18, 19]. (1) LSFM exposes the specimens to at least three orders of magnitude less light energy than confocal and multi-photon fluorescence microscopes over conventional excitation, thus greatly reducing photo-bleaching and photo-toxicity by two to five orders of magnitude [20-22]. In the absence of a pinhole, the loss of energy efficiency of the illumination beam is not more than 5% after transmission through the lenses and mirrors to scan a plane of sample. (2) LSFM allows for illuminating the desired sample area, significantly increasing signal efficiency and axial resolution. The thickness of the light-sheet generated by the illumination lens is the major determinant of the axial resolution whereas the axial resolution of other optical microscopes is predominately determined by the NA of the detection lens. (3) LSFM enables rapid imaging at 100 frames/sec (~400 megapixels/sec) after applying a sCMOS or CCD camera with a large dynamic range, far more than the 10 megapixels/sec of confocal or multi-photon microscopy. (4) LSFM also provides higher signal-to-noise ratio which is over 100:1, while that of confocal microscopy is 60:1 and multi-photon microscopy is only 10:1. LSFM for the present experimental data set was carried out on previously developed systems (**Fig. 1A**) [3, 23-28].

The detection path, including an objective lens (10x/0.25, Nikon), a tube lens (ITL 200, Thorlabs), and switchable optical filters (Semrock, NewYork, USA), was placed orthogonal to the illumination plane for collecting fluorescence signals (**Fig. 1B$_{1\text{-}2}$**). Digital images were recorded with a high frame rate by using two scientific CMOS cameras (ORCA-Flash4.0 V2, Hamamatsu, Japan) for dual-channel detection (**Fig. 1B$_3$**). A diode-pumped solid-state laser containing four wavelengths of 405 nm, 473 nm, 532 nm, and 589 nm (Laserglow Technologies, Toronto, Canada) was used as the illumination source (**Fig. 1B$_4$**). Three common light-sheet configurations were generated to illuminate the embryonic zebrafish heart (150–250 μm), adult zebrafish heart (500–1500 μm), and neonatal mouse heart (3000–5000 μm) (**Fig.1C$_1$**). The confocal region of the light-sheet was used as a uniform planar illumination and was finely stretched to cover the sample's transverse dimension (**Fig.1C$_2$**). The extent of axial projection was directly imaged at the waist of the light-sheet by the profiler, and the confocal range was further reconstructed by stacking the projections (**Fig. 1C$_2$**). The thickness of the light-sheet, defined as the axial full width at half maximum (FWHM) value of the beam waist, was measured at ~5 μm for the embryonic zebrafish heart (i), ~9 μm for the adult zebrafish heart (ii), and ~18 μm for the neonatal mouse heart (iii) (**Fig. 1C$_{1\text{-}2}$**). The lateral confocal regions with respect to these three axial extents were profiled (**Fig. 1C$_2$ i-iii**). The detection objectives were 10x/0.3 (Plan Fluor, Nikon, Japan) for the embryonic zebrafish heart, 4x/0.13 (Plan Fluor, Nikon, Japan) for the adult zebrafish heart, and 1x/0.25 (MVX10, Olympus, Japan) for the neonatal mouse heart to capture the full region-of-interest (ROI). Once the thickness of the light-sheet for excitation and the objective lens for detection were determined, the lateral and axial resolution for each configuration could be obtained by measuring the point spread function (PSF). The fluorescent point source (polystyrene beads) was imaged by applying the aforementioned three light-sheet configurations and demonstrated the lateral and axial resolution by measuring the FWHMs from x-y, x-z, and y-z plane images (**Fig. 1C$_3$**).

LSFM has the capacity to localize the 4D cellular phenomena with multi-fluorescence channels to study cardiovascular development and regeneration. Unlike commercial systems, including the ASI iSPIM, Zeiss Z.1, Leica SP8 and LaVision Ultramicroscope. Our multi-scale LSFM strategy is capable of rapid imaging acquisition to elucidate mechanisms of vascular regeneration after injury in the zebrafish cardiovascular system. In comparison with the ASI iSPIM, Zeiss Z.1 and Leica SP8 [29-32], we applied dry objective lenses with long-working distances to provide a large field-of-view. We further implemented a cylindrical lens to reshape the Gaussian beam to achieve high spatiotemporal resolution without the need for laser scanning the contracting heart [4, 27]. In addition, our system minimizes photo-bleaching and photo-toxicity due to the planar illumination [4]. In contrast to the LaVision Ultramicrope optimized for mouse brain [33], our LSFM system enables live imaging of zebrafish embryos. Furthermore, our custom-built system adapts a retrospective synchronization algorithm to reconstruct contracting embryonic hearts in 4D [27]. We have also demonstrated a resolution-enhancement method for using the objective lenses with low NA objectives, allowing for multi-scale imaging with a large field-of-view [34]. For these reasons, our custom-built LSFM has the capacity to perform the image-guided study for cardiovascular regeneration.

However, the main limitation of LSFM reside in photon scattering or absorption in the setting of imaging acquisition of large specimens (such as the rodent heart) or interfacing with mismatching refractive indices (from inadequate tissue clearing). Other limitations include the effect of out-of-focus light to reduce the signal-to-noise ratio. As a result of absorption, refraction, and scattering of coherent light within the tissue, these limitations generate stripe or shadow artifacts to attenuate the image. The lateral resolution of LSFM is lower than that of confocal imaging by the factor of $\sqrt{2}$ when the same objectives are used [35]. The advantages and disadvantages among the different optical modalities are summarized in **Table 1**.

1.1. Light-sheet imaging with automated segmentation method to analyze doxorubicin-induced cardiac injury and regeneration

In adult zebrafish, regenerating myocardium electrically couples with uninjured myocardium [36], providing a conserved cardiomyopathy model [37]. Precise assessment of cardiac ventricular architecture remains an imaging challenge due to the small size of the heart. The advent of the chemical clearing method enabled multi-scale imaging of hearts from zebrafish embryos (hundreds of μm in diameter) to adult fish (1-2 mm in diameter) [24, 26]. In the setting of a simplified tissue clearing method using benzyl alcohol-benzyl benzoate (BABB) to improve laser penetration and to achieve optical transparency, we visualized volumetric changes of cardiac morphology in adult zebrafish in response to doxorubicin-induced cardiac toxicity by combining light-sheet illumination with a customized automated segmentation method based on histogram analysis (**Fig. 2A**). Doxorubicin is an anthracycline agent that is commonly used in chemotherapy regimens for patients with a variety of cancers, and it is well known to cause cardiac injury, often limiting its use clinically [38]. The transgenic *Tg(cmlc2:GFP)* zebrafish line was used to visualize ventricular remodeling after doxorubicin chemotherapy. The detection objective is imaged through the liquid-air interface where it is introduced to a spherical aberration-based PSF extension [39]. The section thickness (1-5 μm) of mechanical scanning was determined based on the Nyquist-Shannon sampling theorem, while image acquisition was done with an exposure time of between 10-50 ms. Thus, the spatial resolution of the LSFM in cross-section varied from 1 μm to 10 μm, while the waist ω_0 ranged from 2 to 9 μm. Reconstructed image stacks underwent alpine interpolation and iterative 3D deconvolution to compensate under-sampling of the camera and to prevent blurred images. A 4-step automated image segmentation process was then applied to the input images for precise assessment of the structural reorganization of the adult zebrafish heart, as previously described [3]. Cardiac volumes assessed with automated segmentation were quantitatively compared following 3, 30, and 60 days of doxorubicin treatment (**Fig. 2B**). Our present data revealed 3 days of doxorubicin treatment led to global cardiac injury and resulted in the reduction of both endocardial and myocardial volumes, followed by ventricular remodeling at day 30, and complete regeneration and restoration of normal architecture at day 60. Furthermore, the automated segmentation method established a well-defined structure of the atrium, ventricle, and bulbus arteriosus, revealing ventricular trabeculae and ultrastructure (**Fig. 3A-B, D**). The computation of the angle between the atrio-ventricular (AV) valves and ventricular-bulbar (VB) valves permitted precise assessment, including the ventricular inflow (dotted yellow line) and outflow path (solid yellow line) (**Fig. 3C**). Our results accentuate the suitability of light-sheet imaging combined with automated segmentation as a high-throughput method to monitor 3D cardiac ultrastructural changes in adult zebrafish, with translational implications to drug discovery and modifiers of chemotherapy-induced cardiomyopathy.

1.2. LSFM to study mechano-transduction and vascular dynamics

With the use of the transgenic *Tg*(*flk1:GFP; Gata1:Ds-red*) zebrafish line which drives of the expressions of VEGFR2 as well as erythrocytes, we simultaneously detected circulating erythrocytes and demonstrated flow-mediated vascular regeneration. Our previous study established a zebrafish tail amputation model to seek mechanisms underlying vascular regeneration after injury [10]. The posterior tail segments of the embryos were amputated with a sterilized surgical scalpel under a stereomicroscope and immobilized with low melting agarose in a fluorinated ethylene propylene tube to achieve a uniform refractive index for fluorescence detection. Imaging cellular dynamics across large specimens requires high spatiotemporal resolution, uniform light-sheet thickness and low photo-bleaching/-toxicity. LSFM enables image acquisition of dynamic biophysical and biochemical activities such as blood flow or a beating heart at > 100 frames/sec. The precise alignment of dual-channel detection of LSFM further allows us to concurrently acquire the structure of the vasculature and circulating erythrocytes to perform 2D particle imaging velocimetry (PIV) in the dorsal aorta (DA) (**Fig. 4A-E**). The tail amputation model with LSFM offers a flexible platform to study hemodynamic regulation on endothelial vascular regeneration (**Fig. 4F-G**), providing an entry point to study mechano-transduction in a low Reynolds number system (Re: 100 ~ 1000). Besides, LSFM imaging has also been implemented in various developmental studies, such as 4D reconstruction of contracting zebrafish hearts [18, 27], time-lapse imaging of neural activity and cell lineages in *Drosophila* [40-44], *C. elegans* [32], zebrafish [19, 30, 45-49] and mice [50]. Unique characteristics of LSFM permit long-term imaging of cardiovascular regeneration and development. In comparison to the aforementioned studies, visualization of the periodic contractions of the embryonic heart requires either a 4D synchronization algorithm [18, 28,

[51] or a volumetric imaging method, while capturing dynamic blood flow in 4D is still underway.

2. Zebrafish tail amputation model to study vascular regeneration after injury

2.1. Exposure to ambient UFP reveals importance of Notch signaling for vascular regeneration

Ambient particulate matter ($PM_{2.5}$) in air pollutants is an emerging epigenetic factor in promoting endothelial dysfunction [52, 53]. Recent epidemiological studies have consistently supported that $PM_{2.5}$ exposure results in elevated risk of cancer, respiratory diseases, and cardiovascular defects during development [54-59]. UFP are a major sub-fraction of $PM_{2.5}$ and comprise a mixture of highly reactive organic chemicals [60] and transition metals [54, 61-63]. Exposure to UFP promotes Jun amino-terminal kinase (JNK) expression to produce a reactive oxygen species (ROS), thereby increasing vascular oxidative stress, and is also implicated in NF-κB-mediated inflammatory responses that induce atherosclerosis and vascular calcification [54, 62-67].

The Notch signaling pathway is an evolutionarily conserved intracellular signaling pathway intimately involved in cell-fate determination [68-72] and regulates initial sprout formation during angiogenesis [73-80]. Upon ligand binding, Notch receptors undergo proteolytic cleavages to release the Notch Intracellular Cytoplasmic Domain (NICD) under regulation of a disintegrin and metalloproteinases (ADAM) family. Following translocation to the nucleus, NICD forms a transcriptional activation complex to induce downstream Notch target genes, including Hairy and enhancer of split-1 (*Hes1*) and *gridlock* [68]. Ablation of Notch1 is associated with developmental retardation resulting in embryonic lethality, whereas dysregulated Notch1 activity in endothelial cells induces aberrant proliferation, resulting in a hyperplastic vascular network [81]. Missense mutation of the

Notch3 gene underlies the development of the degenerative vascular disease known as Cerebral Autosomal-Dominant Arteriopathy with Subcortical Infarcts and Leukoencephalopathy (CADASIL) [82].

To investigate whether UFP mitigate Notch-mediated vascular regeneration, we crossbred the Notch reporter transgenic fish *Tg(tp1:GFP)* with the *Tg(flk1:mCherry)* line to image Notch activity-mediated vascular regeneration. The Epstein-Barr Virus terminal protein 1 (tp1) reporter contains two Notch-responsive elements on the Rbp-Jĸ binding sites for NICD, thereby reporting regional Notch1b activation [27]. The control group developed vascular regeneration and formed a loop between the DA and the dorsal longitudinal anastomotic vessel (DLAV) with prominent endothelial Notch activity (as visualized in yellow) on the site of injury at 3 days post amputation (dpa). On the other hand, UFP exposure resulted in significant reduction of vascular endothelial Notch activity followed by disrupted vascular network formation on the injured site. The ADAM10 inhibitor, GI254023X, which inhibits proteolytic activation of the Notch receptor, recapitulated Notch-mediated impaired vascular regeneration. To further investigate whether the reduction of Notch signaling is associated with vascular impairment after the injury, we constructed dominant-negative *Notch1b* (DN-*Notch1b*) mRNA that attenuated Notch signaling by 96%. Approximately 75% of Notch-knockdown embryos underwent aberrant vascular regeneration and network formation, exhibiting embryonic lethality at 5 dpa. *NICD* mRNA micro-injection as a means to up-regulate Notch signaling restored UFP-, ADAM10 inhibitor-, and DN-*Notch1b* mRNA- attenuated Notch activity and consequent vascular regeneration. By using our well-established zebrafish tail amputation model, we provide a molecular basis to assess the effects of UFP on endothelial function for vascular regeneration (**Fig. 5**).

Epidemiological studies consistently support a link between maternal exposure to air pollutants and increased risk of congenital cardiovascular diseases [58]. UFP in air pollutants are the products of incomplete combustion from urban environmental sources, including diesel trucks and gasoline vehicles, and are enriched by elemental and polycyclic aromatic hydrocarbons [19]. Their large surface-to-volume ratio increases potential absorption to the pulmonary and cardiovascular systems [83-85]. UFP exposure via inhalation facilitates plasma lipid metabolite production and increases high-density lipoprotein oxidant capacity to accelerate atherosclerosis in LDLR-null mice [65]. UFP exposure further regulates atherogenic lipid metabolites and promotes macrophage infiltration in the intestine [19], where the composition of the micro-biota is altered to elevate atherogenic lipid metabolite levels. The emerging role of redox-sensitive micro-RNAs (miRs) have been implicated in cellular proliferation [86, 87]. $PM_{2.5}$ have been reported to modulate the levels of a number of miRNAs, including miR-223 and miR-375 [88-90]. Therefore, UFP could regulate the level of miRs for Notch inhibition [91].

Nevertheless, the mechanism underlying endothelial proliferation and vascular regeneration remains elusive due to the demand of high spatial and temporal resolution of real-time 3-D imaging. Scanning methods such as confocal or multi-photon microscopy are able to provide sufficient lateral resolution to reveal the biophysical dynamics at the cellular level but are confined to sequential raster scanning over the specimen. For instance, confocal microscopy allows for capturing angiogenic sprouts at a particular time but is limited in time-lapse imaging due to rapid photo-bleaching [92-94]. However, selective-plane illumination and concurrent detection in a 2D plane enable to implement time-lapse visualization of regenerating endothelial vasculature with the minimal photo-bleaching and photo-toxicity. The signal-to-noise ratio and axial resolution of LSFM are also improved due to planar illumination; otherwise, the focus of detection gradually degrades in the deep tissue. Therefore, the shorter exposure time, the deeper penetration depth, and the higher spatiotemporal resolution allow for time-lapse imaging of vascular regeneration and cellular dynamics in live zebrafish embryos, and LSFM provides the basis for revealing the mechanisms underlying cardiovascular regeneration and development.

2.2. Shear stress modulation of vascular dynamics and regeneration

Hemodynamic blood flow exerts shear stress, cyclic stretch, and hydrostatic pressure on the endothelium [95, 96]. While cyclic stretch plays an important role in maintaining endothelial function, it is well recognized that hemodynamic shear forces mechanically and metabolically modulate vascular endothelial function [97-99]. A complex flow profile develops at the arterial bifurcations, where flow separation and migrating stagnation points create disturbed flow (DF), mediating the focal and eccentric nature of atherosclerotic lesions [100-106]. A recent study examined the role of laminar shear stress in driving expression of vascular endothelial growth factor (VEGF) and endothelial nitric oxide synthase (eNOS)-mediated Protein Kinase C isoform epsilon (PKCε) to modulate endothelial cell (EC) proliferation and lumen formation [107, 108]. Unidirectional pulsatile (PSS) and oscillatory shear stress (OSS) differentially modulate the canonical Wnt/β-catenin pathway to modulate vascular development and regeneration [2, 109], while also being implicated in the differentiation of vascular progenitors during angiogenesis [110, 111]. Endothelial glycolysis is mechano-responsive [112], and ECs are highly glycolytic [113]. ECs further increase the level of glycolytic flux when switching from quiescence to a proliferative state, while the glycolytic enzyme, 6-phosphofructo-2-kinase/fructose-2,6-biphosphatase 3 (PFKFB3), localizes in lamellipodia [114]. As a critical regulator of glycolysis, PFKFB3 further involves lamellipodia/filopodia extension during vessel formation [113, 114]. Laminar shear stress modulates the expression of Krüppel-like factor 2 (KLF2) to suppress PFKFB3-mediated endothelial glycolysis and vessel sprouting [115], whereas disturbed flow mitigates mitochondrial respiration and increases basal glycolysis and glycolytic capacity [116].

Our recent study with zebrafish supports the notion that PSS and OSS differentially modulate VEGFR-PKCε signaling to induce PFKFB3-mediated glycolytic metabolites for vascular repair [10]. Use of embryonic zebrafish allowed for genetic manipulation of blood viscosity to alter the level of endothelial wall shear stress [117] to modulate the PKCε-PFKFB3 pathway *in vivo* (**Fig. 6A**). *Gata1a* morpholino oligonucleotide (MO) micro-injection prevented erythrocyte production, thereby reducing the level of viscosity-mediated shear stress compared to control (**Fig. 6Ai-ii**). [5, 118]. On the other hand, *EPO* mRNA micro-injection resulted in elevated erythrocytosis as a means of augmenting viscosity-mediated wall shear stress (**Fig. 6Aiii**) [119]. In the transgenic *Tg(flk1:GFP)* zebrafish model of tail regeneration, control *p53* MO injection demonstrated vascular regeneration, as visualized by a closed loop between the DA and the DLAV at 3 dpa. In contrast, suppressing the level of PKCε with MO injection developed aberrant vascular regeneration. Furthermore, micro-injection of *Gata1a* MO delayed vascular regeneration from 3 dpa to 5 dpa. The micro-injection of cardiac troponin T2 (*Tnnt2*) MO to arrest myocardial contraction and subsequent blood flow further attenuated vascular regeneration at 3 dpa, while embryos failed to thrive at 5 dpa. On the other hand, erythropoietin (*EPO*) mRNA micro-injection promoted tail regeneration. As a corollary, *PKCε* mRNA restored vascular regeneration in *Gata1a* MO injected embryos at 3 and 5 dpa (**Fig. 6B**).

In reference to our metabolomic analysis via gas chromatography time-of-flight mass spectrometry (GC-TOF), we elucidated that shear stress regulates glycolytic metabolites, including glucose ($C_6H_{12}O_6$), fructose ($C_6H_{12}O_6$), and dihydroxyacetone ($C_3H_6O_3$, DHA) via PFKFB3. In the zebrafish tail amputation model, exposure to DHA increased the proportion of zebrafish embryos with complete regeneration in the control group, whereas it rescued vascular repair in the absence of PKCε (**Fig. 7**). Our findings support that flow-responsive PKCε modulates endothelial glycolytic metabolites that are implicated in vascular regeneration. The advent of high-throughput "omics" approaches, including epigenomics, transcriptomics, miRnomics, proteomics, and metabolomics [120], has provided new mechanotransduction strategies to discover biomarkers with therapeutic targets.

Current scanning methods are limited by their sequential point-scanning strategy in 2D planes, being insufficient to elucidate hemodynamic shear forces during cardiac morphogenesis. Unlike conventional bright-field microscopy, LSFM applies orthogonal illumination and detection, enabling investigators to selectively localize mechano-transduction to the endocardial endothelial lining within an ultra-thin plane of the sample. Due to the rapid multi-channel detection at the single cellular level, LSFM allows for the simultaneous imaging of the blood flow at the injured site and 3D structure of the vessels, elucidating hemodynamics with underlying the initiation of endocardial trabeculation during cardiac development [27]. In conclusion, LSFM allows for rapid tracking of fluorescently labeled targets in multiple channels, thereby providing a computational basis to quantify blood flow and hemodynamic shear forces.

Conclusion and Outlook

Zebrafish have been utilized as an emerging developmental model due to a conserved physiology and anatomy with mammals. Its optical transparency at the embryonic stage facilitates direct observation of organogenesis including cardiovascular morphogenesis. While zebrafish comprise a well-established genetic system for studying cardiovascular development and disease, zebrafish demonstrate unique regenerative capacity in response to anatomical or chemotherapy-induced injury. Both high spatiotemporal resolution and deep tissue penetration are required to tracking cardiovascular dynamics, such as the regenerating ventricular ultrastructure. Therefore, LSFM is suitable to monitor spatiotemporal variations of the regenerating cardiovascular system with minimal photo-bleaching /-toxicity, and is also a promising approach to track single blood cells as well as estimating the parabolic velocity distribution of blood flow in the embryonic zebrafish model. In addition, parallel advances in deep learning and virtual reality may lead us to more precisely elucidating cardiovascular architecture and function in future studies. Developing a novel convolutional or recurrent neural network for automatic segmentation will benefit image post-processing procedures that are otherwise limited in accuracy and efficiency by manual segmentation in the setting of large data sets [121-123]. The study of interactive virtual reality establishes an efficient and robust framework for creating a user-directed microenvironment in which we are able to unravel developmental cardiac mechanics and physiology with high spatiotemporal resolution [28, 124-126]. In this review, we address our zebrafish model of injury with a mechanistic approach to understand cardiovascular regeneration. Furthermore, our findings with zebrafish combined with multi-scale light-sheet imaging demonstrate the advantages of light-sheet imaging, highlighting its role as a novel imaging strategy that can illuminate the mechanisms of cardiovascular injury and repair and further advance the field.

Acknowledgements

This study was supported by the National Institutes of Health HL118650 (T.K.H.), HL083015 (T.K.H.), HL111437 (T.K.H.), HL129727 (T.K.H.), T32 training grant HL007895 (J.J.H.), and an AHA Scientist Development Grant 16SDG30910007 (R.R.S.P). Chapter II is a reprint of the article: Baek KI*, Ding YC*, Chang CC*, Chang M, Packard RRS, Hsu JJ, Fei P, Hsiai TK. Advanced microscopy to elucidate cardiovascular injury and regeneration: 4D light-sheet imaging. Prog Biophys Mol Biol. 138, 105-115, 2018, (https://doi.org10.1016/j.pbiomolbio.2018.05.003). Reprint was reproduced with permission from the publisher and all of the co-authors of the publication.

FIGURES

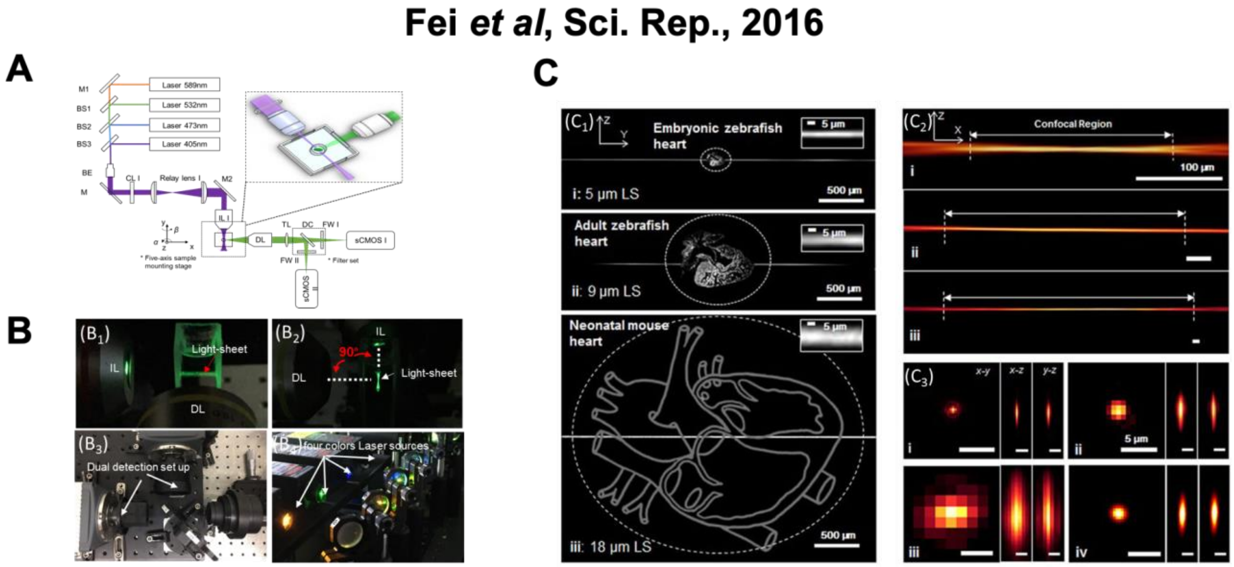

Figure 1. Schematic diagram and performance of the fluorescent light-sheet microscope (**A**) Four collimated laser sources were focused through a cylindrical lens and transmitted by illumination lens (IL) to generate a light-sheet sectioning the sample. The objective lens (DL) was positioned orthogonally to the illumination path for fluorescence detection. In addition, the dual-channel detection was achieved using a dichroic mirror and filter sets at the detection arm. The focus of detection needs to be exactly conjugated to the illuminated plane. **(B_1)** The formation of the light-sheet from the illumination objectives and detected by detection objectives. **(B_2)** Top view of the light-sheet demonstrated orthogonal relation between IL and DL. **(B_3)** Four laser wavelengths offer flexibility for different fluorophores. M: mirror; DC: dichroic mirror; BE: beam expander; CL: cylindrical lens; SL: scan lens; TL: tube lens; FW: filter wheel; IL: illumination lens; DL: detection lens. **(B_4)** The two orthogonal cameras allowed for the capability of simultaneous dual-channel detection. **(C_1)** The axial confinement of the light-sheet was used for sectioning the (i) embryonic zebrafish, (ii) adult zebrafish, and (iii) neonatal mouse hearts. LS: light-sheet. **(C_2)** The changes in confocal region corresponded to the area available for light-sheet sectioning. The double-headed arrow line indicates the confocal region, in which

the light-sheet is considered to be uniform. The scale bars are 100 µm in length for the sub-images in (i), (ii) and (iii). **(C_3)** Imaging a 400 nm fluorescent bead (sub-resolution point source) was compared with the (i) 5 µm LS detected by the 20x/0.5 DL, (ii) 9 µm LS by 10x/0.3 DL, (iii) 18 µm LS by 4x/0.13 DL and (iv) 18 µm LS by 4x/0.13 DL, with resolution enhancement applied. Reproduced in this dissertation with permission from Baek, Ding, Chang *et al*.

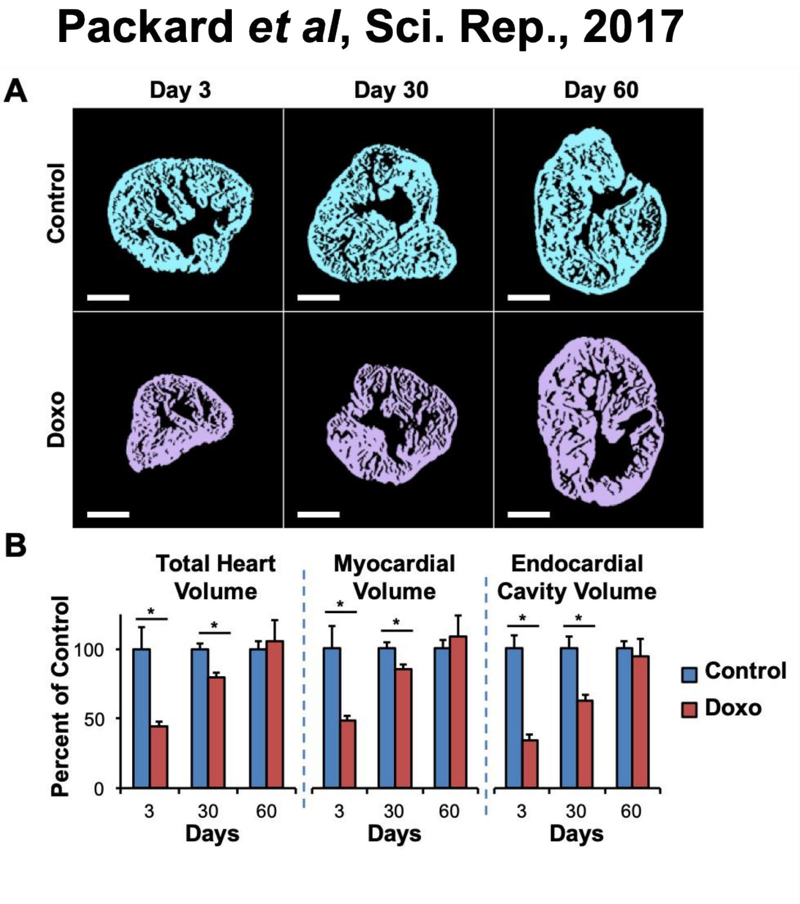

Figure 2. Light-sheet imaging to analyze doxorubicin-induced cardiac injury and regeneration Adult zebrafish hearts were isolated at days 3, 30, 60 following intraperitoneal treatment with doxorubicin or control vehicle. **(A)** Control zebrafish hearts exhibited a preserved architecture during the study period. Treatment of doxorubicin induced a dramatic cardiac remodeling leading to an acute reduction in size at day 3, followed by a gradual increase at day 30, and normalization at day 60. **(B)** Total heart, myocardial, and endocardial volumes were quantitatively compared to control values demonstrating the regeneration process following doxorubicin-induced injury (** $P < 0.01$ vs control). Doxo: doxorubicin. Scale bar: 200 μm. Reproduced in this dissertation with permission from Baek, Ding, Chang *et al*.

Packard *et al*, Sci. Rep., 2017

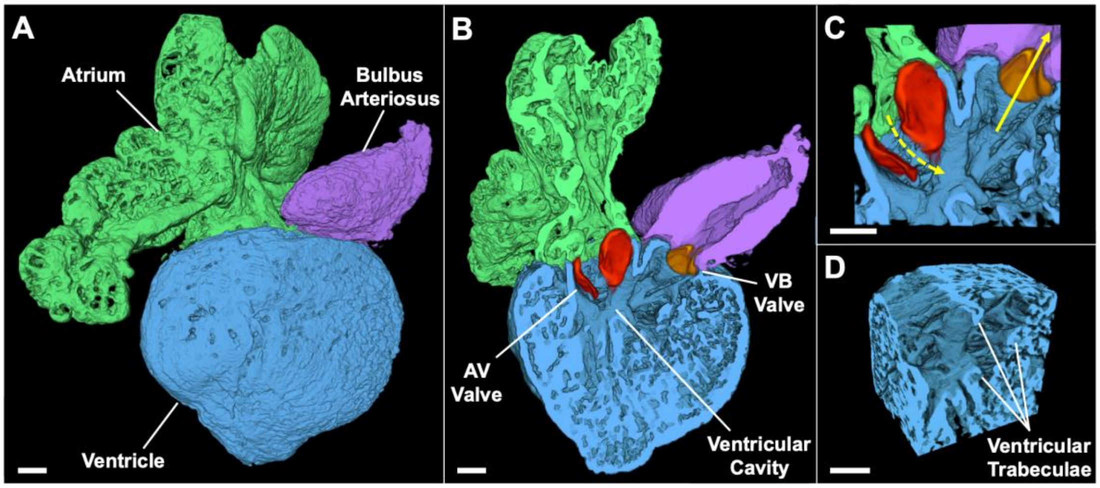

Figure 3. 3D rendering of the adult zebrafish heart **(A)** 3-D rendering combined with automated segmentation method provided anatomic structures of the intact atrium, ventricle, and bulbous arteriosus in adult zebrafish heart. **(B)** Precise assessment of zebrafish heart with automated segmentation established a cross-section through the atrium, ventricle, and bulbous arteriosus and demonstrated 2 leaflets of the AV valve (red) and of the VB valve (orange). **(C)** Ventricular inflow (dotted yellow line) and outflow path (solid yellow line) were estimated with computation of the angle between the atrioventricular (AV) valves and ventricular-bulbar (VB) valves. Scale bar: 100 µm. Reproduced in this dissertation with permission from Baek, Ding, Chang *et al*.

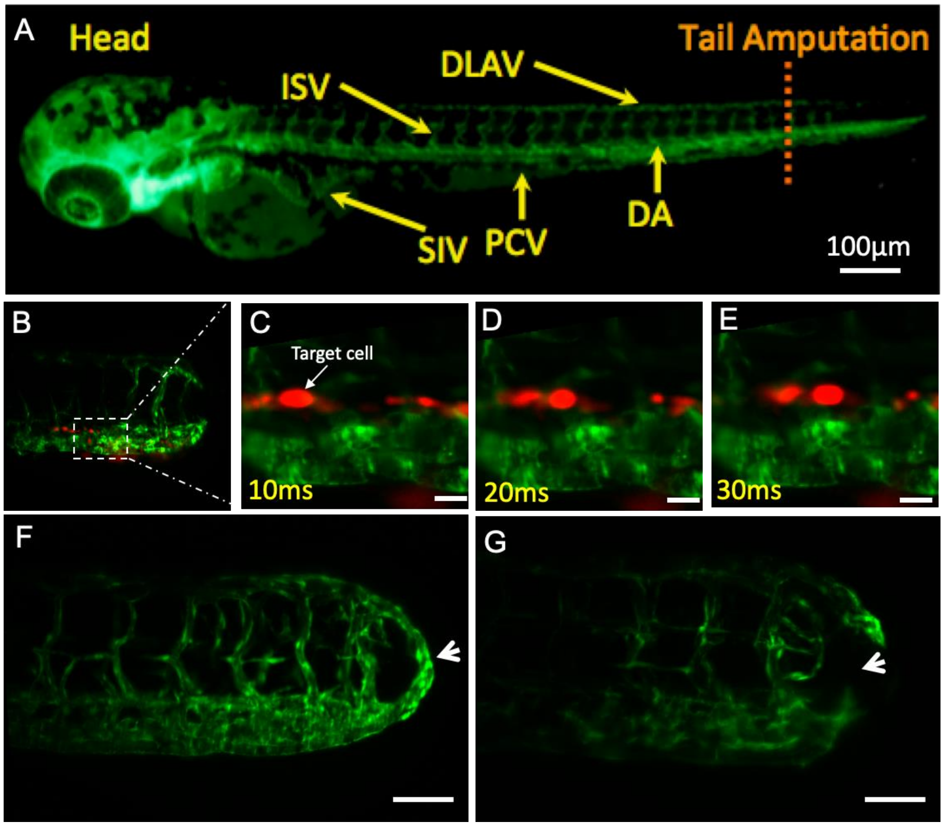

Figure 4. Light-sheet imaging of vascular regeneration and circulating erythrocytes in response to tail amputation **(A)** An inverted fluorescence image demonstrated the vasculature (green) and amputation region (dashed line) of a transgenic *Tg(flk1:GFP; Gata1:Ds-Red)* zebrafish embryo at 3 dpf. ISV: intersegmental vessel; DLAV: dorsal longitudinal anastomotic vessel; SIV: subintestinal vessel; PCV: posterior cardinal vein; DA: dorsal aorta. **(B)** LSFM imaging of the erythrocytes (red) adjacent to the site of amputation and regeneration. The dashed white box indicated locations of higher power images in the subsequent panels **(C-E)**. An individual erythrocyte (red) in relation to the vascular endothelial layer (green) was tracked under LSFM at 100 fps. The travel distance and net velocity of each erythrocyte could be measured from the corresponding location difference among images **(C)**, **(D)** and **(E).** The complete **(F)** and incomplete **(G)** vascular regeneration between DLAV and DA were revealed in separate zebrafish embryos at 3 days after tail amputation. Scale bars: 25 µm. Reproduced in this dissertation with permission from Baek, Ding, Chang *et al*.

Baek *et al*, *Antioxid Redox Signal*, 2018

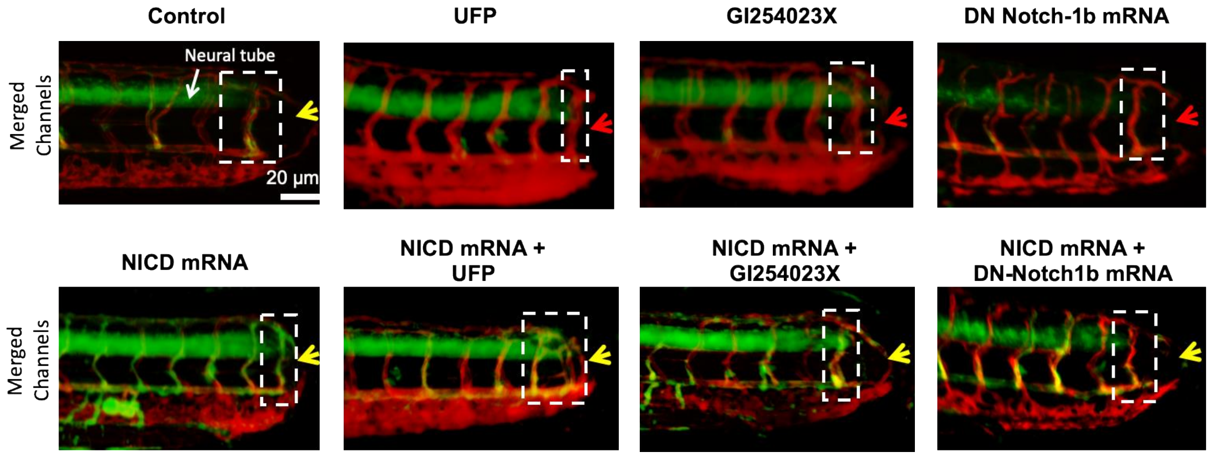

Figure 5. Ambient UFP exposure impaired Notch-mediated vascular regeneration. Transgenic *Tg(tp1:GFP; flk1:mCherry)* zebrafish embryos revealed Notch activity in the vasculature, as indicated by the overlapped yellow color, corroborating the role of endothelial Notch activity in the site of vascular repair. The control group developed vascular regeneration at 3 days post tail amputation (dpa). UFP or ADAM 10 inhibitor (GI254023X) treatment attenuated endothelial Notch activity in the site of injury and impaired vascular regeneration. Injection of dominant negative (DN)-*Notch1b* mRNA further attenuated Notch signaling-mediated vascular regeneration. As a corollary, *NICD* mRNA injection upregulated Notch activity and rescued UFP-, ADAM10 inhibitor- or DN-*Notch1b* mRNA-impaired vascular regeneration. Reproduced in this dissertation with permission from Baek, Ding, Chang *et al*.

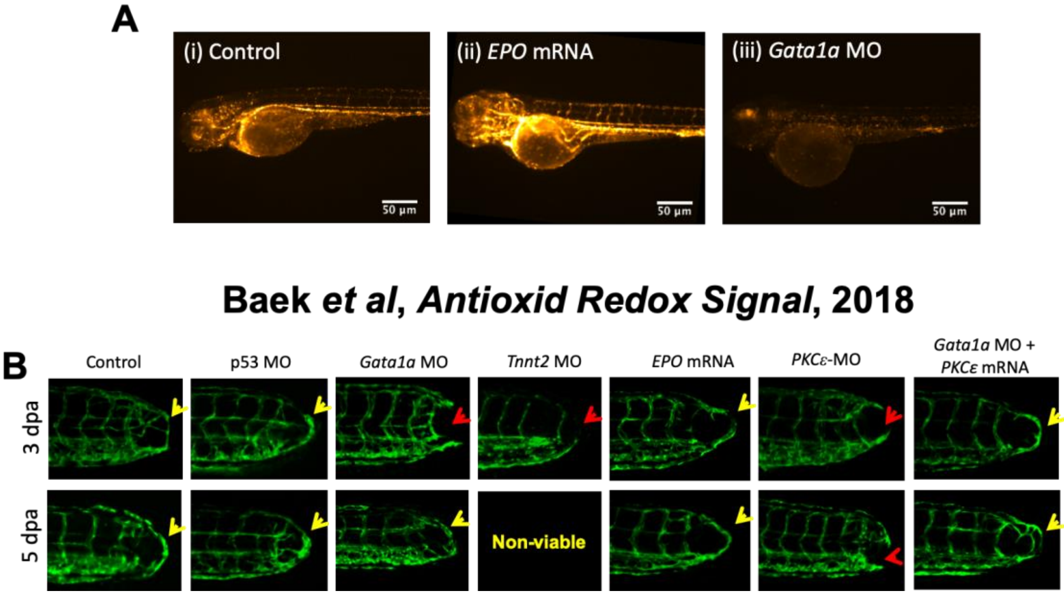

Baek *et al*, *Antioxid Redox Signal*, 2018

Figure 6. Shear stress is implicated in *PKCε*-dependent vascular repair. **(A)** Blood viscosity of the embryonic zebrafish was genetically manipulated to alter the level of endothelial wall shear stress. Compared to control embryos, micro-injection of *Gata1a* MO reduced the level of erythropoiesis and consequent wall shear stress, whereas erythropoietin (*EPO*) mRNA resulted in the opposite effect. **(B)** The control and *p53* MO-injected fish developed vascular repair at 3 dpa (yellow arrows). Reduction of viscosity-mediated shear stress with *Gata1a* MO delayed vascular repair from 3 dpa to 5 dpa. The presence of *Tnnt2* MO to arrest myocardial contractility led impaired vascular repair at 3 dpa, while embryos failed to thrive at 5 dpa (red arrow). On the other hand, increased level of erythropoiesis with *EPO* mRNA promoted vascular regeneration. Silencing *PKCε* with MO attenuated vascular repair at both 3 and 5 dpa, whereas upregulation of *PKCε* mRNA restored vascular impairment in *Gata1a* MO injected embryos. Reproduced in this dissertation with permission from Baek, Ding, Chang *et al*.

Baek *et al*, *Antioxid Redox Signal*, 2018

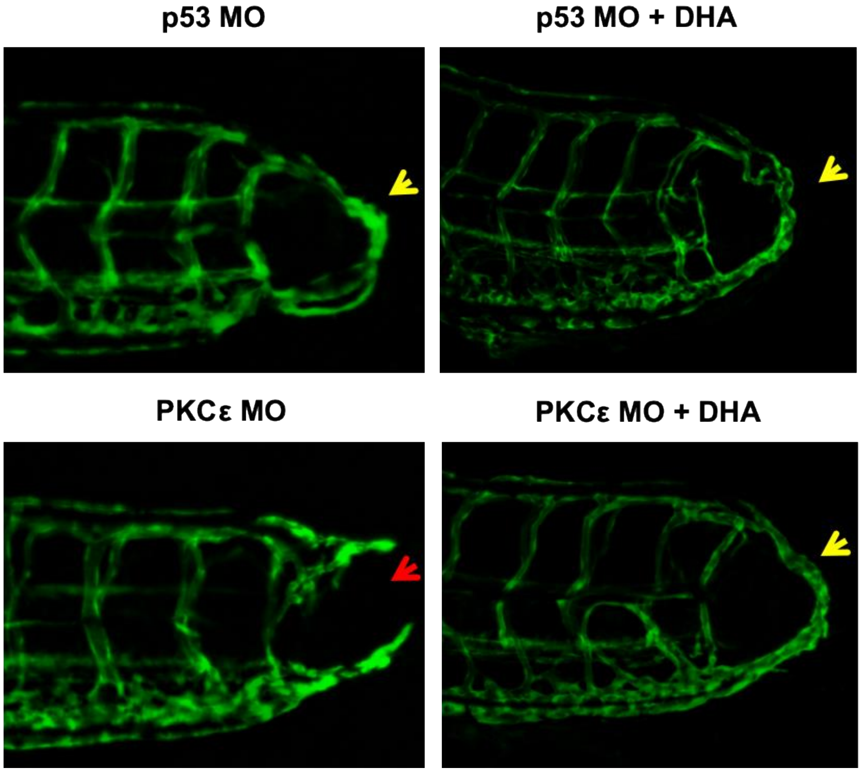

Figure 7. Glycolytic metabolite, dihydroxyacetone (DHA) promoted vascular regeneration. Transgenic *Tg(flk1:GFP)* embryos injected with control *P53* MO or *PKCε* MO were treated with or without DHA at 1mg/mL for 3 days after initial vascular injury. Micro-injection of *PKCε* MO resulted in impaired vascular regeneration (red arrow), whereas DHA treatment reversed the effect of *PKCε* MO and promoted vascular regeneration (yellow arrows). Reproduced in this dissertation with permission from Baek, Ding, Chang *et al*.

Table 1: Comparative advantages and disadvantages among different imaging modalities

Method	Lateral-Axial Resolution (nm)	Penetration (μm)	Image acquisition time	Advantage	Disadvantage
LSFM	200-500	>1000	ms-s	Low phototoxicity	Big data
CFM	200-400	150	s-mins	Optical sectioning	Scanning
WFM	250	---	ms-mins	Low cost, user-friendly design	Low contrast
SD-CFM	200-400	150	s-mins	Rapid Image acquisition	Fixed pinhole
MPM	300-500	1000	ms-mins	Penetration depth, intrinsic confocality	Requires high power pulsed laser
STED	80-400	50	s-mins	High resolution at confocal speed	Significant photobleaching
PALM/STORM	50-100	0.1	mins-hr	Extremely high resolution	Slow image acquisition

LSFM: light-sheet fluorescence microscopy; CFM: confocal microscopy; WFM: wide-field microscopy; SD-CFM: spinning disk confocal microscopy; MPM: multi-photon microscopy; STED: stimulated emission depletion; PALM: photo-activated localization microscopy; STORM: stochastic optical reconstruction microscopy. Adapted from Ding Y et al., Curr. Cardiol. Rep., 2018.

References

1. Tzahor E, Poss KD. Cardiac regeneration strategies: Staying young at heart. *Science*. 2017;356:1035-1039

2. Li R, Beebe T, Jen N, Yu F, Takabe W, Harrison M, Cao H, Lee J, Yang H, Han P, Wang K, Shimizu H, Chen J, Lien CL, Chi NC, Hsiai TK. Shear stress-activated wnt-angiopoietin-2 signaling recapitulates vascular repair in zebrafish embryos. *Arterioscler Thromb Vasc Biol*. 2014;34:2268-2275

3. Packard RRS, Baek KI, Beebe T, Jen N, Ding Y, Shi F, Fei P, Kang BJ, Chen P-H, Gau J. Automated segmentation of light-sheet fluorescent imaging to characterize experimental doxorubicin-induced cardiac injury and repair. *Sci. Rep.* 2017;7:8603

4. Power RM, Huisken J. A guide to light-sheet fluorescence microscopy for multiscale imaging. *Nature methods*. 2017;14:360

5. Vermot J, Forouhar AS, Liebling M, Wu D, Plummer D, Gharib M, Fraser SE. Reversing blood flows act through klf2a to ensure normal valvulogenesis in the developing heart. *PLoS biology*. 2009;7:e1000246

6. Opitz R, Maquet E, Huisken J, Antonica F, Trubiroha A, Pottier G, Janssens V, Costagliola S. Transgenic zebrafish illuminate the dynamics of thyroid morphogenesis and its relationship to cardiovascular development. *Developmental biology*. 2012;372:203-216

7. Sun P, Zhang Y, Yu F, Parks E, Lyman A, Wu Q, Ai L, Hu C-H, Zhou Q, Shung K. Micro-electrocardiograms to study post-ventricular amputation of zebrafish heart. *Ann. Biomed. Eng.* 2009;37:890-901

8. Herzog W, Müller K, Huisken J, Stainier DY. Genetic evidence for a noncanonical function of seryl-trna synthetase in vascular development. *Circulation research*. 2009;104:1260-1266

9. Baek KI, Packard RRS, Hsu JJ, Saffari A, Ma Z, Luu AP, Pietersen A, Yen H, Ren B, Ding Y. Ultrafine particle exposure reveals the importance of foxo1/notch activation complex for vascular regeneration. *Antioxidants & redox signaling*. 2018;28:1209-1223

10. Baek KI, Li R, Jen N, Choi H, Kaboodrangi A, Ping P, Liem D, Beebe T, Hsiai TK. Flow-responsive vascular endothelial growth factor receptor-protein kinase c isoform epsilon signaling mediates glycolytic metabolites for vascular repair. *Antioxid Redox Signal*. 2018;28:31-43

11. Amos B. Lessons from the history of light microscopy. *Nat Cell Biol*. 2000;2:E151-152

12. Yuste R. Fluorescence microscopy today. *Nat Methods*. 2005;2:902-904

13. Ntziachristos V, Ripoll J, Wang LV, Weissleder R. Looking and listening to light: The evolution of whole-body photonic imaging. *Nat. Biotechnol.* 2005;23:313-320

14. Huisken J, Swoger J, Del Bene F, Wittbrodt J, Stelzer EH. Optical sectioning deep inside live embryos by selective plane illumination microscopy. *Science*. 2004;305:1007-1009

15. Keller PJ, Stelzer EHK. Quantitative in vivo imaging of entire embryos with digital scanned laser light sheet fluorescence microscopy. *Curr Opin Neurobiol*. 2008;18:624-632

16. Kobat D, Horton NG, Xu C. In vivo two-photon microscopy to 1.6-mm depth in mouse cortex. *J. Biomed. Opt.* 2011;16:106014-106014-106014

17. Horton NG, Wang K, Kobat D, Clark CG, Wise FW, Schaffer CB, Xu C. In vivo three-photon microscopy of subcortical structures within an intact mouse brain. *Nat. Photon.* 2013;7:205-209

18. Mickoleit M, Schmid B, Weber M, Fahrbach FO, Hombach S, Reischauer S, Huisken J. High-resolution reconstruction of the beating zebrafish heart. *Nature methods*. 2014;11:919

19. Chhetri RK, Amat F, Wan Y, Höckendorf B, Lemon WC, Keller PJ. Whole-animal functional and developmental imaging with isotropic spatial resolution. *Nature methods*. 2015;12:1171

20. Huisken J, Stainier DY. Selective plane illumination microscopy techniques in developmental biology. *Development*. 2009;136:1963-1975

21. Santi PA. Light sheet fluorescence microscopy: A review. *J. Histochem. Cytochem.* 2011;59:129-138

22. De Vos WH, Beghuin D, Schwarz CJ, Jones DB, van Loon JJ, Bereiter-Hahn J, Stelzer EH. Invited review article: Advanced light microscopy for biological space research. *Rev. Sci. Instr.* 2014;85:101101

23. Sideris E, Griffin DR, Ding Y, Li S, Weaver WM, Di Carlo D, Hsiai T, Segura T. Particle hydrogels based on hyaluronic acid building blocks. *ACS Biomater. Sci. Engin.* 2016;2:2034-2041

24. Sung K, Ding Y, Ma J, Chen H, Huang V, Cheng M, Yang CF, Kim JT, Eguchi D, Carlo DD, Hsiai TK, Nakano A, Kulkarni RP. Simplified three-dimensional tissue clearing and incorporation of colorimetric phenotyping. *Sci. Rep.* 2016;6:30736

25. Ding Y, Lee J, Ma J, Sung K, Yokota T, Singh N, Dooraghi M, Abiri P, Wang Y, Kulkarni RP. Light-sheet fluorescence imaging to localize cardiac lineage and protein distribution. *Sci. Rep.* 2017;7:42209

26. Fei P, Lee J, Packard RRS, Sereti K-I, Xu H, Ma J, Ding Y, Kang H, Chen H, Sung K. Cardiac light-sheet fluorescent microscopy for multi-scale and rapid imaging of architecture and function. *Scientific reports*. 2016;6:22489

27. Lee J, Fei P, Packard RRS, Kang H, Xu H, Baek KI, Jen N, Chen J, Yen H, Kuo C-CJ. 4-dimensional light-sheet microscopy to elucidate shear stress modulation of cardiac trabeculation. *The Journal of clinical investigation*. 2016;126:1679-1690

28. Baek KI, Packard RR, Hsu JJ, Saffari A, Ma Z, Luu AP, Pietersen A, Yen H, Ren B, Ding Y, Sioutas C, Li R, Hsiai TK. Ultrafine particles exposure reveals the importance of foxo1/notch activation complex for vascular regeneration. *Antioxid Redox Signal*. 2017

29. Keller PJ, Schmidt AD, Wittbrodt J, Stelzer EH. Reconstruction of zebrafish early embryonic development by scanned light sheet microscopy. *science*. 2008;322:1065-1069

30. Wu Y, Wawrzusin P, Senseney J, Fischer RS, Christensen R, Santella A, York AG, Winter PW, Waterman CM, Bao Z. Spatially isotropic four-dimensional imaging with dual-view plane illumination microscopy. *Nature biotechnology*. 2013;31:1032

31. Kumar A, Wu Y, Christensen R, Chandris P, Gandler W, McCreedy E, Bokinsky A, Colón-Ramos DA, Bao Z, McAuliffe M. Dual-view plane illumination microscopy for rapid and spatially isotropic imaging. *nature protocols*. 2014;9:2555

32. Wu Y, Ghitani A, Christensen R, Santella A, Du Z, Rondeau G, Bao Z, Colon-Ramos D, Shroff H. Inverted selective plane illumination microscopy (ispim) enables

coupled cell identity lineaging and neurodevelopmental imaging in caenorhabditis elegans. *Proc Natl Acad Sci U S A*. 2011;108:17708-17713

33. Dodt H-U, Leischner U, Schierloh A, Jährling N, Mauch CP, Deininger K, Deussing JM, Eder M, Zieglgänsberger W, Becker K. Ultramicroscopy: Three-dimensional visualization of neuronal networks in the whole mouse brain. *Nature methods*. 2007;4:331

34. Fei P, Nie J, Lee J, Ding Y, Li S, Yu Z, Zhang H, Hagiwara M, Yu T, Segura T. Sub-voxel light-sheet microscopy for high-resolution, high-throughput volumetric imaging of large biomedical specimens. *bioRxiv*. 2018:255695

35. Cannell M, McMorland A, Soeller C, Pawley J. Handbook of biological confocal microscopy. 2006

36. Lee J, Cao H, Kang BJ, Jen N, Yu F, Lee C-A, Fei P, Park J, Bohlool S, Lash-Rosenberg L. Hemodynamics and ventricular function in a zebrafish model of injury and repair. *Zebrafish*. 2014;11:447-454

37. Ding Y, Sun X, Huang W, Hoage T, Redfield M, Kushwaha S, Sivasubbu S, Lin X, Ekker S, Xu X. Haploinsufficiency of target of rapamycin attenuates cardiomyopathies in adult zebrafishnovelty and significance. *Circ. Res.* 2011;109:658-669

38. Volkova M, Russell R, 3rd. Anthracycline cardiotoxicity: Prevalence, pathogenesis and treatment. *Curr Cardiol Rev*. 2011;7:214-220

39. Tomer R, Lovett-Barron M, Kauvar I, Andalman A, Burns VM, Sankaran S, Grosenick L, Broxton M, Yang S, Deisseroth K. Sped light sheet microscopy: Fast mapping of biological system structure and function. *Cell*. 2015;163:1796-1806

40. Keller PJ, Schmidt AD, Santella A, Khairy K, Bao Z, Wittbrodt J, Stelzer EH. Fast, high-contrast imaging of animal development with scanned light sheet-based structured-illumination microscopy. *Nat Methods*. 2010;7:637-642

41. Truong TV, Supatto W, Koos DS, Choi JM, Fraser SE. Deep and fast live imaging with two-photon scanned light-sheet microscopy. *Nat Methods*. 2011;8:757-760

42. Ahrens MB, Orger MB, Robson DN, Li JM, Keller PJ. Whole-brain functional imaging at cellular resolution using light-sheet microscopy. *Nat Methods*. 2013;10:413-420

43. Tomer R, Khairy K, Amat F, Keller PJ. Quantitative high-speed imaging of entire developing embryos with simultaneous multiview light-sheet microscopy. *Nat Methods*. 2012;9:755-763

44. Vladimirov N, Mu Y, Kawashima T, Bennett DV, Yang CT, Looger LL, Keller PJ, Freeman J, Ahrens MB. Light-sheet functional imaging in fictively behaving zebrafish. *Nat Methods*. 2014;11:883-884

45. Bassi A, Schmid B, Huisken J. Optical tomography complements light sheet microscopy for in toto imaging of zebrafish development. *Development*. 2015;142:1016-1020

46. Schmid B, Shah G, Scherf N, Weber M, Thierbach K, Campos CP, Roeder I, Aanstad P, Huisken J. High-speed panoramic light-sheet microscopy reveals global endodermal cell dynamics. *Nat Commun*. 2013;4:2207

47. Weber M, Scherf N, Meyer AM, Panakova D, Kohl P, Huisken J. Cell-accurate optical mapping across the entire developing heart. *Elife*. 2017;6

48. Forouhar AS, Liebling M, Hickerson A, Nasiraei-Moghaddam A, Tsai H-J, Hove JR, Fraser SE, Dickinson ME, Gharib M. The embryonic vertebrate heart tube is a dynamic suction pump. *Science*. 2006;312:751-753

49. Lenard A, Daetwyler S, Betz C, Ellertsdottir E, Belting H-G, Huisken J, Affolter M. Endothelial cell self-fusion during vascular pruning. *PLoS biology*. 2015;13:e1002126

50. Bouchard MB, Voleti V, Mendes CS, Lacefield C, Grueber WB, Mann RS, Bruno RM, Hillman EM. Swept confocally-aligned planar excitation (scape) microscopy for high-speed volumetric imaging of behaving organisms. *Nature photonics*. 2015;9:113

51. Liebling M, Forouhar AS, Gharib M, Fraser SE, Dickinson ME. Four-dimensional cardiac imaging in living embryos via postacquisition synchronization of nongated slice sequences. *J Biomed Opt*. 2005;10:054001

52. Karimi Galougahi K, Ashley EA, Ali ZA. Redox regulation of vascular remodeling. *Cell Mol Life Sci*. 2016;73:349-363

53. Minicucci MF, Azevedo PS, Paiva SA, Zornoff LA. Cardiovascular remodeling induced by passive smoking. *Inflamm Allergy Drug Targets*. 2009;8:334-339

54. Brook RD, Rajagopalan S, Pope CA, 3rd, Brook JR, Bhatnagar A, Diez-Roux AV, Holguin F, Hong Y, Luepker RV, Mittleman MA, Peters A, Siscovick D, Smith SC, Jr., Whitsel L, Kaufman JD, American Heart Association Council on E, Prevention CotKiCD, Council on Nutrition PA, Metabolism. Particulate matter air pollution and cardiovascular disease: An update to the scientific statement from the american heart association. *Circulation*. 2010;121:2331-2378

55. Brunekreef B, Holgate ST. Air pollution and health. *Lancet*. 2002;360:1233-1242

56. Gorham ED, Garland CF, Garland FC. Acid haze air pollution and breast and colon cancer mortality in 20 canadian cities. *Can J Public Health*. 1989;80:96-100

57. Ritz B, Yu F, Fruin S, Chapa G, Shaw GM, Harris JA. Ambient air pollution and risk of birth defects in southern california. *American journal of epidemiology*. 2002;155:17-25

58. Dadvand P, Rankin J, Rushton S, Pless-Mulloli T. Ambient air pollution and congenital heart disease: A register-based study. *Environmental research*. 2011;111:435-441

59. Hwang BF, Lee YL, Jaakkola JJ. Air pollution and the risk of cardiac defects: A population-based case-control study. *Medicine*. 2015;94:e1883

60. Sardar SB, Fine PM, Mayo PR, Sioutas C. Size-fractionated measurements of ambient ultrafine particle chemical composition in los angeles using the nanomoudi. *Environ Sci Technol*. 2005;39:932-944

61. Lough GC, Schauer JJ, Park JS, Shafer MM, Deminter JT, Weinstein JP. Emissions of metals associated with motor vehicle roadways. *Environ Sci Technol*. 2005;39:826-836

62. Nel A, Xia T, Madler L, Li N. Toxic potential of materials at the nanolevel. *Science*. 2006;311:622-627

63. Zhang Y, Schauer JJ, Shafer MM, Hannigan MP, Dutton SJ. Source apportionment of in vitro reactive oxygen species bioassay activity from atmospheric particulate matter. *Environ Sci Technol*. 2008;42:7502-7509

64. Li R, Ning Z, Cui J, Khalsa B, Ai L, Takabe W, Beebe T, Majumdar R, Sioutas C, Hsiai T. Ultrafine particles from diesel engines induce vascular oxidative stress via jnk activation. *Free Radic Biol Med*. 2009;46:775-782

65. Li R, Navab M, Pakbin P, Ning Z, Navab K, Hough G, Morgan TE, Finch CE, Araujo JA, Fogelman AM, Sioutas C, Hsiai T. Ambient ultrafine particles alter lipid metabolism and hdl anti-oxidant capacity in ldlr-null mice. *J Lipid Res*. 2013;54:1608-1615

66. Araujo JA, Barajas B, Kleinman M, Wang X, Bennett BJ, Gong KW, Navab M, Harkema J, Sioutas C, Lusis AJ, Nel AE. Ambient particulate pollutants in the ultrafine

range promote early atherosclerosis and systemic oxidative stress. *Circ Res*. 2008;102:589-596

67. Pope CA, 3rd, Burnett RT, Thurston GD, Thun MJ, Calle EE, Krewski D, Godleski JJ. Cardiovascular mortality and long-term exposure to particulate air pollution: Epidemiological evidence of general pathophysiological pathways of disease. *Circulation*. 2004;109:71-77

68. Bray SJ. Notch signalling in context. *Nature reviews. Molecular cell biology*. 2016;17:722-735

69. MacKenzie F, Duriez P, Wong F, Noseda M, Karsan A. Notch4 inhibits endothelial apoptosis via rbp-jkappa-dependent and -independent pathways. *The Journal of biological chemistry*. 2004;279:11657-11663

70. Quillard T, Coupel S, Coulon F, Fitau J, Chatelais M, Cuturi MC, Chiffoleau E, Charreau B. Impaired notch4 activity elicits endothelial cell activation and apoptosis: Implication for transplant arteriosclerosis. *Arterioscler Thromb Vasc Biol*. 2008;28:2258-2265

71. Rostama B, Peterson SM, Vary CP, Liaw L. Notch signal integration in the vasculature during remodeling. *Vascular pharmacology*. 2014;63:97-104

72. Walshe TE, Connell P, Cryan L, Ferguson G, Gardiner T, Morrow D, Redmond EM, O'Brien C, Cahill PA. Microvascular retinal endothelial and pericyte cell apoptosis in vitro: Role of hedgehog and notch signaling. *Investigative ophthalmology & visual science*. 2011;52:4472-4483

73. Krebs LT, Xue Y, Norton CR, Shutter JR, Maguire M, Sundberg JP, Gallahan D, Closson V, Kitajewski J, Callahan R, Smith GH, Stark KL, Gridley T. Notch signaling is

essential for vascular morphogenesis in mice. *Genes & development*. 2000;14:1343-1352

74. Baonza A, Garcia-Bellido A. Notch signaling directly controls cell proliferation in the drosophila wing disc. *Proc Natl Acad Sci U S A*. 2000;97:2609-2614

75. Jensen J, Heller RS, Funder-Nielsen T, Pedersen EE, Lindsell C, Weinmaster G, Madsen OD, Serup P. Independent development of pancreatic alpha- and beta-cells from neurogenin3-expressing precursors: A role for the notch pathway in repression of premature differentiation. *Diabetes*. 2000;49:163-176

76. Fre S, Huyghe M, Mourikis P, Robine S, Louvard D, Artavanis-Tsakonas S. Notch signals control the fate of immature progenitor cells in the intestine. *Nature*. 2005;435:964-968

77. Stanger BZ, Datar R, Murtaugh LC, Melton DA. Direct regulation of intestinal fate by notch. *Proc Natl Acad Sci U S A*. 2005;102:12443-12448

78. Pellegrinet L, Rodilla V, Liu Z, Chen S, Koch U, Espinosa L, Kaestner KH, Kopan R, Lewis J, Radtke F. Dll1- and dll4-mediated notch signaling are required for homeostasis of intestinal stem cells. *Gastroenterology*. 2011;140:1230-1240 e1231-1237

79. Hellstrom M, Phng LK, Hofmann JJ, Wallgard E, Coultas L, Lindblom P, Alva J, Nilsson AK, Karlsson L, Gaiano N, Yoon K, Rossant J, Iruela-Arispe ML, Kalen M, Gerhardt H, Betsholtz C. Dll4 signalling through notch1 regulates formation of tip cells during angiogenesis. *Nature*. 2007;445:776-780

80. Lobov IB, Renard RA, Papadopoulos N, Gale NW, Thurston G, Yancopoulos GD, Wiegand SJ. Delta-like ligand 4 (dll4) is induced by vegf as a negative regulator of angiogenic sprouting. *Proc Natl Acad Sci U S A*. 2007;104:3219-3224

81. Artavanis-Tsakonas S, Rand MD, Lake RJ. Notch signaling: Cell fate control and signal integration in development. *Science*. 1999;284:770-776

82. Joutel A, Corpechot C, Ducros A, Vahedi K, Chabriat H, Mouton P, Alamowitch S, Domenga V, Cecillion M, Marechal E, Maciazek J, Vayssiere C, Cruaud C, Cabanis EA, Ruchoux MM, Weissenbach J, Bach JF, Bousser MG, Tournier-Lasserve E. Notch3 mutations in cadasil, a hereditary adult-onset condition causing stroke and dementia. *Nature*. 1996;383:707-710

83. Schulz H, Harder V, Ibald-Mulli A, Khandoga A, Koenig W, Krombach F, Radykewicz R, Stampfl A, Thorand B, Peters A. Cardiovascular effects of fine and ultrafine particles. *J Aerosol Med*. 2005;18:1-22

84. Frampton MW. Systemic and cardiovascular effects of airway injury and inflammation: Ultrafine particle exposure in humans. *Environ Health Persp*. 2001;109:529-532

85. Nemmar A, Hoet PHM, Vanquickenborne B, Dinsdale D, Thomeer M, Hoylaerts MF, Vanbilloen H, Mortelmans L, Nemery B. Passage of inhaled particles into the blood circulation in humans. *Circulation*. 2002;105:411-414

86. Yu B, Zhou S, Wang Y, Qian T, Ding G, Ding F, Gu X. Mir-221 and mir-222 promote schwann cell proliferation and migration by targeting lass2 after sciatic nerve injury. *Journal of cell science*. 2012;125:2675-2683

87. Wu L, Li H, Jia CY, Cheng W, Yu M, Peng M, Zhu Y, Zhao Q, Dong YW, Shao K, Wu A, Wu XZ. Microrna-223 regulates foxo1 expression and cell proliferation. *FEBS letters*. 2012;586:1038-1043

88. Bleck B, Grunig G, Chiu A, Liu M, Gordon T, Kazeros A, Reibman J. Microrna-375 regulation of thymic stromal lymphopoietin by diesel exhaust particles and ambient particulate matter in human bronchial epithelial cells. *J Immunol*. 2013;190:3757-3763

89. Rodosthenous RS, Coull BA, Lu Q, Vokonas PS, Schwartz JD, Baccarelli AA. Ambient particulate matter and micrornas in extracellular vesicles: A pilot study of older individuals. *Part Fibre Toxicol*. 2016;13:13

90. Yang L, Hou XY, Wei Y, Thai P, Chai F. Biomarkers of the health outcomes associated with ambient particulate matter exposure. *Sci Total Environ*. 2017;579:1446-1459

91. Li R, Yang J, Saffari A, Jacobs J, Baek KI, Hough G, Larauche MH, Ma J, Jen N, Moussaoui N, Zhou B, Kang H, Reddy S, Henning SM, Campen MJ, Pisegna J, Li Z, Fogelman AM, Sioutas C, Navab M, Hsiai TK. Ambient ultrafine particle ingestion alters gut microbiota in association with increased atherogenic lipid metabolites. *Sci Rep*. 2017;7:42906

92. Gerhardt H, Golding M, Fruttiger M, Ruhrberg C, Lundkvist A, Abramsson A, Jeltsch M, Mitchell C, Alitalo K, Shima D. Vegf guides angiogenic sprouting utilizing endothelial tip cell filopodia. *The Journal of cell biology*. 2003;161:1163-1177

93. Nguyen D-HT, Stapleton SC, Yang MT, Cha SS, Choi CK, Galie PA, Chen CS. Biomimetic model to reconstitute angiogenic sprouting morphogenesis in vitro. *Proceedings of the National Academy of Sciences*. 2013;110:6712-6717

94. Hogan BM, Bos FL, Bussmann J, Witte M, Chi NC, Duckers HJ, Schulte-Merker S. Ccbe1 is required for embryonic lymphangiogenesis and venous sprouting. *Nature genetics*. 2009;41:396

95. Li YS, Haga JH, Chien S. Molecular basis of the effects of shear stress on vascular endothelial cells. *J Biomech*. 2005;38:1949-1971

96. Ando J, Yamamoto K. Effects of shear stress and stretch on endothelial function. *Antioxid Redox Signal*. 2011;15:1389-1403

97. Li R, Jen N, Wu L, Lee J, Fang K, Quigley K, Lee K, Wang S, Zhou B, Vergnes L, Chen YR, Li Z, Reue K, Ann DK, Hsiai TK. Disturbed flow induces autophagy, but impairs autophagic flux to perturb mitochondrial homeostasis. *Antioxid Redox Signal*. 2015;23:1207-1219

98. Lee J, Packard RR, Hsiai TK. Blood flow modulation of vascular dynamics. *Curr Opin Lipidol*. 2015;26:376-383

99. Cheng C, Tempel D, van Haperen R, de Boer HC, Segers D, Huisman M, van Zonneveld AJ, Leenen PJ, van der Steen A, Serruys PW, de Crom R, Krams R. Shear stress-induced changes in atherosclerotic plaque composition are modulated by chemokines. *J Clin Invest*. 2007;117:616-626

100. Chiu JJ, Wang DL, Chien S, Skalak J, Usami S. Effects of disturbed flow on endothelial cells. *Journal of biomechanical engineering*. 1998;120:2-8

101. Dewey Jr CF, Bussolari SR, Gimbrone Jr MA, Davies PF. The dynamic response of vascular endothelial cells to fluid shear stress. *Journal of biomechanical engineering*. 1981;103:177-185

102. Ding Z, Liu S, Wang X, Khaidakov M, Dai Y, Mehta JL. Oxidant stress in mitochondrial DNA damage, autophagy and inflammation in atherosclerosis. *Scientific reports*. 2013;3:1077

103. Frangos JA, Huang TY, Clark CB. Steady shear and step changes in shear stimulate endothelium via independent mechanisms--superposition of transient and sustained nitric oxide production. *Biochem Biophys Res Commun*. 1996;224:660-665

104. Hwang J, Michael H, Salazar A, Lassegue B, Griendling K, Navab M, Sevanian A, Hsiai TK. Pulsatile versus oscillatory shear stress regulates nadph oxidase subunit expression: Implication for native ldl oxidation. *Circulation research*. 2003;93:1225-1232

105. Hwang J, Saha A, Boo YC, Sorescu GP, McNally JS, Holland SM, Dikalov S, Giddens DP, Griendling KK, Harrison DG, Jo H. Oscillatory shear stress stimulates endothelial production of o2- from p47phox-dependent nad(p)h oxidases, leading to monocyte adhesion. *J Biol Chem*. 2003;278:47291-47298

106. Surapisitchat J, Hoefen RJ, Pi X, Yoshizumi M, Yan C, Berk BC. Fluid shear stress inhibits tnf-alpha activation of jnk but not erk1/2 or p38 in human umbilical vein endothelial cells: Inhibitory crosstalk among mapk family members. *Proceedings of the National Academy of Sciences of the United States of America*. 2001;98:6476-6481

107. Koh W, Sachidanandam K, Stratman AN, Sacharidou A, Mayo AM, Murphy EA, Cheresh DA, Davis GE. Formation of endothelial lumens requires a coordinated pkcepsilon-, src-, pak- and raf-kinase-dependent signaling cascade downstream of cdc42 activation. *Journal of cell science*. 2009;122:1812-1822

108. Rask-Madsen C, King GL. Differential regulation of vegf signaling by pkc-alpha and pkc-epsilon in endothelial cells. *Arterioscler Thromb Vasc Biol*. 2008;28:919-924

109. Dejana E. The role of wnt signaling in physiological and pathological angiogenesis. *Circ Res*. 2010;107:943-952

110. Boselli F, Freund JB, Vermot J. Blood flow mechanics in cardiovascular development. *Cell Mol Life Sci*. 2015;72:2545-2559

111. Roman BL, Pekkan K. Mechanotransduction in embryonic vascular development. *Biomechanics and modeling in mechanobiology*. 2012;11:1149-1168

112. Suarez J, Rubio R. Regulation of glycolytic flux by coronary flow in guinea pig heart. Role of vascular endothelial cell glycocalyx. *The American journal of physiology*. 1991;261:H1994-2000

113. De Bock K, Georgiadou M, Carmeliet P. Role of endothelial cell metabolism in vessel sprouting. *Cell Metab*. 2013;18:634-647

114. De Bock K, Georgiadou M, Schoors S, Kuchnio A, Wong BW, Cantelmo AR, Quaegebeur A, Ghesquiere B, Cauwenberghs S, Eelen G, Phng LK, Betz I, Tembuyser B, Brepoels K, Welti J, Geudens I, Segura I, Cruys B, Bifari F, Decimo I, Blanco R, Wyns S, Vangindertael J, Rocha S, Collins RT, Munck S, Daelemans D, Imamura H, Devlieger R, Rider M, Van Veldhoven PP, Schuit F, Bartrons R, Hofkens J, Fraisl P, Telang S, Deberardinis RJ, Schoonjans L, Vinckier S, Chesney J, Gerhardt H, Dewerchin M, Carmeliet P. Role of pfkfb3-driven glycolysis in vessel sprouting. *Cell*. 2013;154:651-663

115. Doddaballapur A, Michalik KM, Manavski Y, Lucas T, Houtkooper RH, You X, Chen W, Zeiher AM, Potente M, Dimmeler S, Boon RA. Laminar shear stress inhibits endothelial cell metabolism via klf2-mediated repression of pfkfb3. *Arterioscler Thromb Vasc Biol*. 2015;35:137-145

116. Wu D, Huang RT, Hamanaka RB, Krause M, Oh MJ, Kuo CH, Nigdelioglu R, Meliton AY, Witt L, Dai G, Civelek M, Prabhakar NR, Fang Y, Mutlu GM. Hif-1alpha is required for disturbed flow-induced metabolic reprogramming in human and porcine vascular endothelium. *Elife*. 2017;6

117. Galloway JL, Wingert RA, Thisse C, Thisse B, Zon LI. Loss of gata1 but not gata2 converts erythropoiesis to myelopoiesis in zebrafish embryos. *Dev Cell*. 2005;8:109-116

118. Kulkeaw K, Sugiyama D. Zebrafish erythropoiesis and the utility of fish as models of anemia. *Stem cell research & therapy*. 2012;3:55

119. Chu C-Y, Cheng C-H, Chen G-D, Chen Y-C, Hung C-C, Huang K-Y, Huang C-J. The zebrafish erythropoietin: Functional identification and biochemical characterization. *FEBS letters*. 2007;581:4265-4271

120. Simmons RD, Kumar S, Jo H. The role of endothelial mechanosensitive genes in atherosclerosis and omics approaches. *Arch Biochem Biophys*. 2016;591:111-131

121. Lawrence S, Giles CL, Tsoi AC, Back AD. Face recognition: A convolutional neural-network approach. *IEEE Trans Neural Netw*. 1997;8:98-113

122. Shelhamer E, Long J, Darrell T. Fully convolutional networks for semantic segmentation. *IEEE Trans Pattern Anal Mach Intell*. 2017;39:640-651

123. Zheng S, Jayasumana S, Romera-Paredes B, Vineet V, Su Z, Du D, Huang C, Torr PH. Conditional random fields as recurrent neural networks. *Proceedings of the IEEE International Conference on Computer Vision*. 2015:1529-1537

124. Peng H, Ruan Z, Long F, Simpson JH, Myers EW. V3d enables real-time 3d visualization and quantitative analysis of large-scale biological image data sets. *Nat Biotechnol*. 2010;28:348-353

125. Eliceiri KW, Berthold MR, Goldberg IG, Ibanez L, Manjunath BS, Martone ME, Murphy RF, Peng H, Plant AL, Roysam B, Stuurman N, Swedlow JR, Tomancak P, Carpenter AE. Biological imaging software tools. *Nat Methods*. 2012;9:697-710

126. Peng H, Tang J, Xiao H, Bria A, Zhou J, Butler V, Zhou Z, Gonzalez-Bellido PT, Oh SW, Chen J, Mitra A, Tsien RW, Zeng H, Ascoli GA, Iannello G, Hawrylycz M, Myers E, Long F. Virtual finger boosts three-dimensional imaging and microsurgery as well as terabyte volume image visualization and analysis. *Nat Commun*. 2014;5:4342

CHAPTER III

Three-dimensional Imaging Coupled with Topological Quantification Uncovers Retinal Vascular Plexuses Undergoing Obliteration

Chang, C.C*., Chu, A*., Meyer, S., Ding, Y., Sun, M.M., Abiri, P., Baek, K.I., Gudapati, V., Ding, X., Guihard, P., Bostrom, K.I, Li, S., Gordon, L.K., Zheng, J.J., and Hsiai T.K

* Equal contribution.

This chapter is reproduced from the original article published in **Theranostics**. 2021;11(3):1162 and approved by the co-authors.

Introduction

Aberrant retinal angiogenesis is a hallmark of numerous retinal disorder-mediated vasculopathies, including retinopathy of prematurity (ROP) and diabetic retinopathy (DR), resulting in visual impairment [1, 2]. Premature newborns are susceptible to hyperoxic injury and the development of retinopathy of prematurity. They often require supplemental oxygen therapy due to the immature development of their lungs, and this hyperoxia exposure leads to attenuation of the retinal vascular bed [3-5]. Subsequently, these newborns further develop ischemia-induced neovascularization in the retina due to local hypoxia and increased metabolic demand [4, 6]. Similarly, diabetic patients are also prone to developing proliferative retinopathy and aberrant neovascularization as a result of hypoxia [7, 8].

To quantify the microvascular damage that occurs early in DR, ophthalmologists have relied on several clinical imaging modalities, including fundus photography, fluorescein angiography (FA), and optical coherence tomography angiography (OCTA). These imaging modalities allow for screening and monitoring of vision-threatening complications in adults [9, 10]. OCT-angiography enables identification of preclinical retinal vascular changes, including the remodeling of the foveal avascular zone (FAZ), capillary nonperfusion, and reduction of capillary density [11-15]. However, the quality of the images obtained using these modalities in neonates and young children is often limited by ocular movement and a restricted field of view.

To elucidate the mechanisms underlying vascular abnormalities seen in the presence of ROP, researchers have utilized mouse models of oxygen-induced retinopathy (OIR) [16, 17]. Akin to early ocular development in humans, the postnatal mouse retina is considered a viable model to underpin the development of retinal vascular network [1, 2, 16]. The current gold standard to image and quantify changes in the murine retinal vascular network typically utilizes whole-mount samples with 2-D analysis [17-21]. Previous groups have utilized 3-D imaging to demonstrate vaso-obliteration in the rat model [22] and report the local ‘knotted’ morphology and vascular tufts during neovascularization in murine OIR [23]. To quantify the early abnormalities and progression of OIR in 3-D for the entire retinal vasculature, we hereby coupled selective plane illumination microscopy also known as light-sheet fluorescence microscopy (LSFM), with quantitative 3-D topological analyses to interrogate the entire retinal vasculature in response to hyperoxia-induced microvascular obliteration [24-28]. Unlike confocal or two-photon microscopy commonly applying a point scanning approach, LSFM generates a sheet of laser light to rapidly scan across optically-cleared specimens [24, 29]. This approach provides an entry point to investigate the murine ocular system in 3-D with rapid imaging acquisition to minimize photo-bleaching. LSFM further provides the high axial resolution needed to quantify the multi-layered vascular network; namely, the vertical sprouts embedded between the primary and secondary plexuses [1, 16, 30].

To this end, we optimized an optical clearing technique to preserve the 3-D conformation of the hemispherical murine retina and its microvasculature for LSFM imaging. Following hyperoxia exposure (75% O_2) to post-natal mice for 5 days (P7-P12), we quantified the spatial variations in vascular obliteration and observed a preferential loss of the vertical sprouts and secondary plexuses at day P12. Using principal component analysis (PCA), we developed an automated segmentation algorithm to demonstrate a significant reduction in the volume fraction of the vertical sprouts that bridge the primary and secondary plexuses. In oxygen-induced retinopathy (OIR), we calculated both Euler numbers and clustering coefficients to reveal a reduction in the global vascular connectivity, but a preserved local connectivity. Our topological analysis of the large data set provided by light-sheet imaging, including PCA, further corroborated the deep capillary obliteration following oxygen-mediated retinopathy. We hereby establish topological quantification to unravel spatial variations in microvascular obliteration that preferentially affect the secondary plexus and vertical sprouts in murine OIR, allowing for the detection of early changes in hyperoxia-mediated microvascular disarray.

Results

Schematic pipeline for the 3-D quantitative analysis of murine retinal vasculature

To achieve 3-D retinal microvasculature imaging and analysis (Figure 1A-B), we developed an eight-step pipeline for light-sheet imaging and quantification in the ensuing sections (Figure 1C). After euthanizing the mice at postnatal day 12 (P12), the ocular globes were enucleated and dissected to obtain the unscathed hemispherical retinas, and polymerization and lipid removal were performed in the monomer and clearing solution to achieve optical transparency (Figure 1D). Next, immunofluorescence staining with Isolectin B4 (Vector Lab, CA) was performed to label the vascular endothelium in preparation for light-sheet imaging. Following filament tracing, the morphology and topology of the retinal vasculature were characterized by quantifying the vascular branching points, Euler characteristics, and clustering coefficients.

3-D characterization of the vascular network under normoxic conditions

LSFM was employed to unravel the 3-D vascular network in the hemispherical retina with endothelial cells labeled with Alexa Fluor 488 (Figure 2A-B). Representative volumes of interest (VOIs) were selected, including a 2-D section (red dashed line), peripheral vascular networks in the peripheral region (orange box), the middle region (blue box) (Figure 2B), and a 2-D slice (Figure 2C), to highlight the two-layered plexuses with 2-D connections. The volumetric rendering of the VOI (blue box) revealed the vertical sprouts bridging the primary and secondary plexuses in 3-D (Figure 2D, Movie S1). Light-sheet imaging also allowed for visualization of the 3-D vascular network from selected VOIs at various depths (Figure 2E-F), uncovering the interconnected capillary vascular bed as indicated by the color-coded depth imaging (Figure 2G-H). Taken together, the 3-D LSFM revealed the hemispherical vascular network to uncover the multi-layered capillary plexuses under normoxic conditions.

Morphological and topological quantification of the 3-D retinal vascular network

We applied the filament tracing strategy to characterize retinal morphology and topology. Vascular connectivity and clustering coefficients were quantified (Figure 3A, Movie S2), as illustrated by the interconnected nodes (in green) within the 3-D vascular network (in red). Clustering coefficients represent the degree of regional vascular connectivity, ranging from 0 to 1. The connectivity and mean clustering coefficients for the unscathed retina were 1.6×10^{4} and 2.9×10^{-2}, respectively. The former coefficient indicates a large number of loops in the retinal vasculature, and the latter shows the low degree of clustering of these individual nodes. We interrogated the central (yellow disk), middle (orange rings), and peripheral (blue rings) regions of the hemispherical network (Figure

3A). We selected 5 volumes of interest (VOIs) from each of the regions as a standard assessment for retinopathy [10]. The 3-D vascular network was visualized (Figure 3B, D, and F) and filament tracing was applied to characterize the vessel lengths, branching points, and connections in the central, middle and peripheral regions. Nodes were labeled in blue and segments in green (Figure 3C, E, and G). The means of the entire vessel lengths were $6.62 \text{x} 10^3 \pm 7.4 \text{x} 10^2$ µm for the central, $7.29 \text{ x} 10^3 \pm 8.9 \text{x} 10^2$ µm for the middle, and $8.26 \text{ x} 10^2 \pm 1.9 \text{x} 10^3$ µm for the peripheral regions. In the absence of hyperoxia exposure, the differences among these 3 regions were statistically insignificant ($p > 0.05$, n = 5/region). The means of the entire vessel volumes were $9.19 \text{ x } 10^5 \pm 1.63 \text{x} 10^5$ µm^3, $9.81 \text{ x } 10^5 \pm 1.59 \text{x} 10^5$ µm^3, and $9.27 \text{ x } 10^5 \pm 2.5 \text{x} 10^5$ µm^3, respectively. There were 146 ± 23.1 nodes and 32.3 ± 9.3 in connectivity in the central region, 157.3 ± 41.3 nodes and 35 ± 9.85 in connectivity in the middle region, and 172.3 ± 49.1 nodes and 43.3 ± 16.1 in connectivity in the peripheral region (Figure 3H-K). Thus, the differences in vascular lengths, volumes, connections, and branching points among the three representative regions of the retinal vasculature were statistically insignificant under the normoxic conditions.

Changes in the morphological and topological measures in OIR

In response to hyperoxia, the 3-D vascular network (Figure 4A-B, Movies S3-4) and filament tracing results (Figure 4C, Movie S5) in the OIR group were markedly different from the normoxia group (Figure 4). A preferential depletion of the capillaries in the primary plexuses developed in the central region, whereas depletion of vertical sprouts and secondary plexuses occurred in all three regions as evidenced by the selected VOIs (Figure 4D-E). Importantly, the immunofluorescence 2-D flat mount images for both normoxia and OIR groups demonstrated the expected phenotype of central vaso-obliteration only for the primary plexus, but could not distinguish vertical sprouts and secondary plexus changes unlike the LSFM images (Figure 4F). We further compared the topological parameters, including total length (normoxia: $1.2\times10^6 \pm 3.1\times10^4$; OIR: $2.6\times10^5 \pm 1.3\times10^4$ µm, $p < 0.001$, n = 5/group), total volume (normoxia: $7.3\times10^7 \pm 1.4\times10^7$; OIR: $3.2\times10^7 \pm 8.2\times10^6$ µm^3, $p < 0.05$, n = 5/group), branching points (normoxia: $2.7\times10^4 \pm 9.6\times10^2$; OIR: $5.8\times10^3 \pm 1.3\times10^3$, $p < 0.001$, n = 5/group) and connectivity (normoxia: $1.1\times10^4 \pm 6.9\times10^2$; OIR: $2.3\times10^3 \pm 9.1\times10^2$, $p < 0.01$, n = 5/group) for the conformationally-intact retinal vascular network (Figure 4G). In summary, our topological analysis allowed for the demonstration and quantification of the preferential obliteration of the outer layer (secondary plexuses) and vertical sprouts of the capillary vasculature under hyperoxic conditions.

Frequency of clustering coefficients to quantify differences in the local vs. global vascular network

We computed the distribution of the clustering coefficients for each node in the vascular network (Figure 5A). In both normoxia- and hyperoxia-exposed P12 mice, approximately 10% of the nodes exhibited positive clustering coefficients, whereas 90% of the nodes approached zero (grey), suggesting an overall paucity of connections with the neighboring nodes in the retinal vasculature. The most common clustering coefficients were 0 and the most frequent number of degrees was 3 (Figure 5B-C). These findings demonstrate that most of the nodes form connections with three neighboring nodes, with no connections between its neighbors, resulting in a 3-D reticulated vascular network, analogous to a honeycomb. In addition, the reticulated pattern in the local network was preserved despite hyperoxia-induced obliteration of the capillaries. We further compared the average clustering coefficients among the central, middle, and peripheral regions of the retina (Figure 6A-B), revealing statistically insignificant differences between normoxia and hyperoxia conditions (central = 0.026 ± 0.012 vs. 0.047 ± 0.032, $p > 0.05$; middle = 0.027 ± 0.018 vs. 0.039 ± 0.013, $p > 0.05$; peripheral = 0.044 ± 0.019 vs. 0.038 ± 0.018, $p > 0.05$, n = 5/group). This comparison demonstrated that the local connectivity was preserved, whereas the global connectivity was significantly reduced (local = 0.032 ± 0.018 vs. 0.043 ± 0.024, $p > 0.05$, n = 5/group; global = $1.1\times10^4 \pm 6.9\times10^2$ vs. $2.3\times10^3 \pm 9.1\times10^2$, $p < 0.05$, n = 5/group) (Figure 4 and 6). Thus, determination of clustering coefficients supports the preserved local patterning in OIR, but the impaired global capillary connections in response to hyperoxia.

Topological quantification of the plexuses and vertical sprouts following hyperoxia

The filament tracing results allowed for auto-segmentation of image stacks to construct a 3-D unscathed retinal vascular network. We randomly selected 5 VOIs at 200 µm in thickness to quantify the volume fraction of vertical sprouts, defined as the volume of vertical sprouts divided by the total volume of the vascular network. The representative images for the maximum intensity projection (MIP) of the automatically segmented plexuses and vertical sprouts were assessed from selected image slices (Figure S1). Furthermore, the 3-D rendering results (Figure 7A-B) of the plexuses (in yellow) and vertical sprouts (in blue) demonstrated statistically significant obliteration of the vertical sprouts following hyperoxia treatment ($p<0.05$ vs. normoxia, n=5) (Figure 7A & B). Spatial variations in obliteration were observed; namely, 17.98% ± 5.2% vs. 0.69% ± 0.75% in the middle, and 18.89% ± 7.43% vs. 0.51% ± 0.62% in the peripheral regions (Figure 7C-D). To validate the auto segmentation method, we segmented the vertical sprouts and plexuses by performing manual and automated labeling. The generalized dice coefficients were obtained to compare the similarity between the manual annotation and automated segmentation under each condition. To optimize automated segmentation, we introduced the sliding window (40 µm x 40 µm x 40 µm) with 20 µm in shifting distance and 35° as the cutoff angle (Figure 7E, Tables S1-S3). The maximum dice coefficient and low standard deviation (0.852 ±0.04) indicate accurate segmentation of the vertical sprouts by the auto-segmentation method (Figure 7E, Tables S1-S3). Finally, the representative VOI demonstrated 3-D rendering of the color-coded (X: Blue, Y: Green: Z: Red) vascular networks in relation to the orientation of the vessels (Figure 7F). Taken together, our computational analyses enable multi-scale interrogation of the 3-D vascular network from the micro- to the macro scale.

DISCUSSION

Advances in imaging modalities have dramatically enhanced the fundamental understanding and experimental capabilities of microvascular injury and repair models, including retinopathy of prematurity and diabetes. Our integration of 3-D imaging with topological computation demonstrated the ability to quantitatively characterize the morphological changes in 3-D of the entire retinal vascular network in a neonatal mouse model of oxygen-induced retinopathy (OIR). The use of clustering coefficients, Euler's number, and PCA corroborated the reticular vascular network undergoing capillary obliteration, revealing spatial variations in capillary obliteration in the deep plexuses and the bridging vessels in response to hyperoxia. Our light-sheet imaging further revealed a 3-D drop-out phenomenon of the deep plexuses preceding capillary obliteration in the central superficial plexuses, otherwise challenging to detect with the 2-D imaging modalities [16, 31].

In the retina, vascular development is regulated by a host of signaling pathways that are coordinated by environmental cues and cellular metabolic activities [2, 3]. Murine retinal vasculature provides a viable platform to investigate genetic and epigenetic effects on vascular injury and regeneration [1, 2, 16]. Disturbances to the signaling pathways, including changes in oxygen and nutrient provision, promote pathological vaso-obliteration, result in structural and functional abnormalities during angiogenesis [1, 6, 16]. In diabetic retinopathy, hypoxia resulting from a non-perfused capillary bed induces vascular endothelial growth factor (VEGF) expression, thereby, promoting neo-angiogenesis and vascular permeability [7]. In retinopathy of prematurity, pathological obliteration of the capillary network can progress to irreversible blindness [3, 6]. To this end, 3-D laser light-sheet microscopy allows for imaging of the 3-D hemispherical vascular network, uncovering multi-layer vascular changes, and quantifying epigenetic vs. genetic perturbations. LSFM coupled with our topologic analyses could also be adapted to larger animals and even human tissue samples, with translational potential to identify therapeutic targets [16, 24, 32, 33].

The conventional method used to image retinal vascular structures typically involves flat-mount samples, with the fluorescently-labeled structures detected via confocal or fluorescence microscopy [17, 18, 34-40]. Unlike wide-field, two-photon and confocal microscopes, LSFM enables rapid optical sectioning at high acquisition rates [25, 26]. Optical sectioning generates a sheet of light, allowing for only a selective plane to be illuminated; thereby, minimizing photobleaching [24]. LSFM imaging enables rapid image acquisition of the 3-D mouse retina in ~10 mins for high-throughput studies.

Advances in optical clearing techniques have rendered the tissue or organ systems (including retinas) from different animal models transparent for LSFM imaging [22, 23, 25, 26, 33, 41]. These techniques remove lipids from tissues to minimize photon scattering while stabilizing the 3-D structural conformation [42-44] to allow for deep tissue penetration for large samples [42, 45-48]. Successful 3-D imaging of murine hyperoxia-induced retinopathy often encounters technical challenges with the fragile developing tissues and small specimen size. Previously, Singh et al. demonstrated vaso-obliteration in the rat model [22]. Prahst et al. reported the local ‘knotted’ morphology and vascular tufts seen during neovascularization [23]. In our study, we optimized and coupled light-sheet imaging with detailed topological analyses to interrogate the entire retinal vasculature, focusing on the vaso-obliterative phase in the mouse OIR model. We demonstrated the spatial variations in 3-D microvascular obliteration, namely, the loss of primary (inner) vs. secondary (outer) capillary plexuses in response to oxygen-induced retinopathy (OIR). This integration of light-sheet imaging and topological analyses demonstrated that vaso-obliteration preferentially occurs in the outer layer (secondary plexus) and the vertical sprouts.

In addition to imaging developmental biologic processes and tissue regeneration, other laboratories and our group have demonstrated the capacity of LSFM to investigate ophthalmologic disease in small animal models [22, 23]. While adaptive optics scanning laser ophthalmoscopy (AOSLO) performs *in vivo* imaging with high spatial and temporal resolution [49-52], the small field of view (FOV) remains a challenge to capture the entire vascular network. Similarly, optical coherence tomography (OCT) performs *in vivo* imaging of the retinal vasculature with a relatively small FOV [53, 54]. Also, motion artifacts from patient movement and eye blinking further hamper 3-D vascular imaging [55]. In the case of small animal models, confocal microscopy and two-photon microscopy may provide high spatial resolution or deep penetration into the retina; however, the point scan nature of these two imaging modalities usually requires a prolonged period to image the entire retina (> several hours) as opposed to the rapid scanning time (~10 mins) of LSFM [22, 23]. In this context, the integration of 3-D imaging with quantitative topological analysis provides the vascular network phenotype for the entire retina to address the limitations of OCT encountered in imaging small animal models.

In the mouse model of oxygen-induced retinopathy, LSFM imaging, followed by topological analyses, quantifies the 3-D morphological and topological parameters for the entire vascular network. In addition to quantifying vessel lengths, vessel volumes, and branching points, topological computation further quantified the global vs. local vascular connectivity by Euler numbers and clustering coefficients. Unlike conventional estimations of the network connections via branching points, Euler number calculations simultaneously reflect both connectivity and the topological features of a 3-D network [56-58], facilitating comprehensive measurement of the connectivity of a capillary network [18, 59-62]. Moreover, the clustering coefficients capture the local connectivity and degree of organization of the regional vascular network for every vertex in the vascular or neuronal network [63-65]. Using Euler number and clustering coefficient calculations, we demonstrated that in hyperoxia-induced retinopathy, there was a significant reduction in global connectivity, but the local reticular pattern was preserved. We further applied principal component analysis (PCA) to automatically segment the vertical sprouts, and to quantify the volume fraction in the plexuses and vertical sprouts under normoxia vs.

hyperoxia conditions. As a result, we were able to corroborate the differential obliteration of the vertical sprouts and the secondary plexus in OIR. Although this PCA-based segmentation method offered the fidelity to segment the vertical sprouts, it is limited in its use when the sliding windows include multiple vessels in different directions (i.e. bifurcations). While smaller window sizes reduce the probability of including bifurcations, the trade-off is to increase the possibility of miscalculation of vessel orientation. Thus, determining and optimizing the window size is essential to include adequate vessel elements for quantification of vessel orientation and minimization of including vessel bifurcations prior to initiating the analysis. A potential improvement may be achieved by combining PCA-based segmentation with machine learning by applying the image labels of vertical sprouts (determined by using different window sizes) as inputs to train the classifiers for segmentation. Despite the well-defined formulas to calculate Euler numbers and clustering coefficients, uncertainties reside in the accuracy of segmentation of the blood vessels using filament tracing. The use of machine learning-based automated segmentation for blood vessels will further strengthen the capacity to abbreviate the segmentation process and to obviate the need for filament tracing. Taken together, the topological computation analyses quantitatively corroborate the spatial variations of vaso-obliteration, identifying impaired vascular branching and global connectivity, and reduced vessel volumes and lengths in OIR retinas.

In sum, 3-D LSFM enables deep tissue penetration to unravel topological changes in the 3-D retinal vasculature. Integration of LSFM with 3-D topological analysis demonstrates global vaso-obliteration, but preserved local 3-D reticular vascular architecture, supporting the differential vascular obliteration from the outer (secondary) plexuses to the vertical sprouts in hyperoxia-induced retinopathy. Overall, the application of clustering coefficients, Euler’s number, and PCA to 3-D LSFM images provides vascular insights into OIR, with translational significance for developing therapeutic interventions to prevent visual impairment.

Material and Methods

Ethics statement

All animal studies were performed in compliance with the IACUC protocol approved by the UCLA Office of Animal Research and in accordance with the guidelines set by the National Institutes of Health. Humane care and use of animals were observed to minimize distress and discomfort.

The modified passive CLARITY for retinal imaging

We optimized the use of CLARITY for fixed retinas as previously described [44, 47]. The mice were euthanized at P12 for dissection of the ocular globe. We enucleated the intact ocular globe and then fixed globes in 4% paraformaldehyde (PFA) for 1.5 hours. We then removed the cornea, sclera, lens, and choroid while preserving the retina in its 3-D hemispherical configuration. The 3-D retinas were then immersed in 4% paraformaldehyde overnight (Figure 1D-①), followed by overnight incubation in a monomer solution (4% Acrylamide, 0.05% Bis-Acrylamide , and 0.25% VA-044 initiator (weight/volume) in PBS) (Figure 1D-②). Next, samples were placed into a 37 °C water bath for 6 h for hydrogel polymerization (Figure 1D-③). A degassing nitrogen flush or addition of an oil layer was performed to minimize exposure to oxygen. Next, retinas were incubated in the clearing solution (4% weight/volume sodium dodecyl sulfate (SDS) and

1.25% weight/volume boric acid (pH 8.5) at 37 °C to remove non-transparent lipid contents. (Figure 1D-4). The retina was rinsed for an additional 24 h in 1X PBS to remove residual SDS, followed by incubation in the refraction index matching solution RIMS (40 g histodenz in 30 ml of 0.02 M PBS with 0.01% neutralized sodium azide (pH to 7.5 with NaOH)) to achieve transparency of the tissue. This method enables the preservation of the 3-D structure of the tissue and maintains the integrity of the retinal vasculature during clearing. Selected P12 retinas (n=3) were collected for direct immunostaining without optical clearing (non-cleared group) for comparison (Figure S2).

Murine oxygen-induced retinopathy (OIR) model

C57BL/6J mice were acquired from the UCLA Division of Laboratory and Animal Medicine colony. All mice were housed in 12:12 h light-dark cycles. Female pregnant mice were fed *ad libitum* with standard rodent chow diet (Pico Lab Rodent Diet 20, cat#5053, Lab Diet, St. Louis, MO) and water during pregnancy and lactation. Oxygen-induced retinopathy (OIR) was produced using standard published guidelines[17]. Pups were designated as P0.5 on the morning that they were delivered. Per protocol recommendations, litters were culled to eight pups. Mothers were randomly assigned to normoxia or hyperoxia (OIR) conditions. To induce OIR, the newborn mice were exposed to 75% oxygen continuously in an airtight chamber (Biospherix Proox model 360, Parish, NY, USA) with their nursing mothers from P7 to P12 before removal to room air, whereas the normoxia group remained in room air (21% oxygen) throughout the postnatal period.

Immunostaining and imaging of flat-mount retinas

Immunostaining and imaging were performed as previously described [66]. Briefly, dissected retinas were washed with phosphate-buffered saline (PBS), blocked with blocking buffer (20% fetal bovine serum (FBS), 2% goat serum, 0.05% bovine serum albumin (BSA), and 1%Triton X-100 in PBS) for 1 h, and stained with Alexa594-isolectin GS-IB4 (Invitrogen, Carlsbad, CA, USA) at 4 °C overnight. Retinas were then incised into four equally-sized quadrants and mounted with ProLong mounting medium (Invitrogen). Images were taken at 4X magnification using an AxioCam CCD digital camera (Carl Zeiss) mounted to an inverted epifluorescence microscope (AxioVert 135; Carl Zeiss).

Immunostaining for unscathed retinal vasculature

The optically transparent retinas were placed into a blocking buffer Perm/Block (1X PBS + 0.3% Triton-X + 0.2% bovine serum albumin + 5% fetal bovine serum) solution for 1 h at room temperature with gentle shaking. Primary biotinylated GS isolectin B4 (1:50, Vector lab, CA) was used to stain retinal vasculature. Following 2 days of incubation at 4 °C, retinas were washed with PBSTX (1X PBS + 0.3% Triton-X). Streptavidin conjugated with Alexa-488 (1:100, Invitrogen, CA) was utilized to amplify primary-specific fluorescence. The retinas were washed with PBSTX (1X PBS + 0.3% Triton-X) following each step.

LSFM to image the 3-D retinal vascular network

Our custom-built LSFM was adapted for imaging the 3-D retinal microvasculature as previously reported [24, 25, 67]. The detection arm is composed of a stereomicroscope (MVX10, Olympus, Japan) with a 1X magnification objective (NA = 0.25), a scientific

CMOS (sCMOS, ORCA-Flash4.0 LT, Hamamatsu, Japan), and a series of filters (Exciter: FF01-390/482/532/640; Emitter: FF01-446/510/581/703; Dichroic: Di01-R405/488/532/635, Semrock, New York, USA). The illumination arm, orthogonal to the detection arm, is composed of the continuous wave laser at 473 nm and 532 nm (LMM-GBV1-PF3-00300-05, Laserglow Technologies, Canada) (Figure S3A). The illumination beam was then reshaped by a relay lens composed of two achromatic doublets with f1= 100 mm and f2 = 30 mm, respectively, followed by the objectives (Nikon, 10X/0.3 Plan Fluor) as the illumination Lens. The lateral and axial resolutions are 5.6 µm and 6.6 µm, respectively with the 4X zoom lens (Figure S3B). The confocal parameter was the effective illumination region (dotted orange line in Figure S3B). For image acquisition, the samples were immersed in the refractive index matching solution (RIMS: RI of 1.46–1.48) with a 1% agarose solution in a Borosilicate glass tube (RI = 1.47, Pyrex 7740, Corning, New York, USA) to reduce refraction and reflection from various interfaces. The glass sample holder was placed in a 3-D-printed opening chamber, made of acrylonitrile butadiene styrene (ABS) (uPrint, Stratasys, USA) and it was filled with 99.5% glycerol (RI = 1.47). We applied single illumination to image the retinal samples within the confocal region. The multiple scans (~3 scans and ~3 mins per each scan) and image stitching module in ImageJ [68] (Tile overlap = 15% and regression threshold = 0.9) were applied to acquire the 3-D imaging stacks for the entire retinas.

Computational analyses of the morphological and topological parameters of the vascular network

The raw data were preprocessed in ImageJ to remove stationary noise [69, 70] and the background was reduced by rolling ball background subtraction (20 pixels in radius). To provide the axial visualization or the depth of the 3-D vascular network, we applied the depth-coded plugin in ImageJ to enhance visualization of the superficial and deep capillaries. In addition, 3-D rendering and semi-automated filament tracing were performed and processed in Amira 6.1. The results of filament tracing were used to quantify both the morphological (Euler-Poincaré characteristic) and topological parameters (clustering coefficients). The Euler number, χ, of the 3-D object was defined as follows [56, 58]:

$$\chi = n_0 - n_1 + n_2 - n_3, \quad (1)$$

where n_0, n_1, n_2, and n_3 are the numbers of vertices (V), edges (E), faces (F), and the individual voxels contained in a 3-D object, respectively. In the setting of increasing connected edges, the Euler number decreases while the network becomes well-connected. We provided an analysis of the changes in Euler number in response to the morphological changes in Figure S4A. The Euler number remains the same when the new connections form a branching structure (first row of Figure S4A). In addition, the Euler number is reduced when a new connection forms loops in a reticular-like structure (second row in Figure S4A), whereas the Euler number is increased when the new connection forms disconnected objects (third row in Figure S4A). Thus, two factors are the main contributors to the Euler number: 1) the number of loops (holes), and 2) the numbers of disconnected objects [16]. In this context, we defined the connectivity for the vascular network as [59]:

$$\text{Connectivity}=1-\chi, \quad (2)$$

In comparison to the Euler number, the clustering coefficient (C) reflects the local connectivity of individual vertices or nodes in the vasculature [63-65, 71]. The clustering coefficient of each vertex and the average clustering coefficient C are defined as follows, respectively:

$$C_i = \frac{number\ of\ pairs\ of\ neighbors\ connected\ by\ edges}{number\ of\ pairs\ of\ neighbors}$$

$$C = \frac{1}{N}\sum C_i \quad \text{i=1,2,…N,} \tag{3}$$

The local clustering coefficient C_i for a vertex v_i is given by the proportion of links between the vertices within its neighborhood divided by all possible connections between its neighbors (Figure S4B). For detailed mathematical calculation, a graph G (Equation 4) consists of a set of edges, ***E,*** and vertices, ***V,*** and an edge, e_{ij}, connecting vertex v_i with vertex v_j (Figure S4B). We define the neighborhood set N_i of vertex v_i for its directly connected neighbors (Equation 5). By defining $k_i=|\boldsymbol{N}_i|$ as the number of neighbors in set $\boldsymbol{N}_i$ for a vertex v_i, the clustering coefficient C_i for vertex v_i can be calculated (Equation 6).

$$G= (\boldsymbol{V}, \boldsymbol{E}), \tag{4}$$

$$N_i = \{v_j : e_{ij} \in E \ \vee \ e_{ji} \in E\}, \tag{5}$$

$$C_i = \frac{2\times|\{e_{jk}: v_j, v_k \in N_i, e_{jk} \in E\}|}{k_i(k_i-1)} \tag{6}$$

Quantitative analysis of vascular plexuses and vertical sprouts in retinal vasculature

The segmented 3D image stacks were derived from the filament tracing results for the retinal vasculature, and they were resampled along the axis passing through and perpendicular to the optical disk. To quantify the volume of vertical sprouts, we developed an automated segmentation method based on principal component analysis

(PCA) to reduce the dimensionality for the large data set. Considering a thin section from the retinal vasculature image stack with the origin at the center of mass, the vessels belonging to the primary and secondary plexuses are mainly in azimuthal or polar directions, whereas the majority of the vertical sprouts develop in a radial direction (Figure S1A). To quantify the vessel direction for 3-D image stacks, we introduced a sliding window to sample the principal component representing the vessel orientation inside the window (Figure S1A). The coordinates of each segmented blood vessel inside the sliding window were extracted and recorded for deriving the representative principal component for each window (Figure S1A). Next, we applied the center of the mass as the origin to calculate the angle (θ) between the principal vector of the voxel and the vector from the origin to the center of the voxel (Figure S1A). For validation of the quantification, we utilized the generalized dice coefficient (GDC). It is the general form of the dice similarity coefficient (DSC) which has been widely used to evaluate the accuracy of automated segmentation methods by measuring the similarity of two labels [72, 73]. The dice similarity coefficients range from 0 to 1 (DSC>0.7 indicates excellent agreement) and take into consideration the true positive (TP), false positive (FP), and false negative (FN) rates simultaneously [72, 73]. The dice similarity coefficient is defined as follows [72]:

$$DSC(X,Y) = 2 \times \frac{X \cap Y}{X+Y} = \frac{2TP}{2TP+FP+FN} \quad , \tag{7}$$

where X represents the manual labeling (ground truth) and Y represents the automated segmentation results. For multiple class segmentation (i.e. vertical sprouts, plexus), the generalized dice coefficient (GDC) is defined as follows [73, 74]:

$$GDC = 2 \times \frac{\sum_{c=1}^{i} \omega_c \sum_{n=1}^{N} X_{cn} Y_{cn}}{\sum_{c=1}^{i} \omega_c \sum_{n=1}^{N} X_{cn} + Y_{cn}} \quad , \qquad \omega_c = \frac{1}{\sum_{n=1}^{N} X_{cn}} \tag{8}$$

where N is the number of the image elements, i is the number of classes, and ω is the weighting coefficient. The generalized dice coefficient was calculated for different window sizes and cutoff angles (Figure 7E, Tables S1-S3), and while the vast majority of combinations demonstrated excellent fidelity, with GDCs >0.7, we selected the best combination (GDC of 0.852) to optimize our auto segmentation results.

Statistical analysis

All data are presented as means ± SD. Statistical significance was determined with unpaired two-tailed Student’s t-test for comparison of two groups and one-way ANOVA with Tukey post hoc analysis for multiple group comparisons. The level of significance was set at $p < 0.05$.

Abbreviations

ABS: acrylonitrile butadiene styrene; AOSLO: adaptive optics scanning laser ophthalmoscopy; BSA: bovine serum albumin; C: clustering coefficient; DR: diabetic retinopathy; DSC: dice similarity coefficient; E: edges; F: faces; FA: fluorescein angiography; FAZ: foveal avascular zone; FBS: fetal bovine serum; FN: false negative; FOV: field of view; FP: false positive; GDC: generalized dice coefficient; LSFM: light-sheet fluorescence microscopy; MIP: maximum intensity projection; OIR: oxygen-induced retinopathy; OCT: optical coherence tomography; OCTA: optical coherence tomography angiography; PBS: phosphate-buffered saline; PCA: principal component analysis; PFA: paraformaldehyde; P#: postnatal day #; RIMS: refraction index matching solution; ROP: retinopathy of prematurity; SDS: sodium dodecyl sulfate; TP: true positive; V: vertices; VEGF: vascular endothelial growth factor; VOI: volumes of interest;

Acknowledgment

The present work was funded by NIH grants National Institutes of Health R01HL083015 (TKH), R01HL111437 (TKH), R01HL129727 (TKH), R01HL118650 (TKH), VA MERIT AWARD I01 BX004356 (TKH), K99 HL148493 (YD), and AHA 18CDA34110338 (YD).

Supplementary Notes

Supplementary movie 1. The 3-D rendering of the vascular network to demonstrate the vertical sprouts embedded between the primary and secondary plexus.

Supplementary movie 2. The filament tracing result of the intact retinal vascular network in normoxia conditions.

Supplementary movie 3. 3-D rendering of the intact retinal vascular network in normoxia conditions.

Supplementary movie 4. 3-D rendering of the abnormal retinal vascular network in OIR.

Supplementary movie 5. The filament tracing of the intact retinal vascular network in OIR.

Representative results for the integration of LSFM and tissue clearing

Representative images of the maximum intensity projection from LSFM were compared between the passive CLARITY-treated retina and control retina, demonstrating the capacity of optical clearing to allow visualization of microvasculature that would otherwise be challenging with conventional imaging modalities (Figure S2A). Note the comparison of pre- and post-CLARITY treatment to allow imaging of the deep vascular plexus (Figure S2B).

Principal component analysis (PCA) of the vasculature

By reducing the dimensions of the data, PCA unravels important characteristics of the data set. It is a linear transformation that generates a new coordinate system from the data such that the greatest variance was introduced to the projected data points to new axes, ordered as components with decreasing variance by the projection of the data [1]. The $\boldsymbol{r}_{i,j}$ (i=1,2…N, j=1-3) represents the coordinate vectors from the vasculature (Equation 1). N represents the numbers of vessel elements inside the sliding window while j represents 3-D space dimensions (X, Y, and Z). The new coordinates are computed from the covariance matrix (Equations 1,2) of the data and applied to the eigenvector decomposition (Equations 3,4) process to derive the new axes known as principal components (PC). The PC1 is the eigenvector with the largest possible variance and each succeeding component such as PC2 and PC3 has the highest variance possible under the constraint that it is orthogonal to the preceding components. Lastly, the angle between vectors was calculated through the relation of the inner product (Equation 5).

$$Cov(r_j, r_k) = \frac{1}{N}\sum_{i=1}^{N}(r_{i,j} - \overline{r_j})(r_{i,k} - \overline{r_k}) = \sigma_{jk} \qquad \text{(Equation 1)}$$

$$Cov\ Matrix = \begin{bmatrix} \sigma_{xx} & \sigma_{xy} & \sigma_{xz} \\ \sigma_{yx} & \sigma_{yy} & \sigma_{yz} \\ \sigma_{zx} & \sigma_{zy} & \sigma_{zz} \end{bmatrix} \qquad \text{(Equation 2)}$$

Eigen Decomposition

$$Cov\ Matrix = \boldsymbol{V} \cdot \begin{bmatrix} \lambda_1 & 0 & 0 \\ 0 & \lambda_2 & 0 \\ 0 & 0 & \lambda_3 \end{bmatrix} \cdot \boldsymbol{V}^{-1} \qquad \text{(Equation 3)}$$

λ_1 , λ_2 , λ_3 are three eigen values

Eigen Vector ($\boldsymbol{V}$)

$$\boldsymbol{V} = [\overrightarrow{V_1}\ \overrightarrow{V_2}\ \overrightarrow{V_3}] \qquad \text{(Equation 4)}$$

Angle (θ)

$$\theta = \cos^{-1}\frac{\vec{u}\cdot\vec{v}}{|\vec{u}|\cdot|\vec{v}|} \qquad \text{(Equation 5)}$$

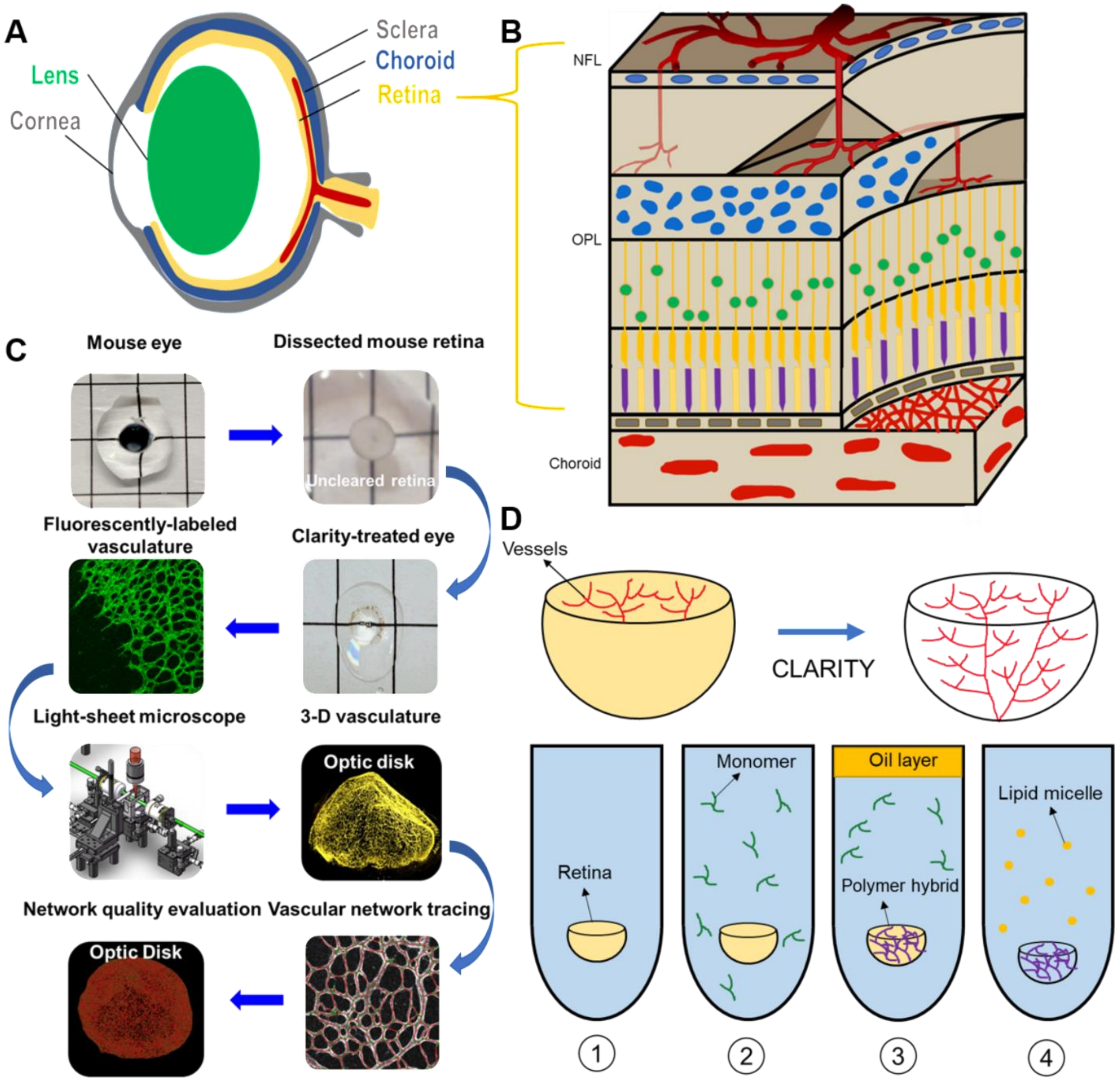

Figure 1. Light-sheet fluorescence microscopy (LSFM) to uncover the 3-D microvascular network. (A) A schematic illustration of the intact ocular globe, consisting of retinal and choroidal vasculature that were imaged and analyzed. **(B)** A superficial primary retinal vascular plexus lies in the nerve fiber layer (NFL), whereas the secondary plexus is located deep in the outer plexiform layer (OPL). **(C)** The pipeline to quantitatively analyze the 3-D hemispherical retinal vascular plexus using a optimized CLARITY method and LSFM. **(D)** An optimized passive CLARITY method was applied to optically clear the retina as articulated in the Methods section.

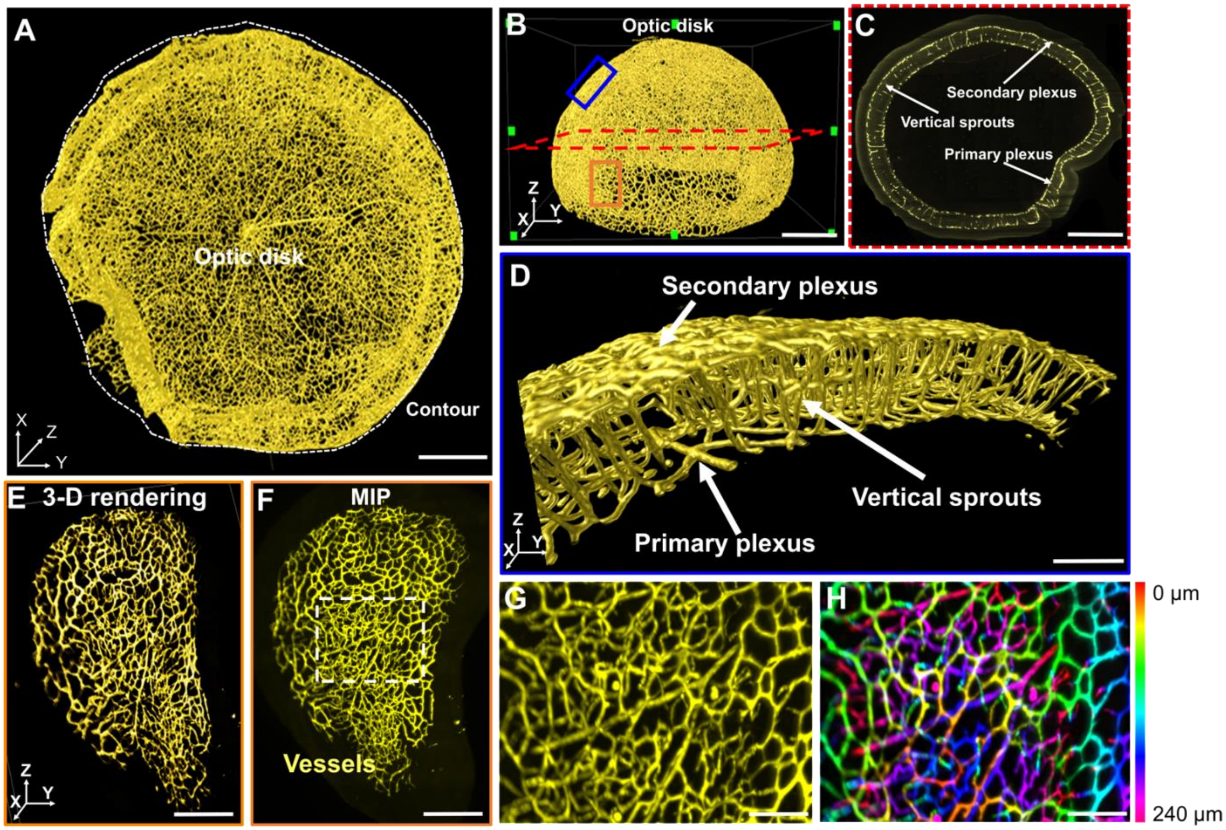

Figure 2. LSFM imaging of the unscathed 3-D hemispherical retina. (A-B) The unscathed vasculature in the 3-D retina was used to define representative regions of interest. The white dashed line depicts the contour of the hemispherical retina. **(C)** The vertical sprouts, bridging the primary and secondary plexus, are highlighted in the representative 2-D section (red dashed lines in **B**) of the retinal vascular network. **(D)** 3-D vertical sprouts between the primary and secondary vascular plexus (blue box in **B**) are located in the nerve fiber layer and the outer plexiform layer. **(E)** The 3-D and **(F)** 2-D peripheral regions (orange box in **B**) of the retina are enlarged. **(G)** The maximum intensity projection and **(H)** depth color-coded images of the capillary network (dashed box in **F**). Scale bars: (A-C) 500 μm; (D) 100 μm; (E-F) 300 μm; (G-H) 50 μm. Depth color-coded scale: 0~240 μm in (H).

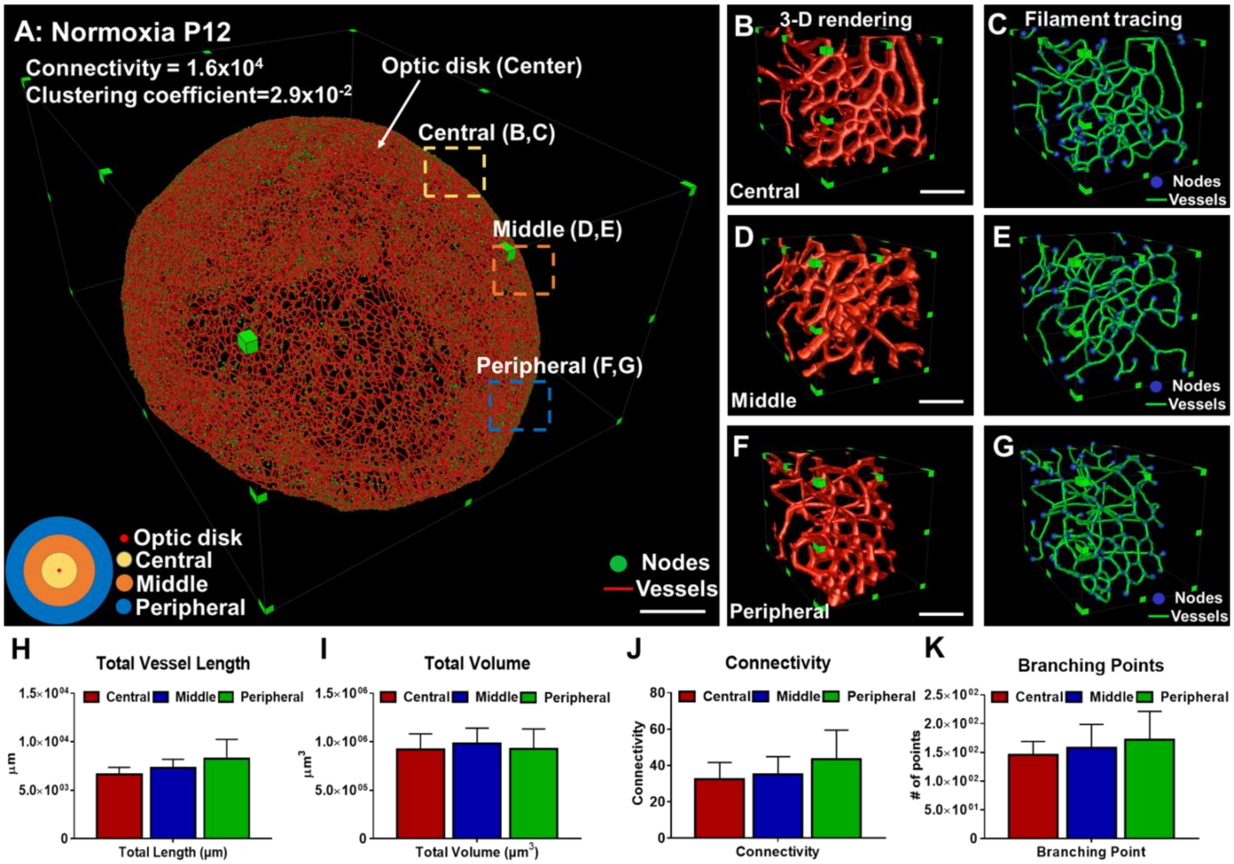

Figure 3. Quantitative comparison between the regions of a healthy vascular network in P12 mice. (A) 3-D filament tracing of retinal vasculature was performed from the unscathed hemisphere retina under normoxic conditions. Representative 3-D rendering **(B, D, F)** and filament tracing **(C, E, G)** of different volumes of interest (VOI) were demonstrated in the central (B, C), middle (D, E), and peripheral (F, G) regions of the unscathed retina. **(H-K)** Quantification of the morphological and topological parameters: vessel lengths, vessel volumes, connectivities, and branching points for different VOIs from the retina, demonstrating the capability and flexibility of our pipeline to quantify specific regions of interest ($p>0.05$ using one-way ANOVA with Tukey post hoc analysis, n = 5 per each region). Scale bar: (A) 500 µm; (B-G) 100 µm.

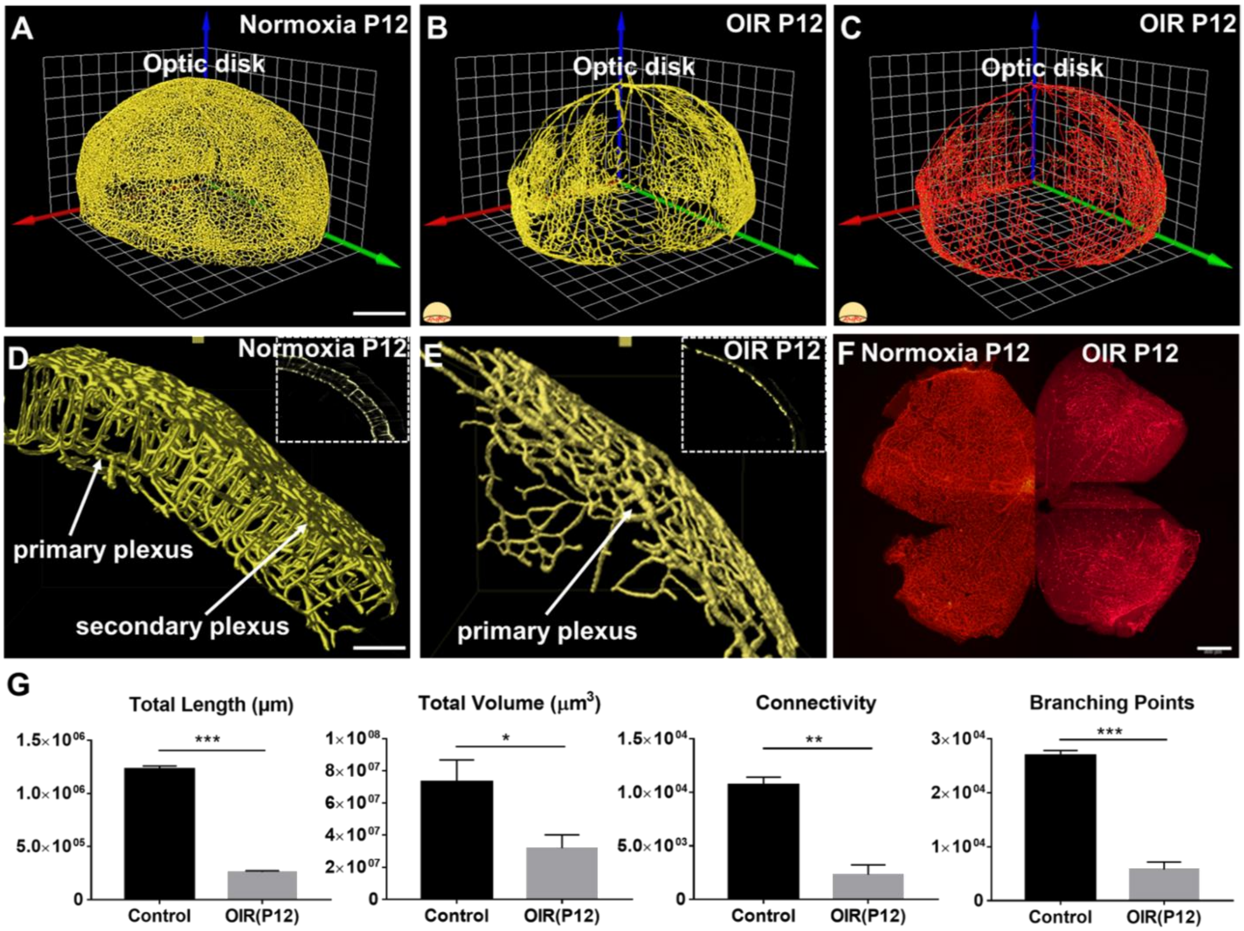

Figure 4. The 3-D vascular network highlights the spatial variations in microvascular obliteration that occurred in the secondary plexus and vertical sprouts following hyperoxia-induced injury in P12 mice. 3-D rendering of the retinal vasculature was performed from the **(A)** normoxia and **(B)** OIR intact retinas, revealing statistically significant obliteration of microvasculature in the OIR retina in P12 mice. **(C)** 3-D filament tracing of the vasculature was performed in the OIR group. **(D-E)** The results of 3-D rendering were compared between the two volumes of interest (VOIs) in the normoxia (D) vs. OIR (E) groups, demonstrating the absence of secondary plexus and vertical sprouts in the OIR mice. **(F)** Immunofluorescence images of flat-mount retinas only captured the phenotype in the primary plexus. **(G)** Quantification of the morphological and topological parameters revealed the statistically significant reduction in total vascular lengths, total volumes, connectivities and branching points in the OIR P12 mice (*$p < 0.05$, ** $p < 0.01$ *** $p < 0.001$, by unpaired two-tailed Student's t-test, n = 5 per group). Scale bar: 500 µm for A-C; 100 µm for D-E, 500 µm for F.

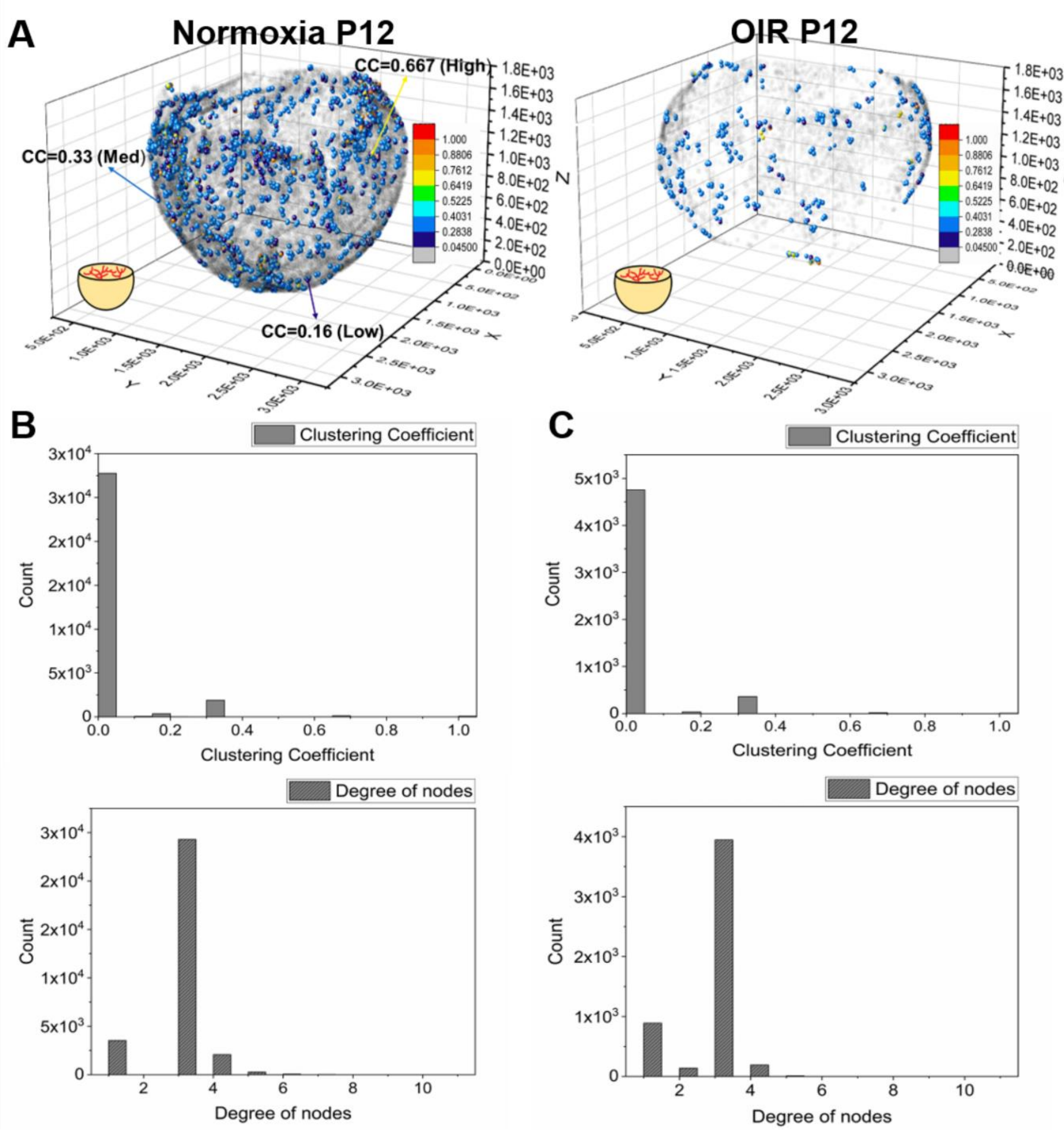

Figure 5. Quantification of the clustering coefficients for the retinal vasculature in P12 mice under normoxia and OIR conditions. (A) Representative 3-D scatter plots of the clustering coefficients demonstrate all the branching nodes and terminal nodes traced. ~90% of the nodes have a cluster coefficient of zero (grey nodes). ~10% of the nodes have clustering coefficients ranging from 0.05 to 1 in both normoxia and OIR mice. **(B)** The histogram of clustering coefficients and degree of nodes demonstrates that the majority of the nodes have three connecting neighbors with a paucity of neighbor connection in a normoxia mouse. **(C)** Despite the significant reduction of the global connectivity and number of nodes, the OIR mouse demonstrated the same trend in local patterns as the normoxia mouse, with the majority of the nodes sharing three connecting neighbors with a paucity of neighboring connections.

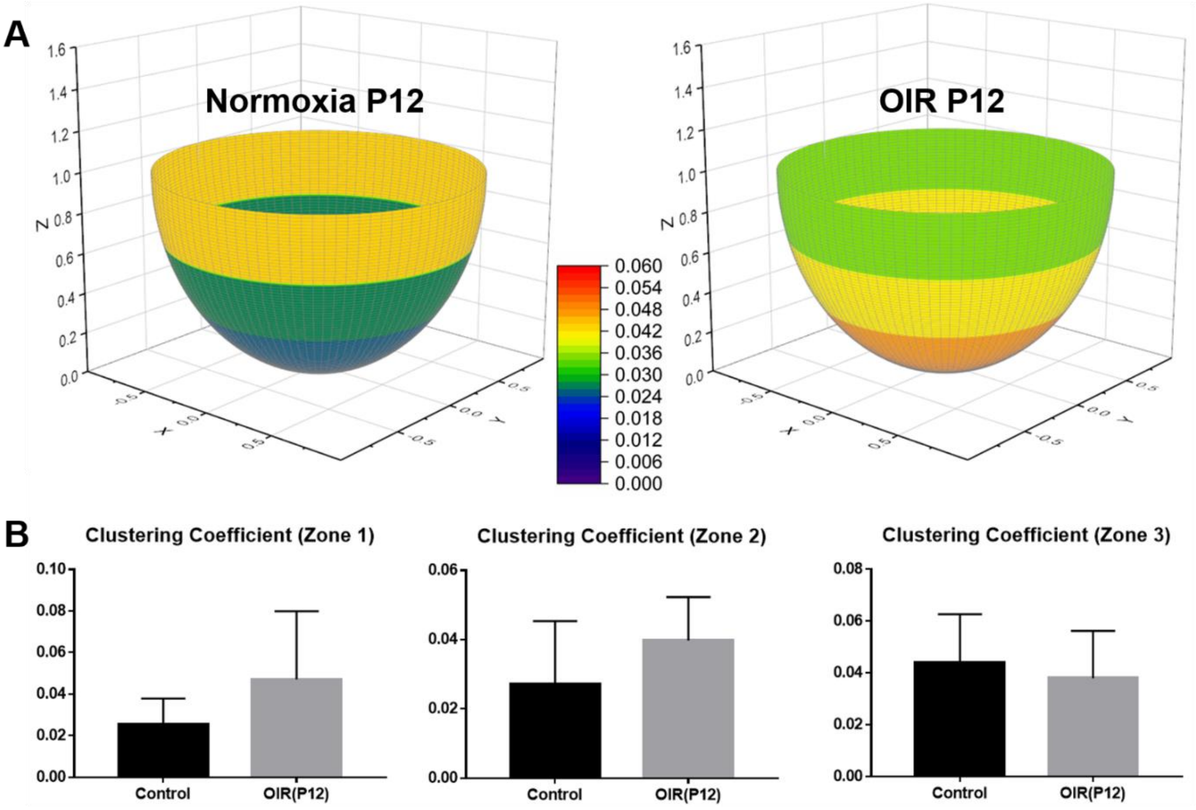

Figure 6. Average clustering coefficients in different regions of the retina in P12 normoxia and OIR mice. (A) The retinas were divided into three regions (central, middle, peripheral) as previously described. The average clustering coefficients of three individual regions were calculated and compared between the two groups. **(B)** The average clustering coefficients indicate no statistically significant difference among all three regions in both groups, supporting the notion that the local connections and basic structure of the network are preserved despite vaso-obliteration in OIR retinas ($p>0.05$ for all comparisons by unpaired two-tailed Student's t-test, n = 5 per group).

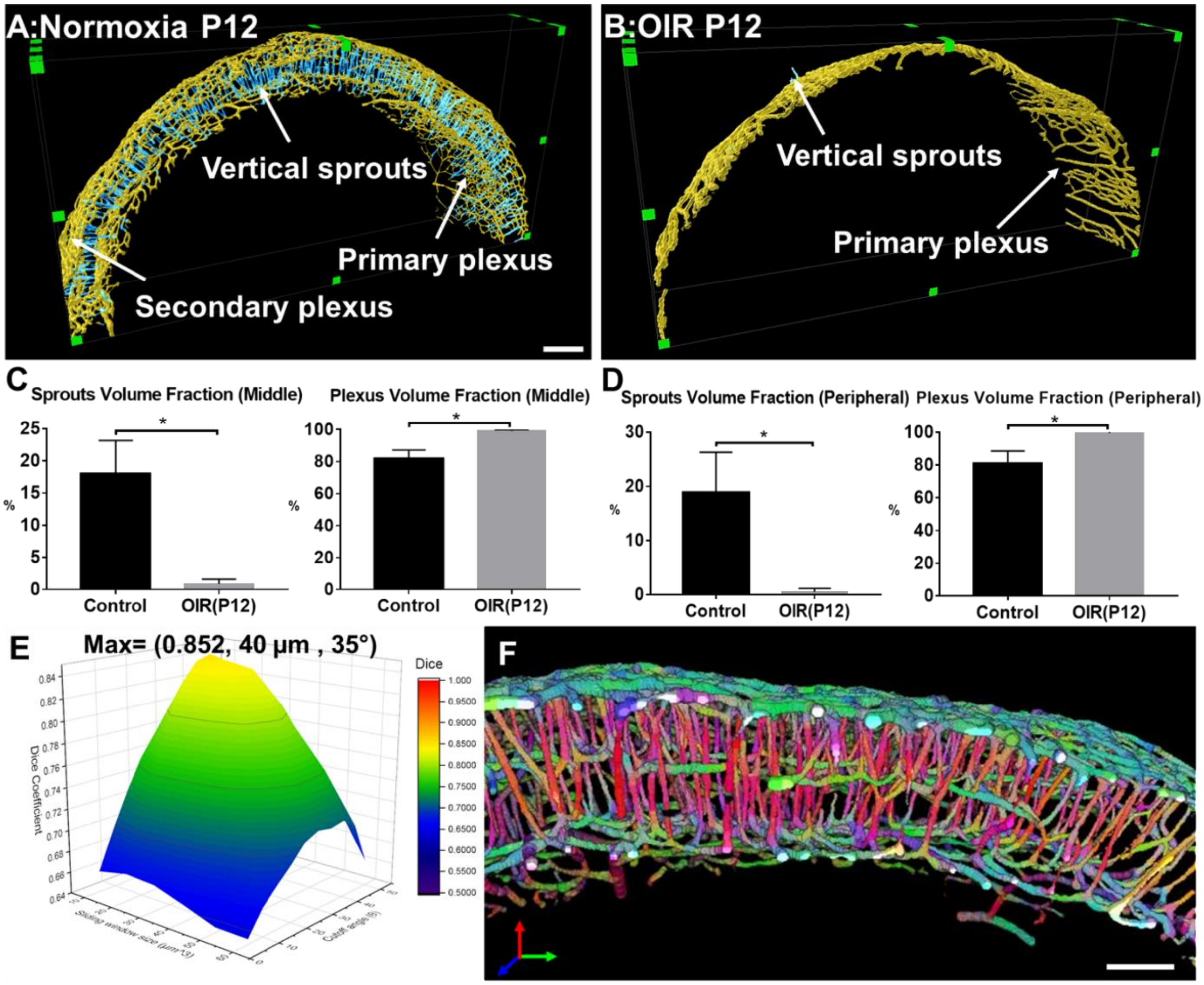

Figure 7. Quantitative analysis of the volumes for the vertical sprouts and plexuses in P12 normoxia and OIR mice. (A-B) Severe vaso-obliteration and depletion of vertical sprouts (in blue) and the secondary plexus (in yellow) were demonstrated in the 3-D rendering of the OIR group. **(C-D)** The quantification of the volume fraction of both sprouts and plexuses from both middle and peripheral regions indicate significant vessel depletion in the OIR group (*p < 0.05 vs. normoxia, by unpaired two-tailed Student's t-test, n = 5 per group). **(E)** The surface plot of the dice coefficients on different sizes of sliding windows and values of cutoff angles. **(F)** The representative VOI demonstrating the orientation color-coded 3-D rendering of the vascular network (X: Blue, Y: Green: Z: Red). Scale bar: 200 µm for A-B and 100 µm for F.

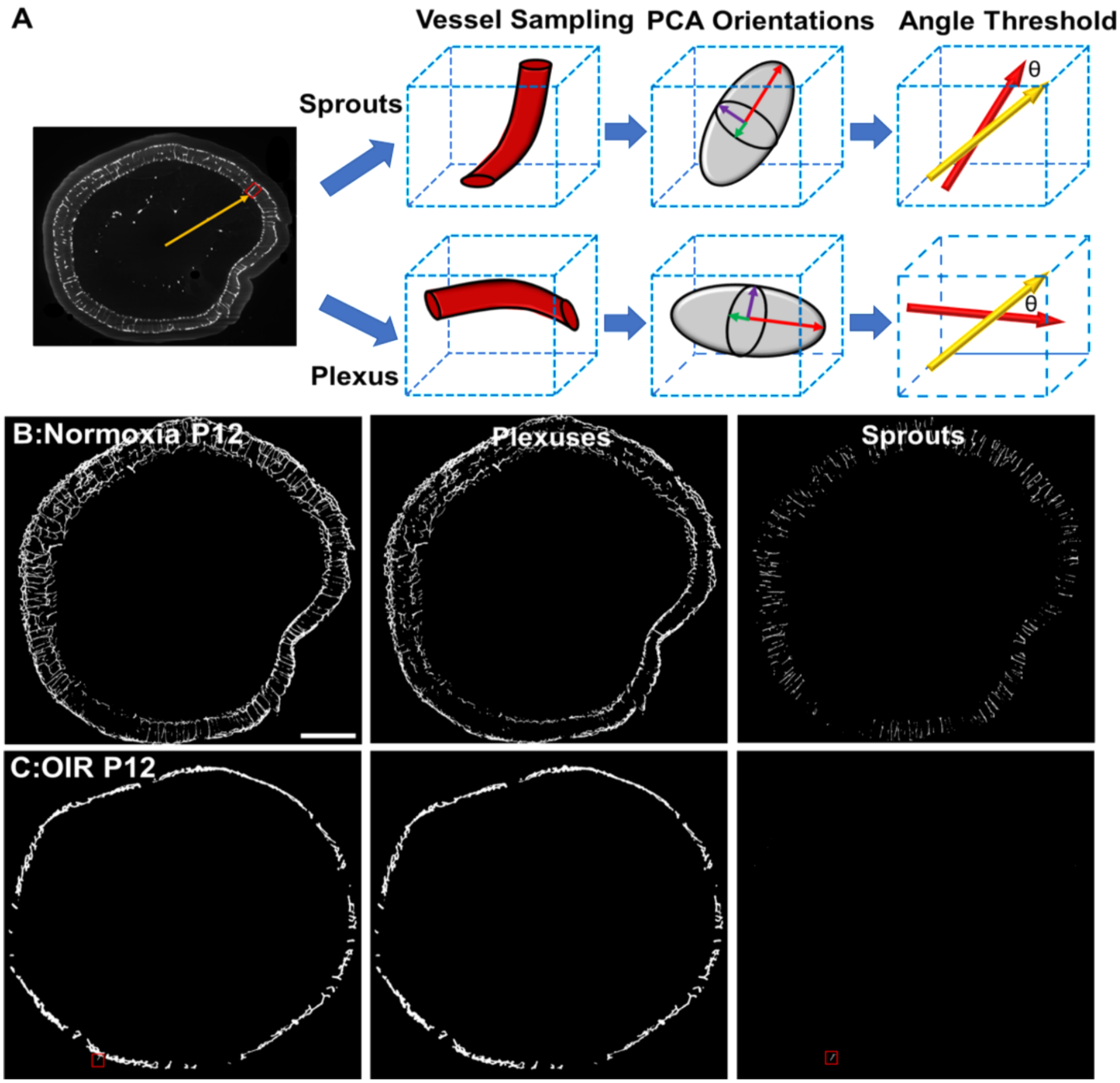

Figure S1. Schematic illustration and representative images of the automated segmentation for retinal vertical sprouts and plexuses in P12 mice in normoxia and OIR conditions. (A) The schematic plot indicates the distinct characteristics that distinguish the vertical sprouts and plexuses from each other which serve as the basis for the automated segmentation method. **(B-C)** The representative MIP images from the image stacks demonstrate the successful separation of the vertical sprouts and plexuses using automated segmentation for both normoxia and OIR P12. groups (sprout highlighted in a red box in OIR group). Scale bar: 500 µm.

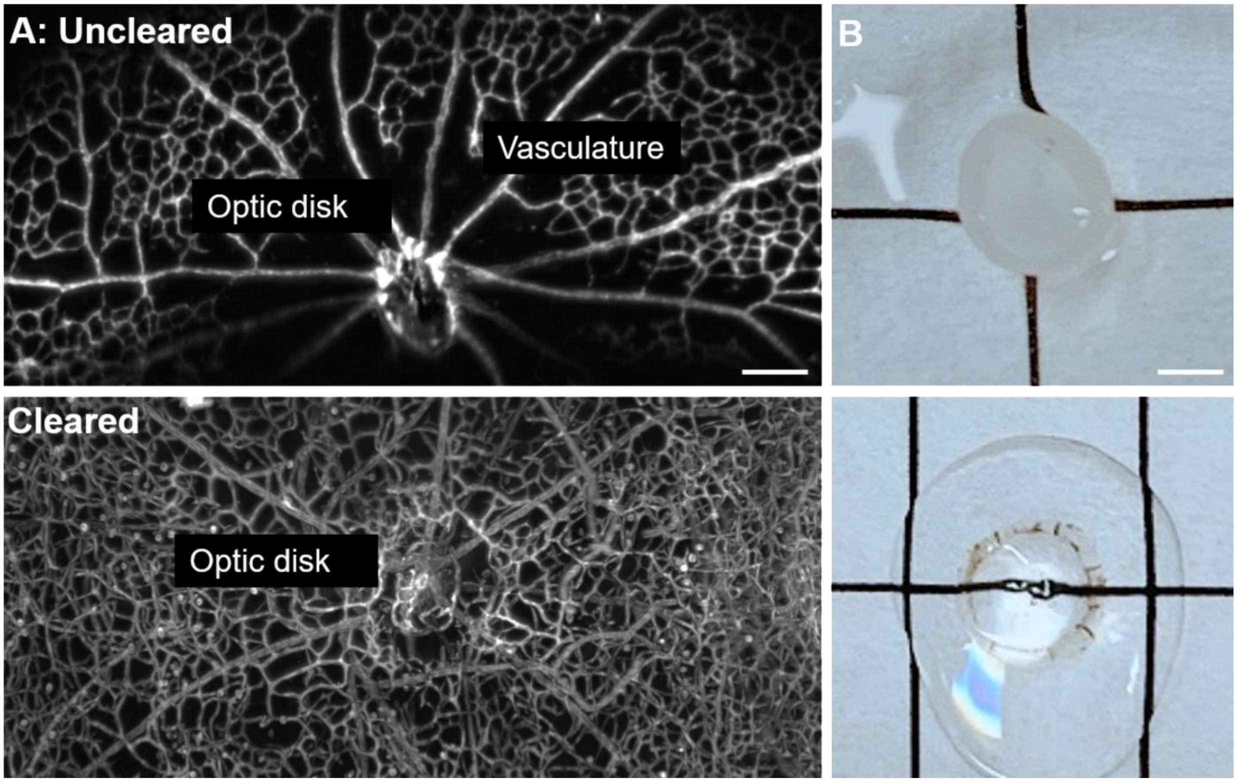

Figure S2. Representative images comparing the P12 murine retinas with and without tissue clearing. (A) The detailed vasculature seen after tissue clearing using the CLARITY method is demonstrated using the maximum intensity projection (bottom) in comparison to the uncleared retina (top). **(B)** Gross images of P12 mouse retinas prior to (top) and after (bottom) modified CLARITY treatment. Scale bar: (A) 100 µm; (B) 1 mm.

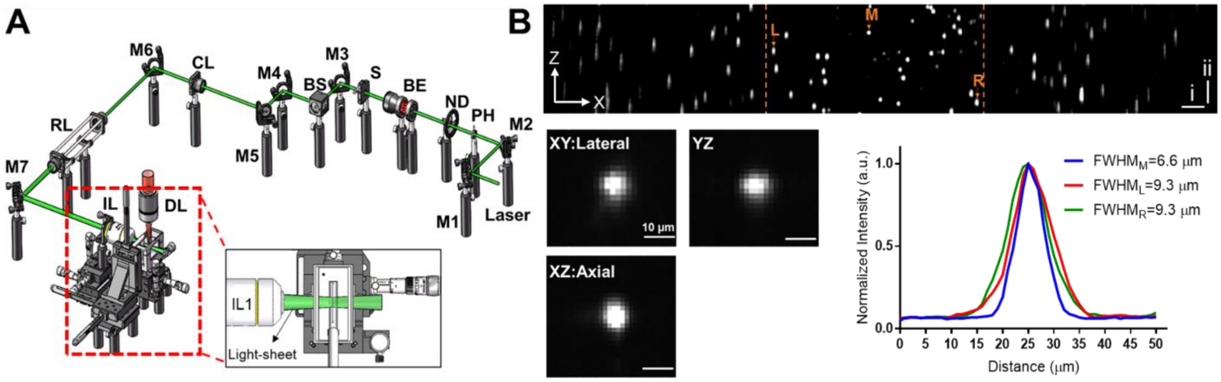

Figure S3. A schematic diagram of LSFM. (A) The diagram depicts the individual optical components that are featured in the LSFM system. M1-7: mirror; PH: pinhole; ND: neutral density filter; BE: beam expander; S: slit; BS: beam splitter, CL: cylindrical lens; RL: Relay lens; IL: illumination lens; DL: detection lens. **(B)** Representative images depicting the point spread function (PSF) of the 0.53 µm fluorescent bead in the lateral and axial directions, respectively. The XZ-view provides the characteristics of the confocal zone (bordered by orange dotted lines). Scale bars in panel B represent 100 µm (i-axis) and 50 µm (ii-axis).

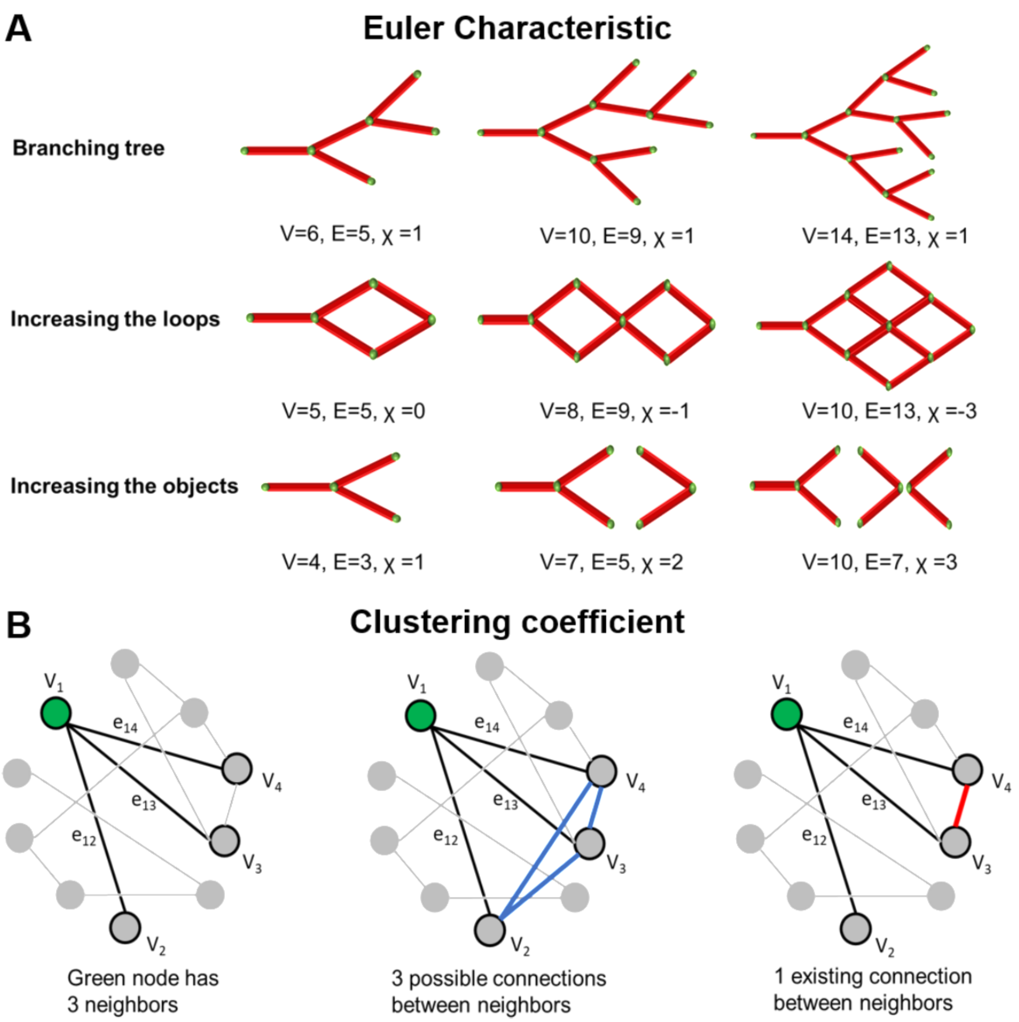

Figure S4. Schematic representation to quantify Euler characteristics and clustering coefficients. (A) Euler characteristic, χ, for the vascular network is determined by the numbers of loops and objects in a network rather than by the number of branching points. Both factors (loops and objects) generate new nodes and edges differently and contribute to the difference in the Euler characteristic value. The retinal vascular network is more reticular-like in structure (depicted by the middle row), resulting in a reduction in the χ value. V: Vertices, E: edges. **(B)** The definition of the clustering coefficient for a specific node (green) is calculated by dividing the existing links (red) over all possible links (blue) among neighboring nodes, such that the clustering coefficient of the representative schematic is 0.33.

Dice coefficient for normoxia group

	10 μm	20 μm	30 μm	40 μm	50 μm	60 μm
5°	0.66 ± 0.011	0.666 ± 0.015	0.664 ± 0.02	0.655 ± 0.015	0.645 ± 0.01	0.645 ± 0.014
10°	0.696 ± 0.026	0.714 ± 0.037	0.707 ± 0.039	0.697 ± 0.034	0.675 ± 0.028	0.666 ± 0.022
15°	0.728 ± 0.036	0.755 ± 0.053	0.75 ± 0.056	0.739 ± 0.047	0.712 ± 0.033	0.679 ± 0.039
20°	0.756 ± 0.041	0.795 ± 0.055	0.789 ± 0.055	0.775 ± 0.048	0.737 ± 0.039	0.692 ± 0.054
25°	0.776 ± 0.043	0.828 ± 0.045	0.822 ± 0.05	0.806 ± 0.039	0.756 ± 0.049	0.707 ± 0.055
30°	0.787 ± 0.045	0.845 ± 0.037	0.836 ± 0.041	0.817 ± 0.033	0.77 ± 0.044	0.713 ± 0.052
35°	0.793 ± 0.04	0.849 ± 0.032	0.841 ± 0.032	0.822 ± 0.023	0.768 ± 0.042	0.71 ± 0.049
40°	0.792 ± 0.035	0.841 ± 0.022	0.836 ± 0.017	0.807 ± 0.015	0.763 ± 0.04	0.712 ± 0.04
45°	0.784 ± 0.03	0.825 ± 0.014	0.817 ± 0.009	0.784 ± 0.014	0.749 ± 0.029	0.703 ± 0.036
50°	0.768 ± 0.028	0.789 ± 0.022	0.776 ± 0.026	0.75 ± 0.03	0.714 ± 0.023	0.664 ± 0.046

Table S1. Average dice coefficients of various combinations of sliding window size and cutoff angle in the normoxia group.

Dice coefficient for OIR group

	10 μm	20 μm	30 μm	40 μm	50 μm	60 μm
5°	0.865 ± 0.04	0.868 ± 0.04	0.873 ± 0.037	0.874 ± 0.036	0.874 ± 0.036	0.874 ± 0.036
10°	0.842 ± 0.062	0.851 ± 0.058	0.872 ± 0.035	0.879 ± 0.034	0.887 ± 0.036	0.877 ± 0.035
15°	0.821 ± 0.072	0.839 ± 0.062	0.894 ± 0.053	0.899 ± 0.049	0.886 ± 0.037	0.9 ± 0.044
20°	0.807 ± 0.07	0.828 ± 0.057	0.864 ± 0.077	0.898 ± 0.049	0.883 ± 0.036	0.884 ± 0.032
25°	0.796 ± 0.076	0.82 ± 0.064	0.864 ± 0.065	0.896 ± 0.052	0.907 ± 0.047	0.881 ± 0.029
30°	0.777 ± 0.081	0.813 ± 0.068	0.855 ± 0.061	0.882 ± 0.045	0.892 ± 0.041	0.88 ± 0.029
35°	0.757 ± 0.089	0.8 ± 0.071	0.848 ± 0.064	0.882 ± 0.029	0.889 ± 0.038	0.89 ± 0.016
40°	0.739 ± 0.094	0.782 ± 0.071	0.834 ± 0.066	0.882 ± 0.027	0.874 ± 0.06	0.892 ± 0.014
45°	0.72 ± 0.1	0.767 ± 0.08	0.826 ± 0.07	0.874 ± 0.027	0.871 ± 0.061	0.883 ± 0.02
50°	0.7 ± 0.103	0.74 ± 0.092	0.793 ± 0.102	0.799 ± 0.096	0.794 ± 0.143	0.798 ± 0.106

Table S2. Average dice coefficients of various combinations of sliding window size and cutoff angle in the OIR group.

Dice coefficient for both groups

	10 μm	20 μm	30 μm	40 μm	50 μm	60 μm
5°	0.763 ± 0.113	0.767 ± 0.111	0.769 ± 0.115	0.765 ± 0.12	0.76 ± 0.125	0.76 ± 0.125
10°	0.769 ± 0.088	0.783 ± 0.085	0.789 ± 0.095	0.788 ± 0.102	0.781 ± 0.117	0.771 ± 0.116
15°	0.775 ± 0.069	0.797 ± 0.068	0.822 ± 0.092	0.819 ± 0.096	0.799 ± 0.098	0.79 ± 0.124
20°	0.782 ± 0.057	0.811 ± 0.054	0.826 ± 0.071	0.836 ± 0.079	0.81 ± 0.085	0.788 ± 0.111
25°	0.786 ± 0.054	0.824 ± 0.049	0.843 ± 0.056	0.851 ± 0.063	0.831 ± 0.092	0.794 ± 0.102
30°	0.782 ± 0.057	0.829 ± 0.05	0.846 ± 0.047	0.849 ± 0.049	0.831 ± 0.076	0.796 ± 0.098
35°	0.775 ± 0.062	0.824 ± 0.054	0.845 ± 0.044	0.852 ± 0.04	0.829 ± 0.074	0.8 ± 0.103
40°	0.765 ± 0.066	0.812 ± 0.054	0.835 ± 0.04	0.844 ± 0.044	0.819 ± 0.074	0.802 ± 0.1
45°	0.752 ± 0.07	0.796 ± 0.056	0.821 ± 0.041	0.829 ± 0.052	0.81 ± 0.077	0.793 ± 0.101
50°	0.734 ± 0.073	0.764 ± 0.061	0.784 ± 0.063	0.775 ± 0.065	0.754 ± 0.094	0.731 ± 0.1

Table S3. Average dice coefficients of various combinations of sliding window size and cutoff angle in both groups combined.

References

1. Liu C-H, Wang Z, Sun Y, Chen J. Animal models of ocular angiogenesis: from development to pathologies. FASEB J. 2017; 31: 4665-81.
2. Selvam S, Kumar T, Fruttiger M. Retinal vasculature development in health and disease. Prog Retin Eye Res. 2018; 63: 1-19.
3. Fruttiger M. Development of the retinal vasculature. Angiogenesis. 2007; 10: 77-88.
4. Zin A, Gole GA. Retinopathy of prematurity-incidence today. Clin Perinatol. 2013; 40: 185-200.
5. Cavallaro G, Filippi L, Bagnoli P, La Marca G, Cristofori G, Raffaeli G, et al. The pathophysiology of retinopathy of prematurity: an update of previous and recent knowledge. Acta Ophthalmol. 2014; 92: 2-20.
6. Gariano RF, Gardner TW. Retinal angiogenesis in development and disease. Nature. 2005; 438: 960.
7. Semeraro F, Cancarini A, Rezzola S, Romano M, Costagliola C. Diabetic retinopathy: vascular and inflammatory disease. J Diabetes Res. 2015; 2015.
8. Antonetti DA, Barber AJ, Bronson SK, Freeman WM, Gardner TW, Jefferson LS, et al. Diabetic retinopathy: seeing beyond glucose-induced microvascular disease. Diabetes. 2006; 55: 2401-11.
9. Lee D-H, Yi HC, Bae SH, Cho JH, Choi SW, Kim H. Risk factors for retinal microvascular impairment in type 2 diabetic patients without diabetic retinopathy. PloS One. 2018; 13: e0202103.
10. Shah PK, Prabhu V, Karandikar SS, Ranjan R, Narendran V, Kalpana N. Retinopathy of prematurity: past, present and future. World J Clin Pediatr. 2016; 5: 35.
11. Talisa E, Chin AT, Bonini Filho MA, Adhi M, Branchini L, Salz DA, et al. Detection of microvascular changes in eyes of patients with diabetes but not clinical diabetic retinopathy using optical coherence tomography angiography. Retina. 2015; 35: 2364-70.
12. Dimitrova G, Chihara E, Takahashi H, Amano H, Okazaki K. Quantitative retinal optical coherence tomography angiography in patients with diabetes without diabetic retinopathy. Invest Ophthalmol Vis Sci. 2017; 58: 190-6.
13. D'Amato G, Luxan G, del Monte-Nieto G, Martinez-Poveda B, Torroja C, Walter W, et al. Sequential Notch activation regulates ventricular chamber development. Nature cell biology. 2016; 18: 7-20.
14. Takase N, Nozaki M, Kato A, Ozeki H, Yoshida M, Ogura Y. Enlargement of foveal avascular zone in diabetic eyes evaluated by en face optical coherence tomography angiography. Retina. 2015; 35: 2377-83.
15. Cao D, Yang D, Huang Z, Zeng Y, Wang J, Hu Y, et al. Optical coherence tomography angiography discerns preclinical diabetic retinopathy in eyes of patients with type 2 diabetes without clinical diabetic retinopathy. Acta Diabetol. 2018; 55: 469-77.
16. Stahl A, Connor KM, Sapieha P, Chen J, Dennison RJ, Krah NM, et al. The mouse retina as an angiogenesis model. Invest Ophthalmol Vis Sci. 2010; 51: 2813-26.
17. Connor KM, Krah NM, Dennison RJ, Aderman CM, Chen J, Guerin KI, et al. Quantification of oxygen-induced retinopathy in the mouse: a model of vessel loss, vessel regrowth and pathological angiogenesis. Nat Protoc. 2009; 4: 1565.
18. Milde F, Lauw S, Koumoutsakos P, Iruela-Arispe ML. The mouse retina in 3D: quantification of vascular growth and remodeling. Integr Biol. 2013; 5: 1426-38.

19. Lin J, Hu J, Schlotterer A, Wang J, Kolibabka M, Awwad K, et al. Protective effect of Soluble Epoxide Hydrolase Inhibition in Retinal Vasculopathy associated with Polycystic Kidney Disease. Theranostics. 2020; 10: 7857.
20. Jiang D, Xiong G, Feng H, Zhang Z, Chen P, Yan B, et al. Donation of mitochondria by iPSC-derived mesenchymal stem cells protects retinal ganglion cells against mitochondrial complex I defect-induced degeneration. Theranostics. 2019; 9: 2395.
21. Liu C, Yao M-D, Li C-P, Shan K, Yang H, Wang J-J, et al. Silencing of circular RNA-ZNF609 ameliorates vascular endothelial dysfunction. Theranostics. 2017; 7: 2863.
22. Singh JN, Nowlin TM, Seedorf GJ, Abman SH, Shepherd DP. Quantifying three-dimensional rodent retina vascular development using optical tissue clearing and light-sheet microscopy. J Biomed Opt. 2017; 22: 076011.
23. Prahst C, Ashrafzadeh P, Mead T, Figueiredo A, Chang K, Richardson D, et al. Mouse retinal cell behaviour in space and time using light sheet fluorescence microscopy. Elife. 2020; 9: e49779.
24. Ding Y, Ma J, Langenbacher AD, Baek KI, Lee J, Chang C-C, et al. Multiscale light-sheet for rapid imaging of cardiopulmonary system. JCI insight. 2018; 3.
25. Baek KI, Ding Y, Chang C-C, Chang M, Packard RRS, Hsu JJ, et al. Advanced microscopy to elucidate cardiovascular injury and regeneration: 4D light-sheet imaging. Prog Biophys Mol Biol. 2018; 138: 105-15.
26. Power RM, Huisken J. A guide to light-sheet fluorescence microscopy for multiscale imaging. Nat Methods. 2017; 14: 360.
27. McDole K, Guignard L, Amat F, Berger A, Malandain G, Royer LA, et al. In toto imaging and reconstruction of post-implantation mouse development at the single-cell level. Cell. 2018; 175: 859-76. e33.
28. Ding Y, Abiri A, Abiri P, Li S, Chang C-C, Baek KI, et al. Integrating light-sheet imaging with virtual reality to recapitulate developmental cardiac mechanics. JCI insight. 2017; 2.
29. Stelzer EH. Light-sheet fluorescence microscopy for quantitative biology. Nat Methods. 2015; 12: 23-6.
30. Weinhaus RS, Burke JM, Delori FC, Snodderly DM. Comparison of fluorescein angiography with microvascular anatomy of macaque retinas. Exp Eye Res. 1995; 61: 1-16.
31. Calzi SL, Shaw LC, Moldovan L, Shelley WC, Qi X, Racette L, et al. Progenitor cell combination normalizes retinal vascular development in the oxygen-induced retinopathy (OIR) model. JCI insight. 2019; 4.
32. Chang B. Mouse models for studies of retinal degeneration and diseases. Retinal Degeneration: Springer; 2012. p. 27-39.
33. Zhao S, Todorov MI, Cai R, Rami A-M, Steinke H, Kemter E, et al. Cellular and molecular probing of intact human organs. Cell. 2020; 180: 796-812. e19.
34. Kim J, Kim YH, Kim J, Bae H, Lee D-H, Kim KH, et al. YAP/TAZ regulates sprouting angiogenesis and vascular barrier maturation. J Clin Invest. 2017; 127: 3441-61.
35. Yoon C-H, Choi Y-E, Cha YR, Koh S-J, Choi J-i, Kim T-W, et al. Diabetes-induced Jagged1 overexpression in endothelial cells causes retinal capillary regression in a murine model of diabetes mellitus: Insights into diabetic retinopathy. Circulation. 2016; 134: 233-47.

36. Wilhelm K, Happel K, Eelen G, Schoors S, Oellerich MF, Lim R, et al. FOXO1 couples metabolic activity and growth state in the vascular endothelium. Nature. 2016; 529: 216.
37. Dubrac A, Künzel SE, Künzel SH, Li J, Chandran RR, Martin K, et al. Nck-dependent pericyte migration promotes pathological neovascularization in ischemic retinopathy. Nat Commun. 2018; 9.
38. Liu Y, Yang Z, Lai P, Huang Z, Sun X, Zhou T, et al. Bcl-6-directed follicular helper T cells promote vascular inflammatory injury in diabetic retinopathy. Theranostics. 2020; 10: 4250.
39. Sun J, Huang W, Yang S-f, Zhang X-p, Yu Q, Zhang Z-q, et al. Gαi1 and Gαi3mediate VEGF-induced VEGFR2 endocytosis, signaling and angiogenesis. Theranostics. 2018; 8: 4695.
40. Wang Y, Rajala A, Cao B, Ranjo-Bishop M, Agbaga M-P, Mao C, et al. Cell-specific promoters enable lipid-based nanoparticles to deliver genes to specific cells of the retina in vivo. Theranostics. 2016; 6: 1514.
41. Lee J, Fei P, Packard RRS, Kang H, Xu H, Baek KI, et al. 4-Dimensional light-sheet microscopy to elucidate shear stress modulation of cardiac trabeculation. J Clin Invest. 2016; 126: 1679-90.
42. Richardson DS, Lichtman JW. Clarifying tissue clearing. Cell. 2015; 162: 246-57.
43. Tomer R, Ye L, Hsueh B, Deisseroth K. Advanced CLARITY for rapid and high-resolution imaging of intact tissues. Nat Protoc. 2014; 9: 1682.
44. Sung K, Ding Y, Ma J, Chen H, Huang V, Cheng M, et al. Simplified three-dimensional tissue clearing and incorporation of colorimetric phenotyping. Sci Rep. 2016; 6: 30736.
45. Gradinaru V, Treweek J, Overton K, Deisseroth K. Hydrogel-tissue chemistry: Principles and applications. Annu Rev Biophys. 2018; 47: 355-76.
46. Richardson DS, Lichtman JW. SnapShot: tissue clearing. Cell. 2017; 171: 496-. e1.
47. Chung K, Wallace J, Kim S-Y, Kalyanasundaram S, Andalman AS, Davidson TJ, et al. Structural and molecular interrogation of intact biological systems. Nature. 2013; 497: 332.
48. Renier N, Wu Z, Simon DJ, Yang J, Ariel P, Tessier-Lavigne M. iDISCO: a simple, rapid method to immunolabel large tissue samples for volume imaging. Cell. 2014; 159: 896-910.
49. Mozaffari S, Jaedicke V, Larocca F, Tiruveedhula P, Roorda A. Versatile multi-detector scheme for adaptive optics scanning laser ophthalmoscopy. Biomed Opt Express. 2018; 9: 5477-88.
50. Mozaffari S, LaRocca F, Jaedicke V, Tiruveedhula P, Roorda A. Wide-vergence, multi-spectral adaptive optics scanning laser ophthalmoscope with diffraction-limited illumination and collection. Biomed Opt Express. 2020; 11: 1617-32.
51. Burns SA, Elsner AE, Chui TY, VanNasdale DA, Clark CA, Gast TJ, et al. In vivo adaptive optics microvascular imaging in diabetic patients without clinically severe diabetic retinopathy. Biomed Opt Express. 2014; 5: 961-74.
52. Sapoznik KA, Luo T, De Castro A, Sawides L, Warner RL, Burns SA. Enhanced retinal vasculature imaging with a rapidly configurable aperture. Biomed Opt Express. 2018; 9: 1323-33.

53. An L, Shen T, Wang RK. Using ultrahigh sensitive optical microangiography to achieve comprehensive depth resolved microvasculature mapping for human retina. J Biomed Opt. 2011; 16: 106013.

54. Chu Z, Chen C-L, Zhang Q, Pepple K, Durbin M, Gregori G, et al. Complex signal-based optical coherence tomography angiography enables in vivo visualization of choriocapillaris in human choroid. J Biomed Opt. 2017; 22: 121705.

55. De Carlo TE, Romano A, Waheed NK, Duker JS. A review of optical coherence tomography angiography (OCTA). Int J Retina Vitreous. 2015; 1: 5.

56. Legland D, Kiêu K, Devaux M-F. Computation of Minkowski measures on 2D and 3D binary images. Image Analysis & Stereology. 2011; 26: 83-92.

57. Nagel W, Ohser J, Pischang K. An integral-geometric approach for the Euler-Poincaré characteristic of spatial images. J Microsc. 2000; 198: 54-62.

58. Toriwaki J, Yonekura T. Euler number and connectivity indexes of a three dimensional digital picture. Forma. 2002; 17: 183-209.

59. Nyengaard JR. Stereologic methods and their application in kidney research. J Am Soc Nephrol. 1999; 10: 1100-23.

60. Willführ A, Brandenberger C, Piatkowski T, Grothausmann R, Nyengaard JR, Ochs M, et al. Estimation of the number of alveolar capillaries by the Euler number (Euler-Poincaré characteristic). Am J Physiol Lung Cell Mol Physiol. 2015; 309: L1286-L93.

61. Muehlfeld C. Quantitative morphology of the vascularisation of organs: a stereological approach illustrated using the cardiac circulation. Ann Anat. 2014; 196: 12-9.

62. Odgaard A, Gundersen H. Quantification of connectivity in cancellous bone, with special emphasis on 3-D reconstructions. Bone. 1993; 14: 173-82.

63. Amat-Roldan I, Berzigotti A, Gilabert R, Bosch J. Assessment of hepatic vascular network connectivity with automated graph analysis of dynamic contrast-enhanced US to evaluate portal hypertension in patients with cirrhosis: a pilot study. Radiology. 2015; 277: 268-76.

64. Czech W, Dzwinel W, Goryczka S, Arodz T, Dudek AZ. Exploring complex networks with graph investigator research application. Comput Inform. 2012; 30: 381-410.

65. Bullmore E, Sporns O. Complex brain networks: graph theoretical analysis of structural and functional systems. Nat Rev Neurosci. 2009; 10: 186.

66. Sun M, Wadehra M, Casero D, Lin M-C, Aguirre B, Parikh S, et al. Epithelial membrane protein 2 (Emp2) promotes VEGF-induced pathological neovascularization in murine oxygen-induced retinopathy. Invest Ophthalmol Vis Sci. 2020; 61: 3-.

67. Ding Y, Lee J, Ma J, Sung K, Yokota T, Singh N, et al. Light-sheet fluorescence imaging to localize cardiac lineage and protein distribution. Scientific reports. 2017; 7: 42209.

68. Preibisch S, Saalfeld S, Tomancak P. Globally optimal stitching of tiled 3D microscopic image acquisitions. Bioinformatics. 2009; 25: 1463-5.

69. Fehrenbach J, Weiss P, Lorenzo C. Variational algorithms to remove stationary noise: applications to microscopy imaging. IEEE Trans Image Process. 2012; 21: 4420-30.

70. Fehrenbach J, Weiss P. Processing stationary noise: Model and parameter selection in variational methods. SIAM J Imaging Sci. 2014; 7: 613-40.

71. Watts DJ, Strogatz SH. Collective dynamics of ‘small-world’networks. Nature. 1998; 393: 440.

72. Taha AA, Hanbury A. Metrics for evaluating 3D medical image segmentation: analysis, selection, and tool. BMC Med Imaging. 2015; 15: 29.
73. Crum WR, Camara O, Hill DL. Generalized overlap measures for evaluation and validation in medical image analysis. IEEE Trans Med Imaging. 2006; 25: 1451-61.
74. Sudre CH, Li W, Vercauteren T, Ourselin S, Cardoso MJ. Generalised dice overlap as a deep learning loss function for highly unbalanced segmentations. Deep learning in medical image analysis and multimodal learning for clinical decision support: Springer; 2017. p. 240-8.

Chapter IV

Liver Electrical Impedance Tomography for Early Identification of Fatty Infiltrate in Obesity

Chang, C.C., Huang, Z.Y., Shih, S.F., Luo, Y., Ko, A., Cui, Q., Sumner J., Cavallero, S., Das, S., Gao, W., Sinsheimer, J., Bui, A., Jacobs, J.P., Pajukanta, P., Wu, H., Tai, Y.C., Li, Z., and Hsiai, T.K.

* Equal contribution.

This chapter is reproduced from the original article published in **bioRxiv** 2020.12.21.423854 and approved by the co-authors

Introduction

Obesity is the major risk factor associated with the development of nonalcoholic fatty liver disease (NAFLD), affecting more than a third of American. adults, and the prevalence of severe obesity (BMI ≥ 35 $kg \cdot m^{-2}$) is continuing to rise nationwide[1]. NAFLD is now one of the most common causes of cirrhosis requiring liver transplantation in the Western world[2,3]. A clinical challenge in the management of NAFLD resides in non-invasively detecting fatty liver (i.e., simple hepatic steatosis) and monitoring disease progression to steatohepatitis (hepatic inflammation), fibrosis (liver scarring), and ultimately cirrhosis[4,5]. While liver biopsy remains the gold standard for diagnosis of NAFLD, it carries a substantial risk of bleeding and is confounded by sampling bias and inter-observer variability[6]. While liver MRI proton-density fat fraction (PDFF) is recognized as the non-invasive reference standard for validating liver fat infiltrate[7,8], it is costly for underserved communities. While ultrasound is non-invasive, it is limited by spatial resolution and operator dependency [9,10]. Thus, there remains an unmet clinical need to develop a non-invasive and economic method that is operator-independent and portable for early detection of fatty liver disease.

To this end, we demonstrated in prior study the theoretical and experimental basis of electrical impedance tomography (EIT) for measuring liver fat content in the New Zealand White Rabbit model of atherosclerosis and fatty liver disease[11]. By virtue of tissue-specific electrical conductivity, fatty infiltrate in the liver was characterized by its frequency-dependent electrical impedance (Z) in response to applied alternating current (AC)[11]. At low frequencies, the cell membranes impede the current flow, resulting in high conductivity, whereas at high frequency, they serve as the imperfect capacitors, resulting in tissue- and fluid-dependent impedance. This impedimetric property enables the development of a multi-electrode array to measure tissue-specific conductivity, morphology, and changes in 3-D volume in response to changes in cardiac output or lung capacity[12-15]. A host of literature has demonstrated the application of EIT for functional studies of the brain, cardiac stroke volume, and respiratory ventilation (transthoracic impedance pneumography)[16-19].

In this context, we reconstructed liver frequency-dependent conductivity distribution with the multi-electrode array-acquired voltage data to demonstrate liver EIT.[11] Applying the multi-electrode array, we performed EIT voltage measurements by biasing electrical currents (at 2-4 mA and 50-250 kHz) to the upper abdomen. The currents penetrated the body to varying depths, and the resulting boundary voltages were acquired by the electrodes. In response to the applied alternating current (AC), muscle and blood are more conductive than fat, bone, or lung tissue due to the varying free ion content.[20,21] Fat-free tissue such as skeletal muscle carries high water (~73%) and electrolyte (ions and proteins) content, allowing for efficient electrical conductivity ($S \cdot m^{-1}$), whereas fat-infiltrated tissue such as fatty liver (steatosis)[22] is anhydrous, resulting in a reduction in conductivity[23]. This impedimetric property provides the theoretical principle to apply the portable liver EIT for the early identification of fatty liver infiltrate with translational implications for the prevention of liver fibrosis and major adverse coronary events (MACE). Unlike EIT for cardiopulmonary function focusing on the differential conductivity [12-15, 16-19], we addressed the ill-posed inverse problem to demonstrate the absolute liver conductivity in 2-D.

We recruited overweight/obese subjects to undergo liver 3T MRI scans, followed by voltage measurements via the flexible multi-electrode array (Swisstom AG, Switzerland) for EIT. MRI images were acquired to provide subject-specific *a priori* knowledge of the liver geometry for performing liver segmentation and positioning to solve the inverse problem of EIT reconstruction. We further compared the subject-specific EIT conductivity with the liver MRI proton-density fat fraction PDFF as a reference standard for validating fatty liver infiltrate[24]. Next, we performed the Pearson's correlation analyses between the EIT liver conductivity and demographic parameters, and also performed the correlation analyses between MRI PDFF and demographics parameters in terms of gender, BMI ($kg \cdot m^{-2}$), age (years), waist circumference (cm), height (cm), and weight (kg). Following Bonferroni correction for multi-testing, correlation analyses revealed that liver EIT conductivity ($S \cdot m^{-1}$) and MRI PDFF were not correlated with these demographics; however, the EIT liver conductivity map was negatively correlated with the MRI PDFF. This inverse correlation between the EIT liver conductivity and MRI PDFF holds promises for developing non-invasive and portable liver EIT for early detection of silent fatty liver content in the healthy overweight/obese individuals

Results

Schematic workflow illustrates the steps to compare and validate the EIT reconstruction with MRI

The recruitment of subjects followed the guidelines of the Human Subjects Protection Committee of UCLA, described in the method section. For the workflow and schematic setup (**Fig 1**), each subject would undergo a different series of MRI scans, including a 30-min MRI multi-echo imaging to acquire the PDFF map of the liver. Next, EIT measurement with 32 electrodes attached to the subject's abdominal region was performed right after the MRI scan to obtain the corresponding liver fat measurement. The average PDFF of the liver, as well as the EIT conductivity of the liver, were then quantified for validation and comparison.

Comparison between MRI multi-echo imaging and EIT images

Liver MRI images provide *a priori* geometric information to reconstruct 2D EIT images. This information includes the boundary conditions for: 1) the abdominal cross-section, 2) the peripheral tissues consisting of the skin, subcutaneous fat, and the ribs, and 3) the liver in the abdomen. With this information, liver EIT inverse problem was solved as described in the Methods section. For each subject, EIT liver conductivity and MRI PDFF were compared with the corresponding BMI value (**Table 1**). Also, the representative abdomen MRI images for anatomy and PDFF, liver segmentation (annotation), and liver EIT conductivity maps ($S \cdot m^{-1}$) were compared (**Fig. 2**). We observed that the MRI PDFF and EIT liver conductivity were not correlated with the magnitude of BMI. Despite a negative correlation with EIT, the MRI PDFF for Subject 17 with a relatively lower BMI (BMI = 27.1 $Kg \cdot m^{-2}$, PDFF = 6.2%, EIT = 0.3243 $S \cdot M^{-1}$) was higher than that of Subject 3 with a high BMI value (BMI = 39.0 $Kg \cdot m^{-2}$, PDFF = 3.82%, conductivity = 0.3296 $S \cdot M^{-1}$). We also noted that MRI PDFF for Subject 11 with a low BMI value (BMI = 27.9 $Kg \cdot m^{-2}$, MRI PDFF = 3.62%, EIT = 0.3473 $S \cdot M^{-1}$) was lower than that of Subject 10 with a high BMI values (BMI = 34.3 $Kg \cdot m^{-2}$, MRI PDFF = 16.44%, EIT = 0.3007 $S \cdot M^{-1}$). Despite similar BMI (27.1 $Kg \cdot m^{-2}$ vs. 27.9 $Kg \cdot m^{-2}$), the percentages of MRI PDFF of Subject 17 was around two times higher than that of Subject 11 (6.20 vs. 3.62 %). Notably, the MRI PDFF for Subject 10 (BMI = 34.3 $Kg \cdot m^{-2}$) was more than 4 times higher than that of Subject 3 (BMI = 39.0 $Kg \cdot m^{-2}$). These inconsistent comparisons suggest that BMI may not be the ideal index for predicting the levels of fatty liver infiltrate, and Pearson's correlation analyses were performed in the ensuing results.

EIT conductivity vs. MRI PDFF

Using the MRI PDFF and EIT conductivity data from **Table 1**, we performed the Pearson's correlation analyses and identified whether the magnitude of BMI correlates with the percentage of MRI PDFF or EIT conductivity. We demonstrated that the correlation between BMI and MRI PDFF (*R* = -0.037, *p*=0.89, n= 16) and the correlation between BMI and EIT (*R* = -0.19, *p* = 0.47, n= 16) were statistically insignificant (**Fig. 3A-B**). However, the confidence interval plot revealed statistically significant negative correlation between EIT and MRI PDFF (*R* = -0.69, *p* = 0.003, n= 16) (**Fig. 3C**). This finding suggests that EIT conductivity may be used as an index for non-invasive detection method to quantify human liver fatty infiltrate.

Correlation analyses with the demographic parameters, MRI PDFF, and EIT conductivity

To demonstrate liver EIT for identification of fatty liver infiltrate in the enrolled subjects (BMI > 25), we performed correlation analyses with demographic parameters including age, waist circumference, height, and weight, respectively (**Table 2**). We compared the correlation coefficients between MRI PDFF and the demographic parameters (**Fig. 4**). Following the Bonferroni correction for multi-testing, the correlations with age (*R* = -0.13, *p* = 0.64, n= 16), waist circumference (*R* = -0.23, *p* = 0.4, n= 16), height (*R* = -0.59, *p* = 0.016, n= 16) and weight (*R* = -0.41, *p* = 0.12, n= 16) were statistically insignificant. We further compared the correlation coefficients between liver EIT and demographic parameters (**Fig. 5**). The correlation with age (*R* = -0.1, *p* = 0.71, n= 16), waist circumference (*R* = -0.05, *p* = 0.85, n= 16), height (*R* = 0.63, *p* = 0.0092, n= 16) and weight (*R* = 0.19, *p* = 0.47, n= 16) were statistically insignificant. Thus, these analyses corroborate that BMI and other demographic parameters were not correlated with liver fat infiltrate in our overweight/obese subjects.

Discussion

Non-invasive and cost-effective monitoring of fatty liver disease remains an unmet clinical need for the early identification of cardiometabolic disorders. While liver biopsy or magnetic resonance imaging (MRI) have been performed to detect non-alcoholic fatty liver disease (NAFLD), the risk of complications, sampling errors and cost limit its clinical application for the general population. We hereby demonstrated the development of liver EIT as a non-invasive and portable detection method for quantifying liver fat content. We recruited 19 overweight/obese adults with BMI > 25 $Kg{\cdot}M^{-2}$ to undergo liver MRI scans. We performed the individual liver EIT measurements with a multi-electrode array, and we used the anatomic information to address the inverse problem for reconstructing the subject-specific EIT conductivity map. We performed correlation analyses on liver EIT vs. MRI PDFF in relation to the individual demographics[25]. To our best knowledge, this is the first demonstration of statistically significant negative correlation between EIT-acquired liver conductivity and MRI-quantified PDFF.

EIT has been applied to clinical medicine over the past two decades. Diagnostic EIT was developed for pulmonary function and lung capacity[23]. For instance, respiratory monitoring was exhibited by transthoracic impedance pneumography[26,27], and the cardiac output (CO) and stroke volume (SV) measurements were demonstrated via myocardial motion and blood volume,respectively[28,29]. EIT has also been applied for assessing conductivity in breast tissue and brain[30]. Using the multi-electrode configuration, we obtained voltage from the surface of the abdomen by injection of AC current, to reconstruct the EIT conductivity map inside the liver. While EIT has been extensively studied,[31-37] the nonlinear forward and inverse models for reconstructing the EIT conductivity map remain a computational challenge. The ill-posed inverse problem introduces issues of existence, uniqueness, and instability of the solution[36]. The non-linear inverse model for EIT reconstruction requires *a priori* knowledge of the anatomic boundaries to enhance the spatial resolution for establishing the absolute conductivity value[38]. To improve the EIT reconstruction, investigators have integrated EIT with other imaging modalities, including co-registration with MRI[39-41] and introduction of ultrasonic vibration to the target tissue in the presence of the magnetic field. This integration could generate inductive currents within the liver resulting in higher spatial resolution, thus obviating the need for *a priori* knowledge of the object geometry and location needed for EIT reconstruction[42].

Researchers have also applied other approaches to enhance the algorithm for solving the ill-posed inverse problem. For instance, particle swarm optimization (PSO) was applied via paradigm shift from the conventional Gauss-Newton methods for fast convergence and high spatial resolution to solve EIT[43,44]. Recent studies have applied machine learning, including Convolutional Neural Networks, to solve the non-linear ill-posed inverse problem for accurate EIT reconstruction[45,46]. Hamilton *et al.* obtained absolute EIT images by combining the D-bar method with subsequent processing using convolutional neural networks (CNN) technique for sharpening EIT reconstruction[45]. Li *et al.* utilized deep neural networks (DNN) to directly obtain a nonlinear relationship between the one-dimensional boundary voltage and the internal conductivity[46]. Experimentally, the accuracy of EIT reconstruction may be further enhanced by increasing the electrode arrays at multiple levels around the abdomen. This multi-level configuration would be able to inject the currents to and record the voltages from the entire liver. As a result, 3-D reconstruction of a liver conductivity distribution would be realized.

As a corollary, we compared the liver anatomy with MRI PDFF distributions from a representative 3-D rendering (**Fig S1A-B**). The 3-D EIT conductivity map was reconstructed with the aid of the MRI multi-echo sequence as *a priori* knowledge (**Fig S1C**). The high-fat region in the MRI PDFF map (red dashed box) was also detected by the EIT demonstrating lower conductivity. The 3-D MRI and EIT analyses further support the negative correlation between MRI PDFF and EIT liver conductivity. The 3-D EIT conductivity map reveals the inhomogeneous fat distribution as supported by the MRI 3-D rendering images (**Fig S1C**). With additional scanning along the z-direction, a precise mapping could be reconstructed to unveil the details of the heterogeneous fat distribution.

While MRI images provided the *a priori* knowledge to solve the ill-posed inverse problem for EIT reconstruction, alternative methods to provide such information would allow for low-cost liver EIT screening for the general population. A strain-displacement conversion method for reconstructing the deformed shape of the object with the boundary conditions was proposed by Luo *et al* [47]. This method would potentially provide the outer abdomen boundary information by embedding the positional sensors in the EIT sensor belt. Another method is to apply differential EIT, which has the potential to identify the tissue-specific conductivity. If the two frequencies are correctly selected, it is possible to differentiate the fatty tissue from the non-fatty tissues or organs by virtue of fatty tissue-specific electrical properties are distinguished from other tissues or organs (**Table S1**) [48,49] thus providing the peripheral layer boundaries information. Furthermore, using a large number of MRI image database, we may correlate the liver and peripheral layer boundaries with the waist circumferences. This correlation would provide a calibration curve between the boundary conditions and a demographic parameter. Thus, the aforementioned methods would be the future area of research to obviate the need for the MRI-acquired *a priori* knowledge to improve EIT reconstruction.

To assess whether the preexisting medical conditions would influence the absolute EIT conductivity, we included the two subjects with electrolytes abnormities (n=18). We observed that the correlation value decreased from R = -0.69 (p = 0,003, n=16) to R= -0.21 (p = 0.4, n=18 (**Fig S2A**). We further excluded 2 subjects with anemia, and we noted that the correlation improved from R = -0.69 (p = 0,003, n=16) to R = -0.70 (p = 0.0049, n=14) (**Fig S2B**). These results were consistent with the impedimetric property underlying the composition of the liver in the setting of pre-existing conditions-associated electrolyte disturbance. In this case, the presence of leukemia, renal failure, and anemia disrupted the homeostasis of the organ systems; thus, altering the liver conductivity. Thus, our fundamental and experimental analyses pave the way for defining our exclusion criteria for future subject enrolment.

In summary, we enrolled overweight/obese subjects to undergo MRI scans and liver EIT measurements to generate the EIT conductivity map. We demonstrated that the increase in liver EIT conductivity is correlated with a decrease in MRI PDFF. As a corollary, we demonstrated that the 3-D EIT conductivity map also revealed the heterogeneous distribution of fatty gradient as evidenced by the 3-D MRI PDFF. Our correlation analyses supported that subject-specific EIT offers a non-invasive and portable method for the detection of hepatic fat infiltrate; thereby, proving a translational basis for developing liver EIT suitable for operator-independent, low-cost identification and monitoring of fatty liver disease.

Materials and Methods

Study Design

The recruitment of human subjects was conducted at the UCLA Center for Human Nutrition and Obesity in compliance with the UCLA Human Subjects Protection Committee. The study protocol (#15-001756) was approved by the UCLA Internal Review Board. All subjects provided written informed consent before participating in research procedures. We enrolled a total of 19 volunteers including, 15 females and 4 males, from 27 to 74 years old with a waist circumference from 91 cm to 141.5 cm and body mass index (BMI) from 25.5 to 46.8 kg/m^2 (**Fig. 1**). Inclusion criteria for all subjects included an age range between 20-75 years, ability to travel for phlebotomy for whole blood collection, no prescription or over-the-counter medications for weight loss, and absence of alcohol consumption, and no weight change > 5 pounds in the previous 3 months. All subjects must be able to follow instructions and to consent. Exclusion criteria for all subjects included coronary artery disease on medications, claustrophobia, previous liver cancer, liver surgery, alcoholism (DSM-5 criteria: alcohol abuse or dependence), metallic implants or other factors hazardous to the MRI scanner as per the MRI safety guidelines, and body weight > 300 pounds (weight and size restrictions for undergoing MRI). Note that an MRI scan was performed to establish PDFF for quantifying obesity-associated fatty liver. Clinical demographic and physical characteristics of human subjects were collected in terms of gender, BMI ($kg \cdot m^{-2}$), age (years), waist circumference (cm), height (cm), and weight (kg) (**Table 2**). Following enrollment and consent, the subjects underwent a 30-min liver MRI scan, including multi-echo imaging for mapping the proton density fat fraction (PDFF) (**Fig. 6**). Next, EIT measurement was acquired by placing 32 electrodes to the upper abdominal region as indicated by the fiduciary markers immediately following the MRI scan (**Fig. 6A**). A pair of electrodes was used to inject the AC current to the abdomen, and the electrode array was used to record voltage by the pairwise algorithm **(Fig. 6B)**. Liver MRI provided the *a priori* knowledge of the boundary conditions needed for the EIT conductivity map reconstruction and PDFF **(Fig 6C-D)**. EIT conductivity map was reconstructed to distinguish the liver conductivity gradient from other tissues or organs **(Fig. 6E)**. Finally, subject-specific EIT (conductivity map) was compared with the corresponding MRI PDFF **(Fig. 6E)**.

Determination of Liver MRI proton-density fat fraction PDFF

Non-contrast-enhanced abdominal MRI scans were performed on a 3-Tesla system (Skyra or Prisma, Siemens, Erlangen, Germany) using a body array and a spine array coils. The protocol included breath-held anatomical scouts, a breath-held T_2-weighted 2-D multi-slice half-Fourier single-shot turbo spin-echo (HASTE) sequence, and a breath-held 3-D multi-echo gradient-echo sequence (TE = 1.23, 2.46, 3.69, 4.92, 6.15, 7.38 ms; TR = 8.94 ms, flip angle = 4 deg, typical field of view = 400 x 350 x 256 mm^3, typical matrix size = 192 x 168 x 64, parallel imaging factor = 4, typical scan time = 19 sec) to quantify PDFF. Scanner software (LiverLab, Siemens, Erlangen, Germany), which utilized a multi-peak fat spectral model with single R_2* for multi-step signal fitting, was used to calculate PDFF[50]. The MRI images and PDFF maps were saved in DICOM format and downloaded from the scanner for analyses.

To ensure alignment of the subsequent EIT slice position to a corresponding mid-liver MRI slice, we affixed two to three MRI-visible fiducial markers (MR-SPOT 122, Beekley Medical, Bristol, CT) to the skin above the expected mid-liver region prior to performing the MRI scan (**Fig 6A**). The positioning of the fiducial markers was examined on the anatomical scouts. If needed, the MRI technologist would re-position the fiducial markers on the subject's abdomen and re-acquire the scouts. At least one adjustment would be required, and this entire alignment required less than 3 minutes.

The echo 1 (TE=1.23) magnitude images from the 3-D multi-echo gradient-echo sequence were used for contouring the body and the liver to create a 3-D anatomy model. An axial slice in the MRI PDFF maps that contained MRI-visible fiducial markers was selected for analysis. Five circular regions of interest (ROIs) with an area of 5 mm^2 were delineated in the slice with fiducial markers by a trained researcher to avoid blood vessels, bile ducts, and imaging artifacts, and at least 1-2 cm away from the liver capsule. The mean PDFF from the ROIs (0-100%) was reported for each subject.

Theoretical Framework for EIT reconstruction (EIDORS)

The EIT imaging reconstruction was implemented as previously described[11]. Following the injection of a known current to the abdomen, an EIT conductivity map across the abdomen was reconstructed with a set of voltages recorded by with an electrode array placed on the surface of the upper abdomen (see **Fig S3**)[7]. With a *priori* knowledge of the target object (liver), the geometric boundary conditions were established with a high degree of precision to mitigate instability inherent from the ill-posed EIT inverse problem[51](**Fig. 6D**), and the solution was obtained by using a regularized Gauss-Newton (GN) type solver(**Fig. S3**).

The Gauss-Newton (GN) type solver calculates the conductivity by minimizing $\emptyset$, the l2 norm (the square root of the sum of the squares of the values) of the difference between the measured voltage V_o, and a function of the conductivity $f(\sigma)$:

$$\emptyset = \|V_o - f(\sigma)\| \tag{1}$$

where $f(\sigma)$ is considered to be the "forward problem" derived from the Laplace equations:

$$\nabla \cdot (-\sigma \nabla V) = 0 \tag{2}$$

By taking the first order Taylor series expansion of $\emptyset$:

$$\emptyset = \|V_o - f(\sigma)\| \quad \cong \left\|\left(V_o - f(\sigma_0)\right) - J(\sigma - \sigma_0)\right\| \tag{3}$$

where σ_0 is a reference conductivity value, and J is the Jacobian matrix of our inverse problem.

By setting $\frac{\partial \emptyset}{\partial \sigma} = 0$, we minimized $\emptyset$ and obtained σ as follows:

$$\sigma = \sigma_0 + (J^T J)^{-1} J^T (V_o - f(\sigma_0)) \tag{4}$$

Equation (4) is an unconstrained GN form of the inverse problem. Due to the ill-posed nature of the EIT inverse problem, achieving a converged solution from this unconstrained GN form is challenging. The solution σ is highly sensitive to perturbations in voltage (V) measurement which means a small noise in V leads to instability in the final solution. A general method to mitigate the issue is to introduce a constraint term that sways the solution towards the preferred solution:

$$\emptyset^2 = \|\varepsilon\|^2 + \lambda \|\Gamma \sigma\|^2 \tag{5}$$

To balance the tradeoff between fitting the error and constraining the solution from the undesired properties, we incorporated a constraint term, $\lambda\|\Gamma\sigma\|^2$, to the objective function and the resulted form is commonly known as the Tikhonov Regularization. The coefficient, λ, is the regularization parameter that suppresses the conductivity spikes in the solution space.

With a *priori* conductivity within a similar area, the term, Γ, was introduced as a "weighted" Laplacian operator that enables us to adjust more properties of the conductivity and suppress the non-smooth regions. Akin to the present work, this strategy is useful in medical imaging, where a *priori* anatomic information of individual organs was obtained from MRI multi-echo sequence and integrated with the EIT solutions. By applying the regulation term to equation (2), we generated the solution as follows:

$$\sigma_1 = \sigma_0 + (J^T J + \lambda \Gamma^T \Gamma)^{-1} J^T (V - f(\sigma_0)) \tag{6}$$

To obtain the absolute conductivity mapping, we adopted an iterated approach by first assuming an arbitrary conductivity, σ_0, which is used to calculate J, Γ, and $f(\sigma_0)$. From equation (6), we calculated a new conductivity value set, σ_1 to generate a new set of J, Γ and $f(\sigma_1)$. The iteration continued until the difference between σ_n and σ_{n-1} reached a minimally desired value.

In this study, we adopted the online open-source software suite EIDORS (version 3.8) for EIT image reconstruction. An inverse finite element model was aided with a mesh generator (Netgen) for the reconstruction of liver EIT image. Rather than using a presumed geometry for the finite element model, we combined the MRI multi-echo images-acquired geometric information with the multi-electrode-measured voltage data to reconstruct the liver EIT conductivity map. As a result, the computational errors from the variations in the geometry of the abdomen of different subjects were reduced.

EIT measurement and reconstruction for fat infiltrate

Following MRI scans, the subjects underwent EIT measurement. The MRI-visible fiducial markers on the abdomen facilitated the circumferential positioning of EIT electrodes. Next, the subjects were instructed to perform the same breath-holds (e.g., end inspiration) as they did for the MRI scan to ensure that the EIT slice matched with the level of the mid-liver MRI slice. Electrical measurement and data acquisition were conducted using the Swisstom EIT Pioneer Set (Swisstom AG, Switzerland). An array of disposable surface electrocardiogram electrodes (Covidien, Ireland) was attached to the skin of the subject, and each of them was connected to one of the 32 data acquisition channels of the Swisstom system, which was interfaced with the controlling computer via a separate module (**Fig. 6A-B**). The AC currents with programmable magnitude from 2-4 mA were injected to the upper abdomen at 50 kHz and 250 kHz respectively through the selected channels, and the resulting voltage responses were recorded by a separate pair of electrodes. A “skipping 4” pattern was used for current injection and voltage recording[52] (**Fig. 6A**). Based on the anatomy of the liver, we established both 2-D and 3-D forward models for EIT reconstruction using the EIDORS library. The acquired voltage data were used to calculate 2-D and 3-D conductivity distribution. Following EIT reconstruction of the liver conductivity maps, we compared the liver conductivity ($S \cdot m^{-1}$) and MRI PDFF with the subject-specific demographics, and we generated the confidence interval plots to demonstrate the correlation between liver EIT conductivity and MRI PDFF.

Statistical Analysis

We performed correlation analyses in the context of the subjects' demographics (n=19) (such as chronic lymphocytic leukemia and renal failure). We excluded one liver EIT measurement due to the malfunction of electrodes. We compared the differences in correlation values between the presence (n= 18) and the absence of pre-existing medical conditions that could disturb the circulation and tissue electrolytes (n=16). The correlation between liver conductivity and MRI PDFF was assessed by Pearson's correlation analysis and the Bonferroni correction for multi-testing. The comparison between EIT and demographics, and between MRI PDFF and demographics, were analyzed for statistically significant coefficients and 95% confidence interval using Pearson's correlation analysis in *R*.

Acknowledgment

The present work was funded by the National Institutes of Health R01HL083015 (TKH), R01HL111437 (TKH), R01HL129727 (TKH), R01HL118650 (TKH), VA MERIT AWARD I01 BX004356 (TKH), and American Heart Association 19CDA34769186 (AK).

Supplementary Materials

Fig. S1. 3-D MRI PDFF mapping vs. 3-D EIT image.

Fig. S2. Sub-analysis of EIT liver conductivity vs. MRI PDFF for all subjects and additional exclusion of anemic subjects.

Fig. S3. Schematic flow of EIT reconstruction.

Table S1. Conductivities of human tissue.

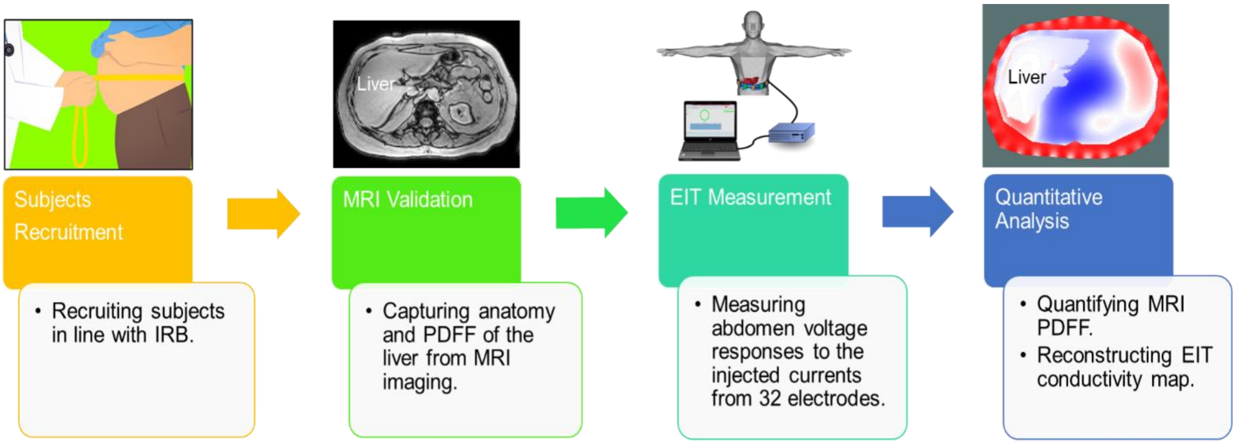

Figure 1. Schematic workflow of the comparison and validation of the MRI and EIT. Volunteers were recruited in line with the UCLA Institutional Human Subjects Protection Committee. Multi-echo MRI scans were performed to provide the liver anatomy and proton density fat fraction (PDFF), followed by the EIT measurements. Finally, the EIT conductivity maps were reconstructed and the MRI PDFF was used to quantify fatty liver infiltrate and to compare with EIT liver conductivity.

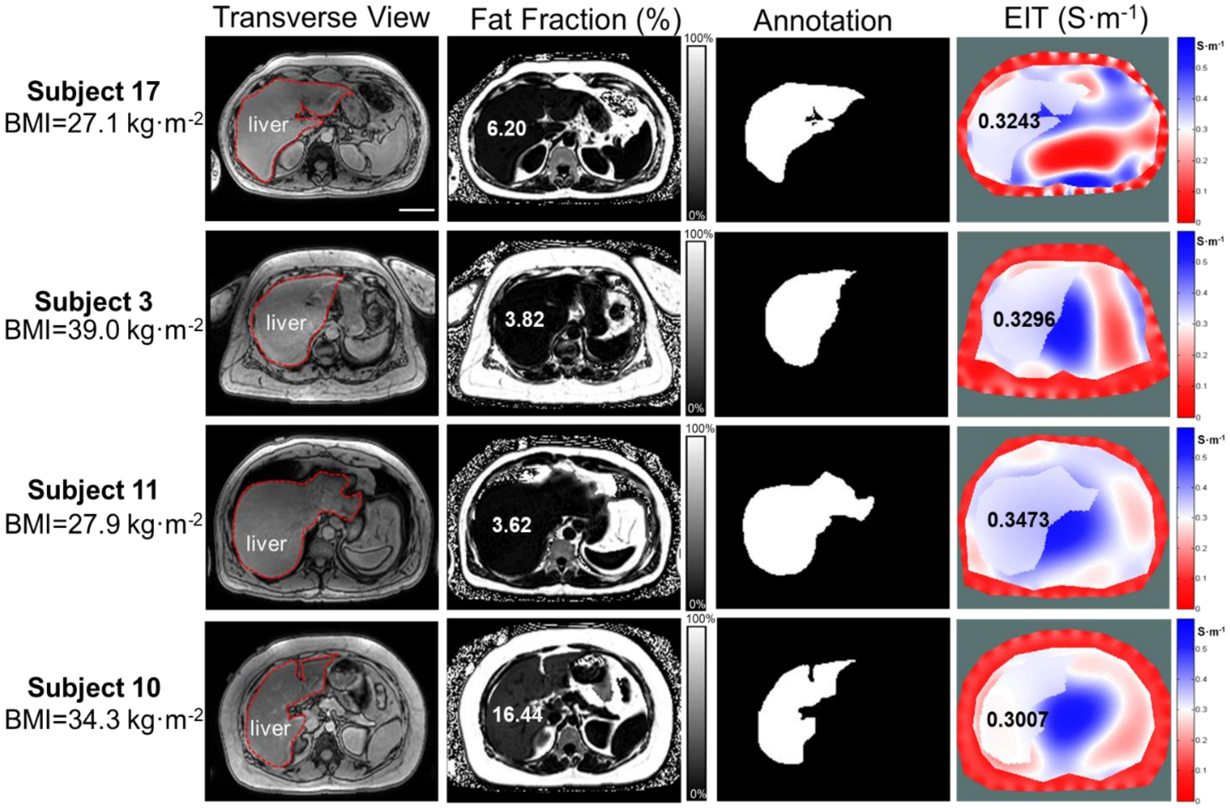

Figure 2. Representative MRI multi-echo and EIT images. Four representative subjects with different BMI values (Kg·m^{-2}) were compared with MRI PDFF (%) and EIT conductivity (S·M^{-1}), respectively. The transverse MRI views demarcate the liver anatomy, the fat fractions provide the corresponding MRI PDFF, annotation reveals the liver boundary condition following image segmentation, and 2-D EIT images unveil the abdomen conductivity distribution and average liver conductivity. The subject 17 with a BMI of 27.1 Kg·m^{-2} developed a relatively high MRI PDFF (6.2%) and a low EIT liver conductivity (0.3243 S·M^{-1}); whereas the subject 3 with BMI of 39 Kg·m^{-2} developed a relatively low MRI PDFF (3.82%) and high EIT liver conductivity (0.3296 S·M^{-1}). However, the subject 11 with BMI of 27.9 Kg·m^{-2} developed a relatively low MRI PDFF (3.62%) in association with a relatively high EIT liver conductivity (0.3473 S·M^{-1}), and the subject 10 with BMI of 34.3 Kg·m^{-2} also developed a relatively high MRI PDFF (16.44%) in association with a low EIT liver conductivity (0.3007 S·M^{-1}). These initial comparisons suggest inconsistent correlations between BMI and MRI PDFF and EIT liver conductivity. Scale bar: 8 cm.

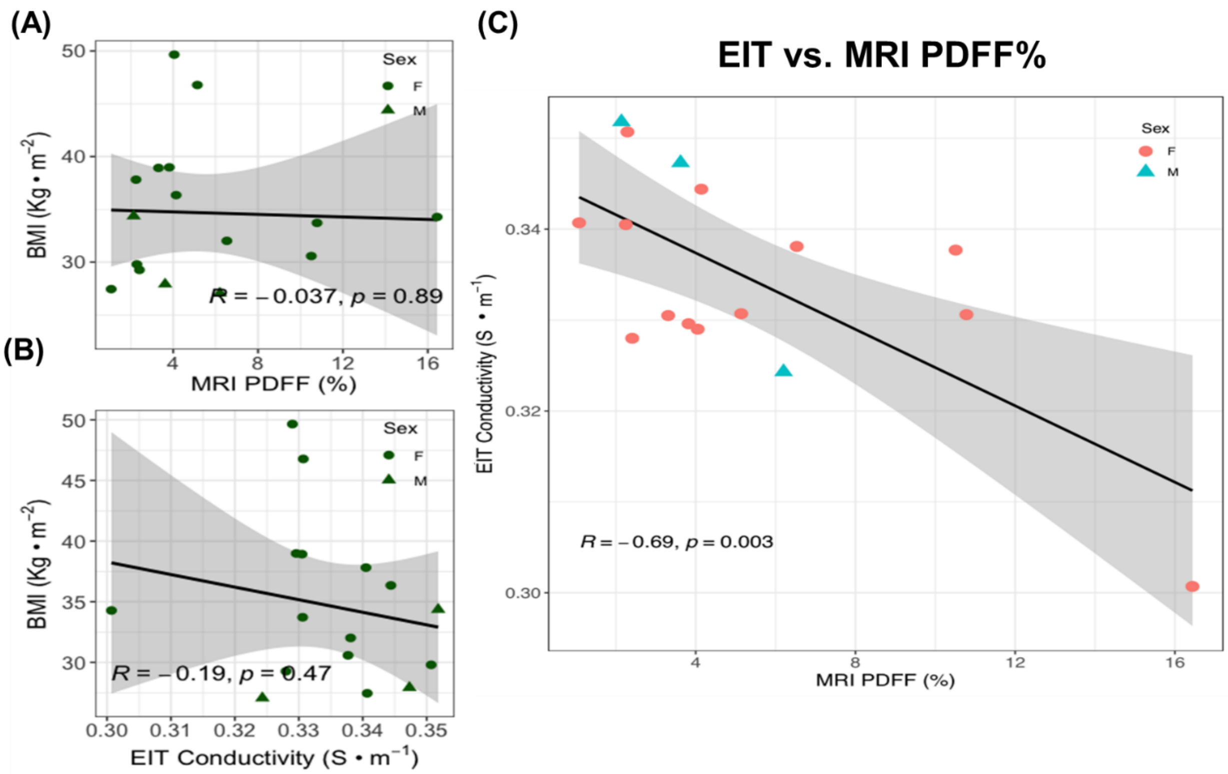

Figure 3. Statistical analyses of BMI vs. MRI PDFF and vs. EIT liver conductivity. (A) BMI values are not correlated with MRI PDFF. (Pearson correlation coefficient R = - 0.037, p = 0.89, n=16). **(B)**. BMI values were also not correlated with EIT liver conductivity values (R = - 0.19, p = 0.47, n=16). **(C)** EIT liver conductivity values were negatively correlated with MRI PDFF (R = -0.69, p = 0,003, n=16). The shaded areas reflect the 95% confidence intervals of the linear slopes.

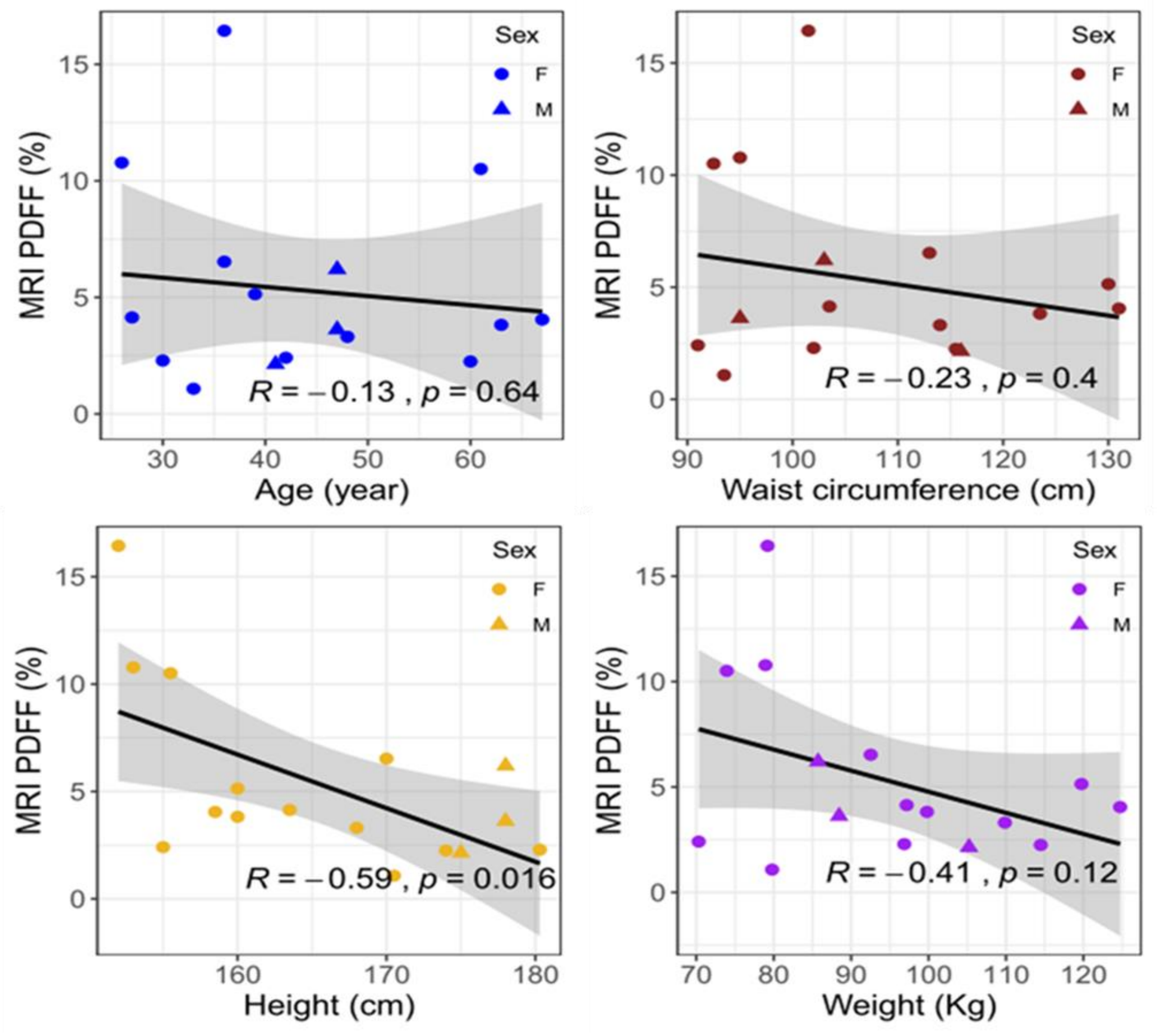

Figure 4. MRI PDFF vs. age, waist, height, and weight. The Pearson correlation coefficients (*R*) and *p* values were analyzed for age, waist circumference, height, and weight, respectively. The circles denote female subjects and triangles denote male subjects. The 95% confidence intervals of the linear slopes are illustrated as shaded area. *R* values are -0.13 for age (*p* = 0.64, n= 16), - 0.23 for waist circumference (*p*= 0.4, n=16), -0.59 for height (*p*= 0.016, n= 16)., and -0.41 for weight (*p*= 0.12, n= 16), demonstrating low to intermediate correlation with MRI PDFF.

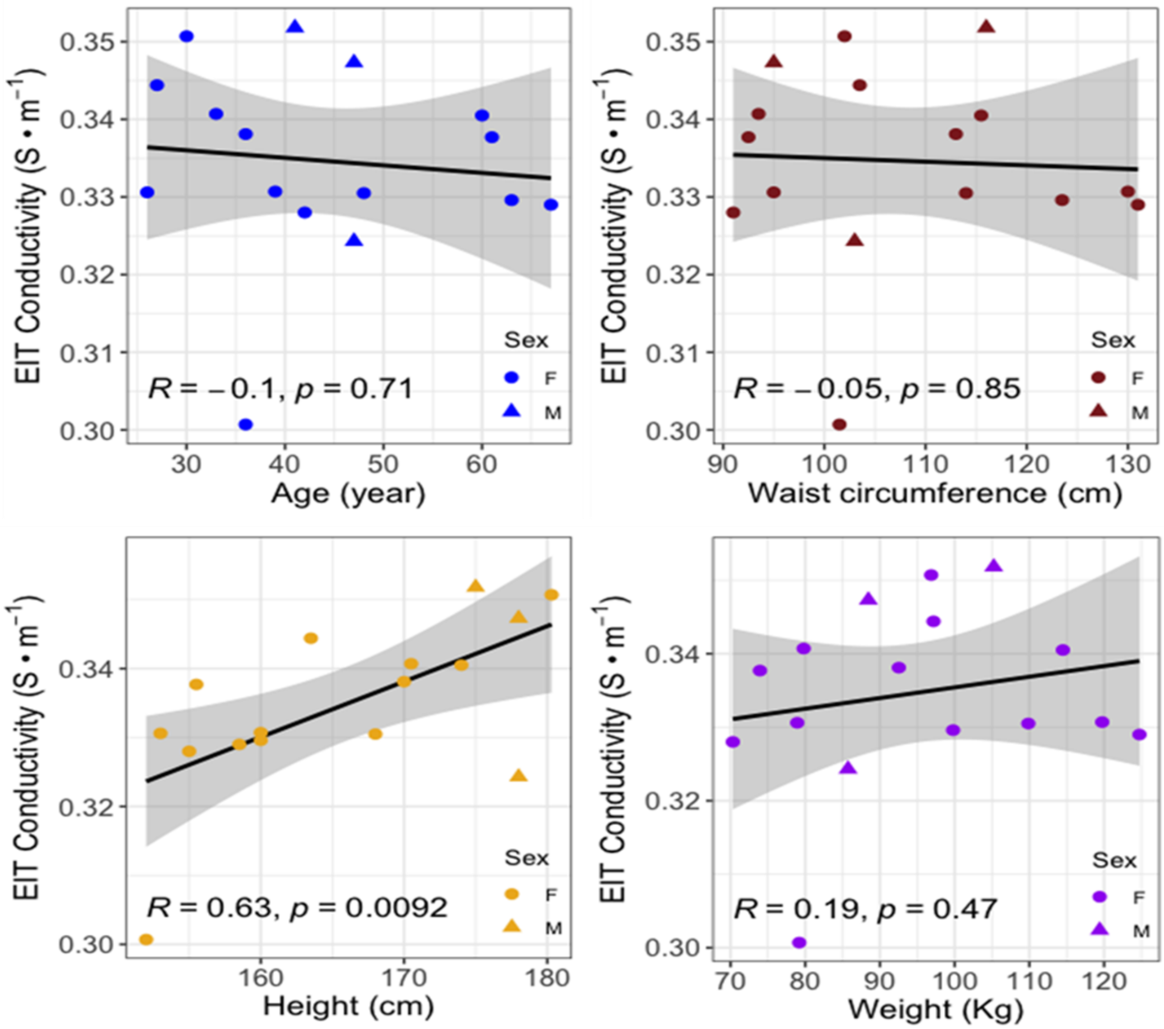

Figure 5. EIT liver conductivity vs. age, waist, height, and weight. The *R* values for age (R = - 0.1, *p* = 0.71, n= 16), waist circumference (R = - 0.05, *p*= 0.85, n=16), height (R = 0.63, *p* = 0.0092, n=16) and weight (R = 0.19, *p* = 0.47, n=16) demonstrate low to intermediate correlation with EIT conductivity.

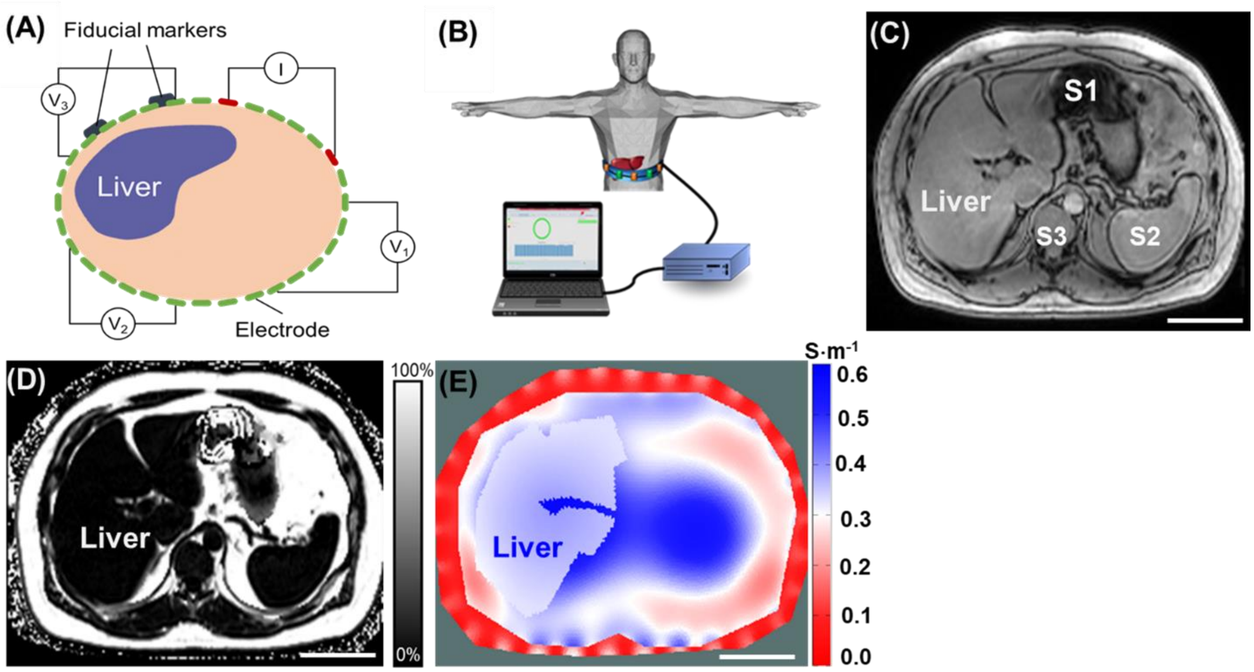

Figure 6. Schematic of EIT measurement, reconstruction, and 2-D representation. **(A)** Schematic illustrates circumferential electrode placement around the abdomen for pairwise voltage measurements. The fiducial markers indicate the anatomic level at which the multi-electrode array was circumferentially positioned for liver EIT measurements. **(B)** Thirty-two electrodes were adhered to the abdomen, as indicated by the fiducial markers. The recorded voltage signals were input to a signal adaptor and the data acquisition channels for EIT measurements. A representative MRI multi-echo image demarcates the boundary conditions **(C)** and PDFF map **(D)** for the abdomen, liver, stomach and spleen. S1: Stomach, S2: Spleen, S3: Spine. **(E)** A representative 2-D EIT image reveals the conductivity distribution. Scale bar: 8 cm.

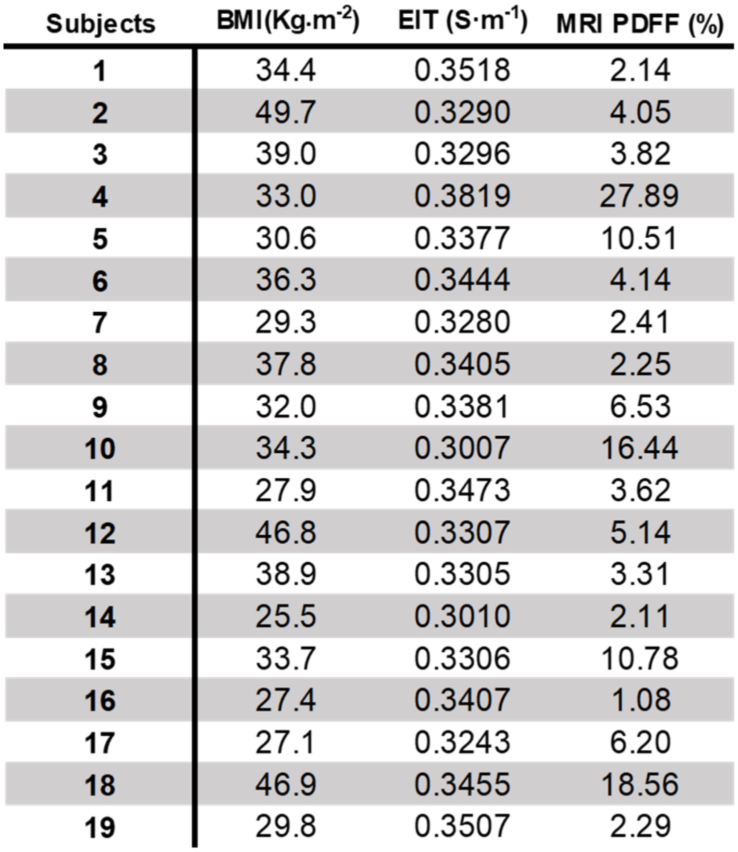

Subjects	BMI(Kg·m^{-2})	EIT (S·m^{-1})	MRI PDFF (%)
1	34.4	0.3518	2.14
2	49.7	0.3290	4.05
3	39.0	0.3296	3.82
4	33.0	0.3819	27.89
5	30.6	0.3377	10.51
6	36.3	0.3444	4.14
7	29.3	0.3280	2.41
8	37.8	0.3405	2.25
9	32.0	0.3381	6.53
10	34.3	0.3007	16.44
11	27.9	0.3473	3.62
12	46.8	0.3307	5.14
13	38.9	0.3305	3.31
14	25.5	0.3010	2.11
15	33.7	0.3306	10.78
16	27.4	0.3407	1.08
17	27.1	0.3243	6.20
18	46.9	0.3455	18.56
19	29.8	0.3507	2.29

Table 1. List of BMI (Kg·m^{-2}), MRI PDFF (%) and EIT liver conductivity of all subjects. (S·M^{-1}).

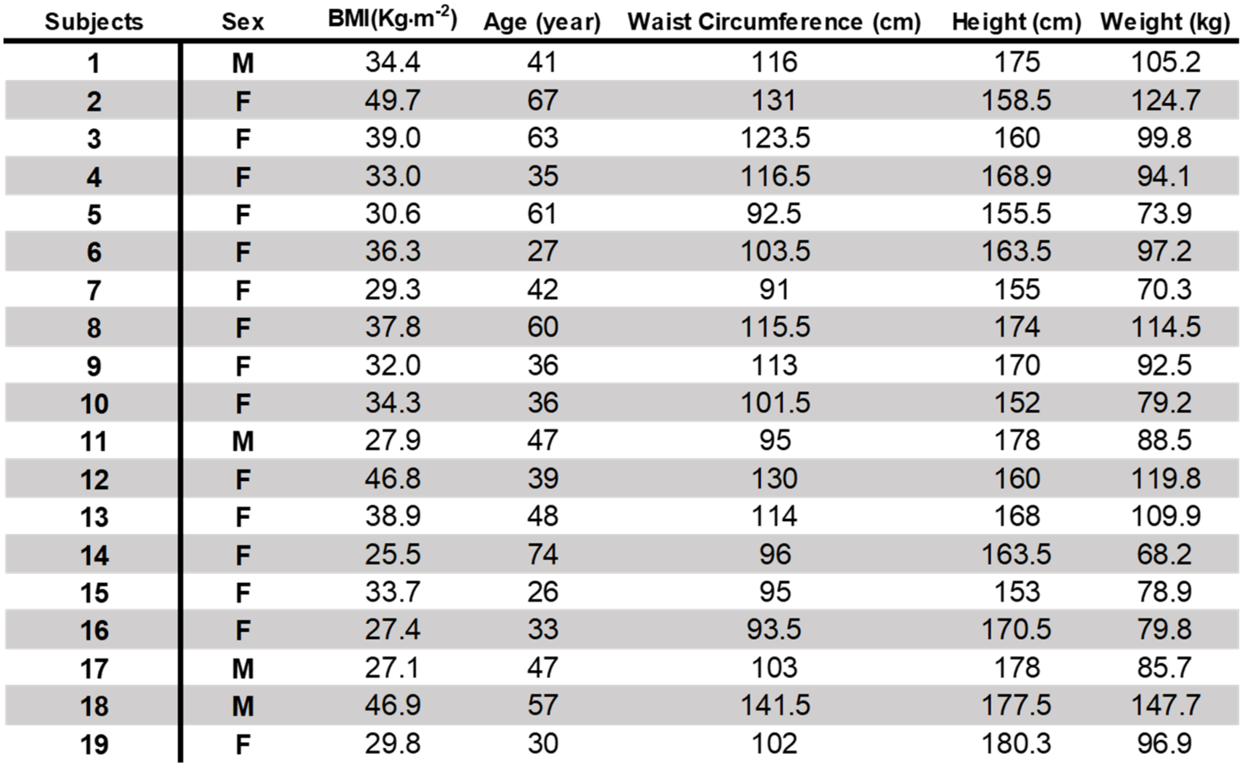

Subjects	Sex	BMI(Kg·m^{-2})	Age (year)	Waist Circumference (cm)	Height (cm)	Weight (kg)
1	**M**	34.4	41	116	175	105.2
2	**F**	49.7	67	131	158.5	124.7
3	**F**	39.0	63	123.5	160	99.8
4	**F**	33.0	35	116.5	168.9	94.1
5	**F**	30.6	61	92.5	155.5	73.9
6	**F**	36.3	27	103.5	163.5	97.2
7	**F**	29.3	42	91	155	70.3
8	**F**	37.8	60	115.5	174	114.5
9	**F**	32.0	36	113	170	92.5
10	**F**	34.3	36	101.5	152	79.2
11	**M**	27.9	47	95	178	88.5
12	**F**	46.8	39	130	160	119.8
13	**F**	38.9	48	114	168	109.9
14	**F**	25.5	74	96	163.5	68.2
15	**F**	33.7	26	95	153	78.9
16	**F**	27.4	33	93.5	170.5	79.8
17	**M**	27.1	47	103	178	85.7
18	**M**	46.9	57	141.5	177.5	147.7
19	**F**	29.8	30	102	180.3	96.9

Table 2. Demographics of overweight/obese subjects. The demographics of 19 subjects including sex, BMI, age, waist circumference, height, and weight, are demonstrated.

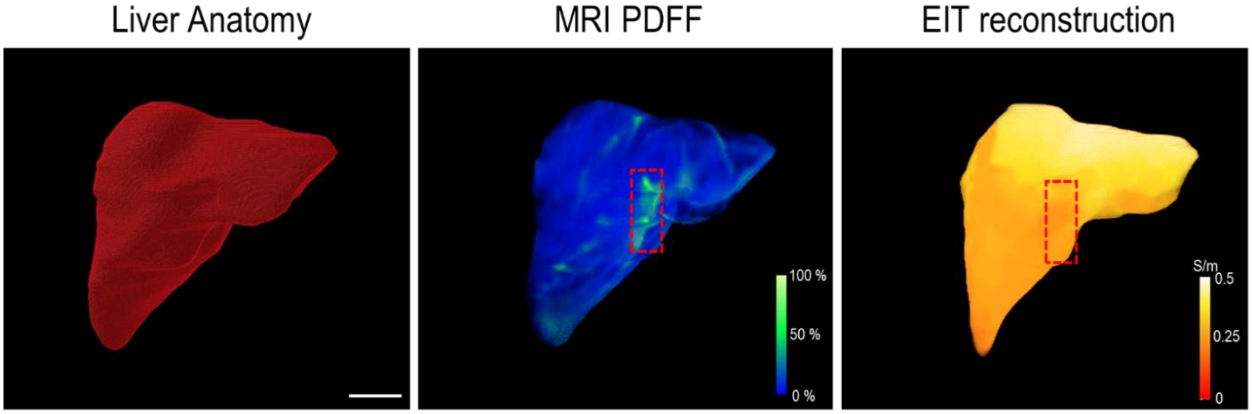

Figure S1. 3-D MRI PDFF mapping vs. 3-D EIT image. (A) The representative 3-D liver boundary condition was established following segmentation of the MRI multi-echo imaging. **(B)** 3-D MRI PDFF mapping reveals a heterogeneous distribution of MRI PDFF. The red dashed box highlights the region with a relatively high fat fraction. **(C)** 3-D EIT image unveils the heterogeneous gradient of conductivity. The dash red box is consistent with that of MRI PDFF mapping. Thus, the 3-D comparison between MRI multi-echo imaging and EIT image further supports the correlation between MRI fat fraction and EIT conductivity. Scale bar: 5 cm.

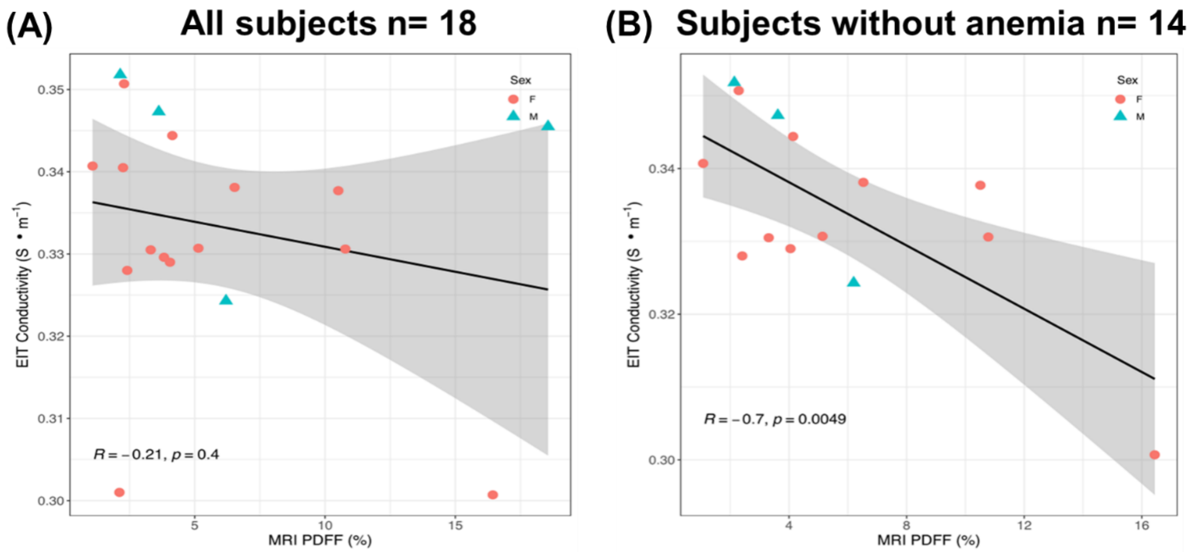

Figure S2. Sub-analysis of EIT liver conductivity vs. MRI PDFF for all subjects and additional exclusion of anemic subjects. (A) The negative correlation between EIT conductivity and MRI PDFF was reduced to R=-0.21 in the presence of preexisting medical conditions implicated in disturbing tissue electrolytes (*p* = 0.4, n= 18). **(B)** The correlation between EIT liver vs. MRI PDFF was increased to R = -0.70 in the absence of anemia subjects (*p* = 0.0049, n=14). The shaded areas reflect the 95% confidence intervals of the linear slopes.

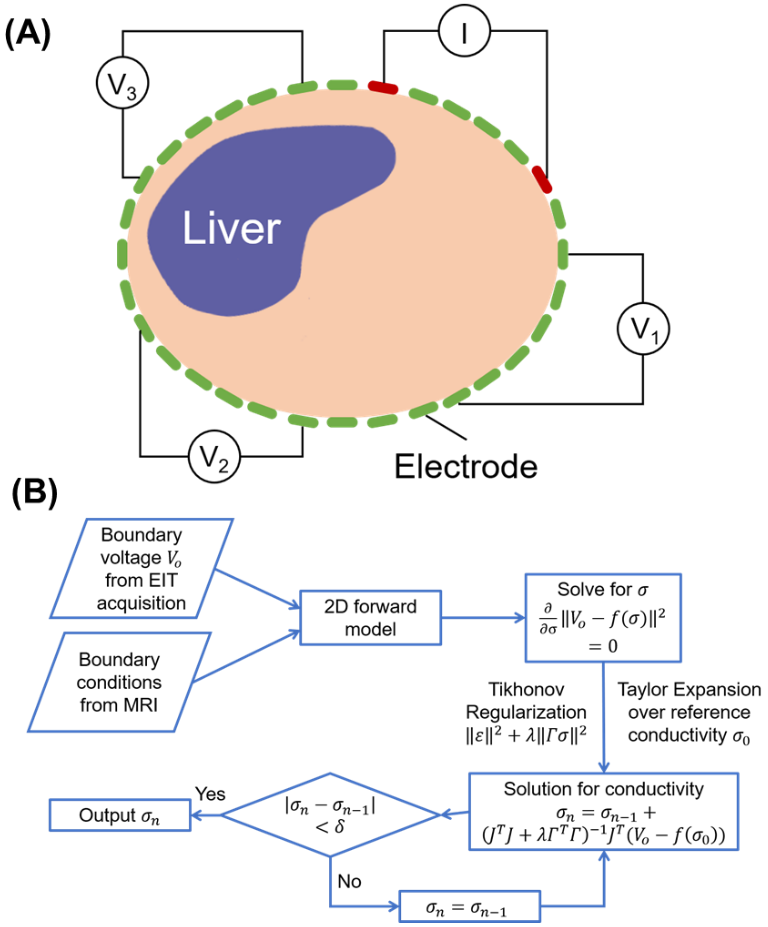

Figure S3. Schematic flow of EIT reconstruction. (A) "Skipping 4" pattern was used for both current injection and voltage acquisition. There were 4 electrodes separating each pair of stimulating and detecting electrodes. **(B)** EIT reconstruction was established by solving the inverse problem via a regularized Gauss-Newton (GN) type solver.

Tissue	$S \cdot m^{-1}$	Tissue	$S \cdot m^{-1}$
liver	0.07	fat	0.04
lung	0.14	musle	0.35
heart	0.10	bone marrow	0.06
kidney	0.10	skin	0.10
intestine	0.35	blood	0.70
stomach	0.50	cartilage	0.18

Table S1 Conductivities of human tissues at 50 kHz [$S \cdot m^{-1}$].

Reference

1 Ahlqvist, E. *et al.* Novel subgroups of adult-onset diabetes and their association with outcomes: a data-driven cluster analysis of six variables. *The lancet Diabetes & endocrinology* **6**, 361-369 (2018).

2 Lazo, M. & Clark, J. M. The epidemiology of nonalcoholic fatty liver disease: a global perspective. *Semin Liver Dis* **28**, 339-350, doi:10.1055/s-0028-1091978 (2008).

3 Kemmer, N. *et al.* Nonalcoholic fatty liver disease epidemic and its implications for liver transplantation. *Transplantation* **96**, 860-862, doi:10.1097/01.TP.0000436723.59879.01 (2013).

4 Marchesini, G. *et al.* Nonalcoholic fatty liver, steatohepatitis, and the metabolic syndrome. *Hepatology* **37**, 917-923 (2003).

5 Vernon, G., Baranova, A. & Younossi, Z. M. Systematic review: the epidemiology and natural history of non-alcoholic fatty liver disease and non-alcoholic steatohepatitis in adults. *Aliment Pharmacol Ther* **34**, 274-285, doi:10.1111/j.1365-2036.2011.04724.x (2011).

6 Bravo, A. A., Sheth, S. G. & Chopra, S. Liver biopsy. *The New England journal of medicine* **344**, 495-500, doi:10.1056/nejm200102153440706 (2001).

7 Reeder, S. B., Hu, H. H. & Sirlin, C. B. Proton density fat-fraction: a standardized MR-based biomarker of tissue fat concentration. *Journal of magnetic resonance imaging* **36**, 1011-1014 (2012).

8 Yokoo, T. *et al.* Linearity, bias, and precision of hepatic proton density fat fraction measurements by using MR imaging: a meta-analysis. *Radiology* **286**, 486-498 (2017).

9 Shuster, A., Patlas, M., Pinthus, J. & Mourtzakis, M. The clinical importance of visceral adiposity: a critical review of methods for visceral adipose tissue analysis. *The British journal of radiology* **85**, 1-10 (2012).

10 Tang, A., Cloutier, G., Szeverenyi, N. M. & Sirlin, C. B. Ultrasound elastography and MR elastography for assessing liver fibrosis: part 1, principles and techniques. *American journal of roentgenology* **205**, 22-32 (2015).

11 Luo, Y. *et al.* Non-invasive electrical impedance tomography for multi-scale detection of liver fat content. *Theranostics* **8**, 1636 (2018).

12 Brown, B. H. Electrical impedance tomography (EIT): a review. *Journal of medical engineering & technology* **27**, 97-108 (2003).

13 Cheney, M., Isaacson, D. & Newell, J. C. Electrical impedance tomography. *SIAM review* **41**, 85-101 (1999).

14 Christ, M., Kenig, C. E. & Sadosky, C. *Harmonic analysis and partial differential equations: essays in honor of Alberto P. Calderón*. (University of Chicago Press, 2001).

15 Holder, D. S. *Electrical impedance tomography: methods, history and applications*. (CRC Press, 2004).

16 Bayford, R. H. Bioimpedance tomography (electrical impedance tomography). *Annu. Rev. Biomed. Eng.* **8**, 63-91 (2006).

17 Wilkinson, J. & Thanawala, V. Thoracic impedance monitoring of respiratory rate during sedation–is it safe? *Anaesthesia* **64**, 455-456 (2009).

18 Frerichs, I., Becher, T. & Weiler, N. Electrical impedance tomography imaging of the cardiopulmonary system. *Current opinion in critical care* **20**, 323-332 (2014).

19 Nguyen, D. M., Andersen, T., Qian, P., Barry, T. & McEwan, A. Electrical Impedance Tomography for monitoring cardiac radiofrequency ablation: a scoping review of an emerging technology. *Medical Engineering & Physics* (2020).

20 Brown, B. H. Electrical impedance tomography (EIT): a review. *Journal of Medical Engineering & Technology* **27**, 97-108 (2003).

21 Isaacson, D., Cheney, M. & Newell, J. C. Comments on reconstruction algorithms. *Clinical Physics and Physiological Measurement* **13**, 83 (1992).

22 Packard, R. R. S. *et al.* 3-D Electrochemical Impedance Spectroscopy Mapping of Arteries to Detect Metabolically Active but Angiographically Invisible Atherosclerotic Lesions. *Theranostics* **7**, 2431 (2017).

23 Brown, B. H. & Seagar, A. D. The Sheffield data collection system. *Clinical Physics and Physiological Measurement* **8**, 91 (1987).

24 Bachtiar, V. *et al.* Repeatability and reproducibility of multiparametric magnetic resonance imaging of the liver. *PloS one* **14**, e0214921 (2019).

25 Hu, H. H., Li, Y., Nagy, T. R., Goran, M. I. & Nayak, K. S. Quantification of absolute fat mass by magnetic resonance imaging: a validation study against chemical analysis. *International Journal of Body Composition Research* **9**, 111 (2011).

26 Wilkinson, J. N. & Thanawala, V. U. Thoracic impedance monitoring of respiratory rate during sedation–is it safe? *Anaesthesia* **64**, 455-456 (2009).

27 Brown, B. H. Impedance pneumography. (1997).

28 Pikkemaat, R., Lundin, S., Stenqvist, O., Hilgers, R.-D. & Leonhardt, S. Recent advances in and limitations of cardiac output monitoring by means of electrical impedance tomography. *Anesthesia & Analgesia* **119**, 76-83 (2014).

29 Zlochiver, S., Freimark, D., Arad, M., Adunsky, A. & Abboud, S. Parametric EIT for monitoring cardiac stroke volume. *Physiological Measurement* **27**, S139 (2006).

30 Bayford, R. H. Bioimpedance tomography (electrical impedance tomography). *Annu. Rev. Biomed. Eng.* **8**, 63-91 (2006).

31 Krautblatter, M. & Hauck, C. Electrical resistivity tomography monitoring of permafrost in solid rock walls. *Journal of Geophysical Research: Earth Surface* **112** (2007).

32 Bolton, G. T. *et al.* Development of an electrical tomographic system for operation in a remote, acidic and radioactive environment. *Chemical Engineering Journal* **130**, 165-169 (2007).

33 Rücker, C., Günther, T. & Spitzer, K. Three-dimensional modelling and inversion of DC resistivity data incorporating topography—I. Modelling. *Geophysical Journal International* **166**, 495-505 (2006).

34 Heinrich, S., Schiffmann, H., Frerichs, A., Klockgether-Radke, A. & Frerichs, I. Body and head position effects on regional lung ventilation in infants: an electrical impedance tomography study. *Intensive care medicine* **32**, 1392 (2006).

35 Adler, A. *et al.* Whither lung EIT: where are we, where do we want to go and what do we need to get there? *Physiological Measurement* **33**, 679 (2012).

36 Calderón, A. P. On an inverse boundary value problem. *Computational & Applied Mathematics* **25**, 133-138 (2006).

37 Cheney, M., Isaacson, D. & Newell, J. C. Electrical impedance tomography. *SIAM Review* **41**, 85-101 (1999).

38 Seo, J. K. & Woo, E. J. *Nonlinear inverse problems in imaging*. (John Wiley & Sons, 2012).

39 Crabb, M. *et al.* Mutual information as a measure of image quality for 3D dynamic lung imaging with EIT. *Physiological measurement* **35**, 863 (2014).

40 Baek, K. I. *et al.* Advanced microscopy to elucidate cardiovascular injury and regeneration: 4D light-sheet imaging. *Progress in biophysics and molecular biology* **138**, 105-115 (2018).

41 Chang, C.-C. *et al.* Three-dimensional Imaging Coupled with Topological Quantification Uncovers Retinal Vascular Plexuses Undergoing Obliteration. *Theranostics* **11**, 1162-1175, doi:10.7150/thno.53073 (2021).

42 Grasland-Mongrain, P., Mari, J.-M., Chapelon, J.-Y. & Lafon, C. Lorentz force electrical impedance tomography. *Irbm* **34**, 357-360 (2013).

43 Chen, M.-Y., Hu, G., He, W., Yang, Y.-L. & Zhai, J.-Q. in *Life system modeling and intelligent computing* 342-350 (Springer, 2010).

44 Feitosa, A. R., Ribeiro, R. R., Barbosa, V. A., de Souza, R. E. & dos Santos, W. P. in *5th ISSNIP-IEEE Biosignals and Biorobotics Conference (2014): Biosignals and Robotics for Better and Safer Living (BRC).* 1-6 (IEEE).

45 Hamilton, S. J. & Hauptmann, A. Deep D-bar: Real-time electrical impedance tomography imaging with deep neural networks. *IEEE transactions on medical imaging* **37**, 2367-2377 (2018).

46 Li, X. *et al.* A novel deep neural network method for electrical impedance tomography. *Transactions of the Institute of Measurement and Control* **41**, 4035-4049 (2019).

47 Luo, Z., Li, J., Hong, G. & Li, H. Strain-based displacement field reconstruction method for thin rectangular plate through orthogonal deflection curves bridging. *Structural Control and Health Monitoring* **27**, e2457 (2020).

48 Hirata, A., Takano, Y., Kamimura, Y. & Fujiwara, O. Effect of the averaging volume and algorithm on the in situ electric field for uniform electric-and magnetic-field exposures. *Physics in Medicine & Biology* **55**, N243 (2010).

49 Menden, T. *et al.* Reconstruction algorithm for frequency-differential EIT using absolute values. *Physiological measurement* **40**, 034008 (2019).

50 Zhong, X. *et al.* Liver fat quantification using a multi-step adaptive fitting approach with multi-echo GRE imaging. *Magnetic resonance in medicine* **72**, 1353-1365 (2014).

51 Ider, Y. Z. & Birgül, Ö. Use of the magnetic field generated by the internal distribution of injected currents for electrical impedance tomography (MR-EIT). *Turkish Journal of Electrical Engineering & Computer Sciences* **6**, 215-226 (2000).

52 Adler, A., Gaggero, P. O. & Maimaitijiang, Y. Adjacent stimulation and measurement patterns considered harmful. *Physiological measurement* **32**, 731 (2011).